

Dissertation

submitted to the
Combined Faculties for the Natural Sciences and for Mathematics
of the Ruperto-Carola University of Heidelberg, Germany
for the degree of
Doctor of Natural Sciences

presented by

Diplom-Physiker Patrick Glaschke
Born in Erbach, Germany

Oral examination: 24. May 2006

**Studying the Formation of Protoplanets:
A new Hybrid Code
for
Planetesimal Dynamics**

Referees: Prof. Dr. Rainer Spurzem
Prof. Dr. Werner M. Tscharnuter

Zusammenfassung — Abstract

Diese Arbeit präsentiert neuartige Simulationen zur Entstehung von Planeten, wobei der Schwerpunkt auf der Entstehung von Protoplaneten aus Planetesimalen liegt. In diesem Stadium wird die Entwicklung des System von Kollisionen und Zwei-Körper-Streuungen bestimmt, die eine sorgfältige Modellierung der Entwicklung der Geschwindigkeitsdispersion und der Größenverteilung über den ganzen Größenbereich erfordern.

Zu diesem Zweck wurde ein neues Hybridprogramm entwickelt, genannt NBODY6DISC, um den vollen Größenbereich von kilometergroßen Planetesimalen bis zu Protoplaneten abzudecken. Es vereint die Vorteile eines N -Körper-Ansatzes zur Integration der größeren Körper mit einem zusätzlichen statistischen Modell zur Beschreibung der kleineren Planetesimale.

Dieses Programm wird auf die Entstehung von Protoplaneten angewendet. Die Simulationen zeigen kein Beenden der protoplanetaren Akkretion durch die Entstehung von Lücken in der Planetesimalverteilung, sondern nur schwache Fluktuationen in der Oberflächendichte. Darüber hinaus sind diese Strukturen nur schwach mit den Positionen der Protoplaneten korreliert. Die Untersuchung verschiedener Schlagfestigkeiten zeigt, daß die Fragmentation von Planetesimalen hauptsächlich den gesamten Massenverlust kontrolliert, der aber während des frühen Wachstums der Protoplaneten relativ gering ist. Es zeigt sich, daß Fragmentation in Verbindung mit dem schnellen Verlust der Fragmente durch Gasreibung eine obere Grenze für die Masse der Protoplaneten in Abhängigkeit vom Abstand zum Zentralstern setzt.

This work presents novel simulations of the formation of planets, with a focus on the formation of protoplanets out of planetesimals. The evolution of the system at this stage is driven by encounters as well as direct collisions, and requires a careful modelling of the evolution of the velocity dispersion and the size distribution over the whole size range.

To serve this purpose, a new hybrid code called NBODY6DISC has been developed to cover the full size range from kilometre-sized planetesimals to protoplanets. It combines the advantages of a pure N -body approach for the integration of the larger bodies with an additional statistical model to cover the smaller planetesimals.

This new code is applied to the formation of protoplanets. The simulations show no termination of the protoplanetary accretion due to gap formation, since the distribution of the planetesimals is only subjected to small fluctuation. Moreover, these features are weakly correlated with the positions of the protoplanets. The exploration of different impact strengths indicates that fragmentation mainly controls the overall mass loss, which is less pronounced during the early runaway growth. It is shown that fragmentation in combination with the effective removal of collisional fragments by gas drag sets an universal upper limit of the protoplanetary mass as a function of the distance to the host star.

*Love is an act of endless forgiveness,
a tender look which becomes a habit.*

Peter Ustinov (1921–2004)

Contents

1	Introduction	1
2	Planet Formation	5
2.1	Early Stages	5
2.2	Formation of Planetesimals	5
2.3	Formation of Protoplanets	7
2.4	Oligarchic Growth	7
2.5	Migration	8
2.6	Summary	9
3	Theory	11
3.1	Solar Nebula	11
3.2	Kepler Orbits	12
3.3	Hill's Problem	13
3.4	Protoplanet Growth	15
4	Integrator	19
4.1	NBODY6++	19
4.2	Individual Time Steps	20
4.3	Ahmad-Cohen Neighbour Scheme	21
4.4	Hermite Scheme	21
4.5	Hermite Iteration	22
4.6	Extended Hermite Scheme	23
4.7	KS-Regularisation	24
4.8	Additional Forces	24
4.8.1	Central Potential	25
4.8.2	Drag Force	25
4.8.3	KS-Pairs	26
5	Optimising the Code	27
5.1	Introduction	27
5.2	Disc Geometry and Neighbour Scheme	27
5.3	Optimal Neighbour Criterion	28
5.4	Neighbour Changes	30
5.5	Neighbour Prediction	30
5.6	Communication Scheme	31
5.7	Block Size Distribution	32
5.8	Optimal Neighbour Number	34

6	Collisional Model	37
6.1	Introduction	37
6.2	Concepts	37
6.3	Theory	38
7	Collisional Cascades	41
7.1	Introduction	41
7.2	Self-similar Collisions	41
7.3	Size-dependent Strength	43
7.4	Perturbation of Equilibrium	44
7.5	Migration and Collisions	47
7.6	Coagulation	49
7.7	Models for M_{red}	50
8	Statistical Model	51
8.1	Fokker-Planck Equation	51
8.2	Distribution Function	52
8.3	Dynamical Friction	53
8.4	High Speed Encounters	54
8.5	Low Speed Encounters	57
8.6	Distant Encounters	58
8.7	Gas Damping	58
8.8	Unified Expressions	59
8.9	Inhomogeneous Disc	59
8.10	Diffusion Coefficient	61
8.11	Coagulation Equation	62
8.12	Collisional Damping	63
8.13	Correlation	64
8.14	Discretisation	66
8.15	Integrator	67
9	Hybrid Code	69
9.1	Introduction	69
9.2	Mass Transfer	70
9.3	Disc Excitation	71
9.4	Pseudo-Force	71
9.5	Spatial Structure	72
9.6	Transition Mass	73
9.7	Boundary Conditions	74
9.8	Validating the Code	75
9.8.1	Energy Balance	75
9.8.2	Coagulation Equation	77
9.8.3	Complete Code Test	77
9.8.4	Statistical Code	81
10	Results	83
10.1	Initial Conditions	83
10.2	Simulations	84
10.2.1	Fragmentation Models	85
10.2.2	Spatial Distribution	86
10.2.3	Resolution	93
10.2.4	Surface Density	94
11	Discussion	101

A Symbols	105
B Central Force – Derivatives	107
C Plummer Model	109
D Scalable Collisions Flux	111
E Coagulation Equation	113
F Computing Facilities	115
G Rendering Planetesimals	117
H Files	119
I New Subroutines	121
J New Variables	123
Bibliography	124
Acknowledgments / Danksagung	133

List of Figures

2.1	Initial planetesimal disc	6
2.2	Evolved planetesimal disc	8
3.1	Hill sphere	15
4.1	Neighbour sphere	21
5.1	Time step ratio for disc systems	28
5.2	Optimal neighbour distance exponents	29
5.3	Timestep distribution	33
5.4	Cumulative irregular block size distribution	34
5.5	Optimal neighbour number	35
6.1	Voronoi tessellation	38
6.2	Impact strength	39
7.1	Fragmentation kernel	46
7.2	Size cut-off due to migration	48
8.1	Δe^2 in three-body encounters	60
8.2	Ordering of protoplanets	65
8.3	Numerical grid	66
9.1	Flow chart of the hybrid code	70
9.2	Gap opening in a planetesimal disc I	72
9.3	Gap opening II	73
9.4	Test simulations T1a–T1c	76
9.5	Test simulations T2a–T2b	76
9.6	Safronov test	77
9.7	Summary of model T4a	78
9.8	Summary of model T4b	78
9.9	Summary of model T4c	78
9.10	Cumulative size distribution of the models T4a–T4c	79
9.11	Eccentricity distribution of the models T4a–T4c	79
9.12	Inclination distribution of the models T4a–T4c	79
9.13	Comparison to Inaba et al. 2001	80
9.14	Simulation of Inaba et al. 2001	81
10.1	Maximum mass for different collision models	87
10.2	Total mass loss for different collision models	87
10.3	Mass in the N -body component for different collision models	87
10.4	Summary of simulation S3FN	88
10.5	Summary of simulation S2FH	89

10.6	Summary of simulation S1FB	90
10.7	Summary of simulation S4FBN	91
10.8	Gap formation at 30,000 years	92
10.9	Gap formation at 100,000 years	92
10.10	Maximum mass for different radial resolutions	93
10.11	Summary of simulation S7FB2	95
10.12	Maximum mass for different surface densities	96
10.13	Mass loss for different surface densities	96
10.14	Mass in the N -body component for different surface densities	96
10.15	Summary of simulation S8_S2	98
10.16	Summary of simulation S9_S100	99
F.1	Images of the used supercomputers	115

Chapter 1

Introduction

The origin of our solar system remains to be one of the most exciting problems of today's astronomy. For a long time it has been the only known planetary system¹. While it is still the only planetary system that can be studied in detail, progress in observation techniques led to the discovery of extrasolar planets and even some extrasolar planetary systems. Thus the wealth of observational data raised the question of how a planetary system forms in general.

Still most planets are detected indirectly by the reflex motion of their host star. The method relies on the overall comparison of the stellar spectrum with a superimposed gauge spectrum (mostly iodine), which allows the precision measurement of the Doppler shift with an accuracy of a few metres per second. Larger velocity amplitudes with a short period are easier to detect, hence radial velocity surveys are biased towards heavy Jupiter-sized planets and favour small semimajor axes, although Neptune-sized planets have been detected recently using this approach (see Butler et al. 2004 [29]). This method gives only the *projected mass* $M \sin(i)$, as long as the inclination i of the planetary system to the plane of the sky is not known. Circumstellar discs, stellar rotation or a transit detection may provide further information on the inclination, but such additional information is only available in a few cases. Pulsar timing uses a similar approach, but the reflex motion is derived from the precise measurement of the pulsar period² that allows even the detection of a few earth masses.

Other indirect detection methods are in progress, like planetary transits and gravitational microlensing. Most of the known planets were detected by 'classical' radial velocity surveys, but the alternative approaches catch up (like OGLE³) and provide first detections. Both methods search for brightness variations that are independent of wavelength, which is a sign of a lensing event or a transit.

The transit method (Charbonneau et al. 2000 [33]) searches for planets passing in front of the host star. As the planet is much fainter, the brightness of the star is reduced during the transit (similar to an eclipsing binary star). The probability of a transit is rather small due to the eclipse geometry, so a survey must automatically monitor a huge sample of stars.

In contrast, the microlensing technique (Paczynski 1996 [117]) searches for lensing events that increase the brightness of a background star during the passage of a lensing star. If the lens is a planetary system, then each planet may also act as a lens which leads to a distinct amplified signal from the background star. However, the small probability of a lensing event requires also a large survey to get a reasonable number of events. While the recent detection of a 5.5 earth mass planet by the OGLE experiment (Beaulieu et al. 2006 [14]) proved the success of this approach, microlensing events are subjected to a severe restriction: They are unique, which excludes the further study and confirmation of the detected planet.

¹We denote any star with more than one planet as a *planetary system*.

²The timing accuracy refers to a velocity error of only a few millimetres per second.

³OGLE, the **O**ptical **G**ravitational **L**ensing **E**xperiment, was originally devoted to the study of microlensing events, but transits are also accessible by this approach. See the project webpage <http://www.astrouw.edu.pl/~ogle> (28/3/2006).

Both methods rely on a large star sample, but they have the capability to detect even terrestrial planets around other stars and could help to complete the planet inventory of the milky way.

High precision astrometry is still far from a routinely detection of extrasolar planets. It is based on the precise measurement of the reflex motion of a star which would reveal an unseen planet. The needed precision of at least a few μas requires a space based mission, but there are currently no operating satellites that meet these requirements. A promising mission is the astrometry satellite GAIA⁴, which is already approved by the ESA. Astrometry already helped determining the planetary masses in some special cases, where the projected mass was already known (Benedict et al. 2002 [16]).

The direct imaging of extrasolar planets is still a technological challenge. Planets are several orders of magnitudes fainter than their host star and are very close to it. Observations in the infrared band improve contrast, but small separations remain a problem due to the diffraction limited resolution of the host star. Therefore first images were obtained from big Jupiter-type planets well separated from the star (see e.g. Chauvin et al. 2005 [35]). The detection of smaller planets requires interferometric techniques like *nulling interferometry*, which suppresses the stellar light by adding two (or more) images with a proper phase shift. While the direct detection of earth-sized planets is theoretically possible, the technological requirements are still far beyond current capabilities. Space-based missions like the TPF/Darwin⁵ project favour an interferometer of free-floating space telescopes. However, the Darwin mission is still in the assessment phase, while the TPF mission has been deferred indefinitely.

All these combined efforts aim at the detection of terrestrial planets in orbits around main sequence stars in the future.

Up to now⁶ 185 planets and 149 planetary systems are known. Most of these planetary systems are very different compared to our solar system. There are *hot Jupiters* very close to their host star, resonant systems as well as planets around pulsars and in multiple stellar systems. The rich observational data helps to overcome the prejudices drawn from our own solar system, but it also demands an explanation of the diversity of extrasolar planets.

Understanding planet formation comprises many challenges, such as hydrodynamics of the protoplanetary disc, chemical evolution of the embedded dust grains, migration of planets and planetesimals and even star-star interactions in dense young star clusters. All these components constitute the frame for the essential process of planet formation: An enormous growth from dust-sized particles to the final planets, accompanied by a steady decrease of the number of particles which contain most of the mass over many orders of magnitude. While this statement leaves all details aside, it points to one major challenge: The particle number changes over many orders of magnitude as planetary growth proceeds. There is active research on each of the different aspects of planet formation, but the current efforts are still far from a unified model of planet formation (Goldreich et al. 2004b [46], Lissauer 1993 [96]).

Our work is devoted to the study of this many-to-few transition from planetesimals to few protoplanets. This stage is of particular interest, as it links the early planetesimal formation to the final planet formation. Collisions still play a major role in the evolution of the system, and the close interplay between the change of the size distribution and the evolution of the random velocities requires a careful treatment of the complete size range.

Small N -body simulations (less than few 10^4 particles) have been useful in exploring the basic growth mechanisms at the price of a modified timescale and an artificially reduced particle number (e.g. Kokubo and Ida 1995 [79], 1996 [80]). Statistical codes explored the limit of large particle numbers in the early phases and are now tentatively applied to the full planet formation process. An efficient solution would be the combination of these two approaches in one hybrid code to unify the advantages of both methods.

⁴The GAIA (Global Astrometric Interferometer for Astrophysics) mission is operated by the European Space Agency (ESA) and the Gaia Science Team (GST). Launch is expected in 2011.

⁵TPF, the Terrestrial Planet Finder, is a study of the National Aeronautics and Space Administration (NASA). Darwin is operated by ESA, launch not expected before 2015.

⁶The Extrasolar Planets Encyclopaedia:
<http://vo.obspm.fr/exoplanets/encyclo/catalog-main.php> (03/04/2006).

We developed a new hybrid code called NBODY6DISC. It combines the NBODY6++ code (a descendant of the widespread N -body family, see Aarseth 1999 [4], Spurzem 1999 [135], Aarseth 2003 [5]) with a new statistical code (see Chapter 8) which uses recent works on the statistical description of planetesimal systems. The new hybrid code includes a consistent modelling of the velocity distribution and the mass spectrum over the whole relevant size range, which allows the application of a detailed collision model beyond the perfect-merger assumption used in previous N -body simulations.

We apply this new code to follow the formation of protoplanets out of 1–10 km sized planetesimals. Before we proceed with the description of the code, Chapter 2 summarises the current status of research on planet formation. Chapter 3 provides the initial setup for our simulations and resumes planetesimal encounters and the protoplanet formation process in more detail. The details of the N -body code, the statistical model and the hybrid code are enclosed in Chapter 4 to 9. Our results are contained in Chapter 10, followed by a summary and discussion of the hybrid code in Chapter 11.

Chapter 2

Planet Formation

2.1 Early Stages

The formation of a planetary system is closely related to the formation of the host star itself. Cool molecular clouds collapse and fragment into smaller substructures which are the seeds for subsequent star formation. Angular momentum conservation in the forming clumps forces the infalling matter into a disc-like structure. The subsequent viscous evolution of the disc leads to a transport of angular momentum which channels gas to the protostar in the centre. These gaseous discs (proplyds – **protoplanetary discs**) are the birth place of the planets.

The first hint to the structure of proplyds has been provided by our own solar system. Through ‘smearing out’ all planets and adding the missing fraction of volatile elements, one can estimate the structure and mass of the protoplanetary disc. Since the efficiency of planet formation is unknown, this yields only a lower limit – the *minimum mass solar nebula* (Hayashi 1981 [52]). The inferred surface density decreases with the distance from the sun as $\propto r^{-3/2}$.

Further insight has been obtained by the detection of an *infrared excess* of some stars, i. e. additional infrared radiation that does not originate from the star but an unseen disc. Since then advancements in observation lead to the direct imaging of nearby star forming regions which opened a new flourishing field in astronomy (see O’dell et al. 1993 [111], who employed Hubble Space Telescope images).

Proplyd masses cover a range from 10^{-3} to $0.1M_{\odot}$ with a peak around $0.01M_{\odot}$ (Data from Taurus/Ophiuchus, Beckwith 1996 [15]), in accordance with mass estimates deduced from the minimum mass solar nebula. Since the disc lifetime can not be measured directly, it is derived indirectly from the age of young, naked (i. e. discless) stars which sets an upper limit on the disc lifetime. Pre-main sequence evolutionary tracks are used to gauge the stellar ages, providing lifetimes of a few 10^6 years. The subsequent evolution of the disc proceeds in several stages.

2.2 Formation of Planetesimals

Two different scenarios have been proposed to explain the formation of kilometre-sized planetesimals. One process is the gravitational instability of the dust component in a proplyd that leads to the direct formation of larger bodies. Goldreich and Ward 1973 [44] propose that an initial growth phase of dust grains leads to a thin dust disc that undergoes a gravitational collapse. As the dense dust layer decouples from the gas, it rotates with the local Keplerian velocity, whereas the gas component rotates slower as it is partially pressure supported. This gives rise to a velocity shear at the boundary, which may excite turbulence through the *Kelvin-Helmholtz-instability*. Since the motion of small dust grains in the boundary layer is coupled to the gas, the turbulent velocity field could suppress the formation of a stratified dust layer, which is a necessary prerequisite for the gravitational instability.

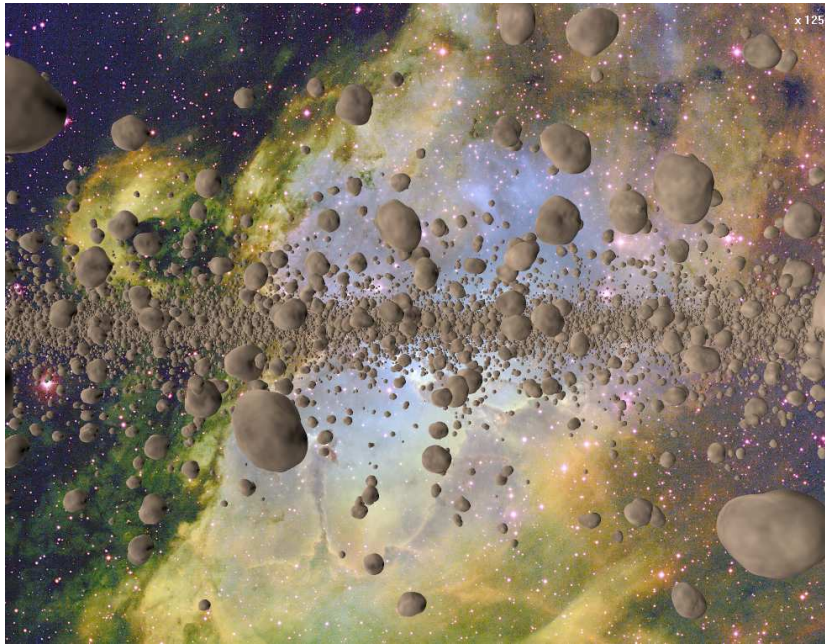


Figure 2.1: Initial planetesimal disc of 10 km–sized bodies roughly enlarged to the size of their Hill sphere for better visibility ($\times 125$). The background is the star-forming region *Eagle Nebula*¹.

The collisional agglomeration of dust particles is an opposed formation mechanism. Relative velocities are dominated by the Brownian motion in the early phases of the growth process. This mechanism becomes increasingly inefficient with growing mass, but successively the particles decouple from the gas and settle to the midplane – a process that yields even larger velocities with increasing mass. The sedimentation initiates a growth mode that is similar to the processes in rain clouds: Larger grains drop faster, thus accreting smaller grains on their way to the midplane. Turbulence may modify this basic growth scenario by forcing the dust grains in a convection-like motion. Dust grains still grow during the settling process, but the turbulent velocity field could mix up dust from the midplane, and a new cycle begins. Each cycle adds a new layer to the dust grains – a mechanism that also operates in hail clouds – until the grains are large enough to decouple from the turbulent motion. Again, turbulence plays an important role in determining the growth mode and the relative velocities. While the relative velocities are high enough to allow for a fast growth, it is not clear *a priori* that collisions are sticky enough to allow for a net growth. High speed encounters lead to fragmentation, which counteracts agglomeration. This issue is still under active research (see e. g. Blum and Wurm 2000 [22] and references therein). An important bottleneck in the agglomeration process is the fast orbital decay of 1 m sized boulders. Their orbital lifetime is as short as 100 years, and a quick increase in size – at least over one order of magnitude – is needed to reduce the radial drift significantly.

To overcome the difficulties associated with each of these scenarios, modifications have been proposed. Recent MHD¹–simulations by Johansen et al. 2006 [71] show that trapping of larger particles in turbulent vortices helps in increasing the orbital lifetime, but could also trigger local instabilities that may lead to the direct formation of planetesimals (Inaba et al. 2005 [69]).

¹Image credit to T. A. Rector (NRAO/AUI/NSF and NOAO/AURA/NSF) and B. A. Wolpa (NOAO/AURA/NSF).

Appendix G provides a brief summary of the image rendering technique and the underlying physics.

¹Magneto-hydrodynamic simulations include electro-magnetic interactions in hydrodynamical calculations. See the reviews of Balbus and Hawley 1998 [11] and Balbus 2003 [12].

While the details of the agglomeration mechanism are still under question (see Kempf et al. 1999 [73]), the successive agglomeration of planetesimals is commonly accepted.

2.3 Formation of Protoplanets

The further growth of planetesimals proceeds through mutual collisions, where the initial phase involves a large number of particles and is thus well described by a coagulation equation (Safronov 1969 [130]). Fig. 2.1 depicts the initial disc with roughly 5 km-sized planetesimals. While earlier works (e.g. Nakagawa et al. 1983 [109]) focussed mainly on the evolution of the size distribution, subsequent refinements of the evolution of the random velocities showed that it is important to evolve the size distribution and the velocity dispersion in a consistent way. A fixed velocity dispersion is an oversimplification, which changes the growth mode and increases the growth timescale as well (Wetherill and Stuart 1989 [150]).

The initial growth is quite democratic. All planetesimals grow roughly at the same rate and the maximum of the size distribution is shifted gently towards larger sizes. As soon as *gravitational focusing* and *dynamical friction* become important, the growth mode changes to a qualitatively different mechanism. Efficient gravitational focusing leads to a *growth timescale*² which decreases with mass. Hence larger bodies grow faster than the smaller planetesimals, a trend that is further supported by energy equipartition due to planetesimal–planetesimal encounters. This *dynamical friction* keeps the largest bodies on nearly circular orbit, thus the relative velocities are small and gravitational focusing remains efficient. Smaller planetesimals are stirred up into eccentricity orbits, which slows down their growth rate compared to the largest bodies. This accelerated growth, denoted as *runaway growth* of planetesimals (see e.g. Greenberg et al. 1978 [47], Wetherill & Stewart 1989 [150], 1993 [151]), shortens the growth timescale to a few 10^5 years. The term *runaway growth* stresses that the *growth timescale* of a particle decreases with mass, hence the largest body ‘runs away’ to the high mass end of the distribution (see Kokubo and Ida 1995 [79]). While energy equipartition increases the velocity dispersion with decreasing mass of the planetesimals, additional damping due to the gaseous disc leads to a turn-over at smaller sizes. However, higher relative velocities may lead nevertheless to destructive encounters, but these *fragmentation events* could even speed up the growth. Since smaller bodies are more subjected to gas drag, their velocity dispersion is smaller which allows an efficient accretion by the runaway bodies. Moreover, smaller particles damp the velocity dispersion of the largest bodies more efficiently.

As runaway proceeds, the system becomes more and more dominated by few big bodies – the *protoplanets* (compare Fig. 2.2). Due to the dominance of few, very large bodies one can not use statistical methods anymore to simulate the problem.

2.4 Oligarchic Growth

The runaway growth of large bodies (i.e. protoplanets) ceases to be efficient as soon as the protoplanets start to control the velocity dispersion of the remaining planetesimals in their vicinity. Gravitational focusing becomes less effective, therefore the growth timescale increases with size and the growth mode changes to *oligarchic growth*. The protoplanets still grow faster than the field planetesimals³, but the masses of the protoplanets remain comparable.

A combination of dynamical friction due to the field planetesimals and perturbations from the neighbouring protoplanets conserves a separation of five to ten Hill radii between neighbouring bodies. Therefore only planetesimals from a limited area, the *feeding zone*, are accreted by a given protoplanet. If this zone is emptied, they have reached their final *isolation mass* (Kokubo and Ida 1998[82], 2000 [84]).

As the damping of the remaining field planetesimals is weak enough, further growth is dominated by mutual perturbations among the protoplanets, which leads to giant impacts. Protoplanets

²We denote M/\dot{M} as the growth timescale.

³The term ‘field planetesimals’ denotes in the following the smooth component of smaller planetesimals.



Figure 2.2: Evolved planetesimal disc after 50,000 years. The protoplanet is larger than 2,000 km, which is well above the sphericity limit. Both illustrations have been generated from simulation S6FBH (see list of all simulations on page 84).

beyond the ‘*snow line*’ (or ice condensation point) can grow larger than 5–15 earth masses and initiate the formation of giant planets. If the protoplanetary disc is very massive in the inner planetary system, this may lead to an in-situ formation of hot Jupiters (see Bodenheimer 2000 [24]).

2.5 Migration

The proposed three-stage scenario of planet formation covers the dominant growth processes, but a major mechanism is still missing – the *migration* of bodies in the system. *Migration* is a generic term that summarises a set of different mechanisms that lead to secular radial drift of bodies (see e.g. the review of Papaloizou and Terquem 2006 [120]):

- The dissipation due to the remaining gas disc leads to an orbital decay of the planetesimals. While this poses a severe problem for 1 m-sized objects, larger bodies drift very slowly inward. One denotes this process as *type 0* migration.
- Planets which are embedded in a gaseous disc launch spiral density waves at the inner and outer *Lindblad resonances*, which leads to an exchange of angular momentum with the resonant excited waves. This *type I* migration leads to a robust inward migration independent of the density profile. The perturbation from the planet is small, hence linear perturbation theory is applicable (Ward 1986 [145]).
- If the protoplanet is massive enough, it opens a gap in the gaseous disc and excites waves through tidal interaction with the gaseous disc. An imbalance of the exchange of angular momentum with the inner and outer part of the disc leads to *type II* migration. The strong interaction between planet and disc leaves the linear regime and requires a numerical solution of the hydrodynamic equations (Lin and Papaloizou 1979 [95]).

- Even with an opened gap, the planet still channels gas between the inner and outer part of the disc. While this *corotational flow* is to some extent already present during type II migration, it dominates the angular momentum balance in the case of *type III* migration due to an asymmetry in the leading and trailing part of the flow. An imbalance allows for an efficient exchange of angular momentum with this corotational gas stream, which gives rise to a remarkably fast migration (Masset and Papaloizou 2003 [102]). Type III migration is subjected to a positive feedback: A faster migration increases the asymmetry in the corotational flow, which speeds up the migration. Both inward and outward migration are possible.

The four migration types modify the three-stage scenario in different ways.

Type 0 migration is most efficient for small planetesimals (i. e. 1 km or smaller). It poses a severe problem during the early stages of planet formation, as it may induce a significant loss of solid material, accompanied by a global change in the initial surface density (Kornet et al. 2001 [88]). The importance of this process diminishes as planetesimal growth proceeds, but it still leads to the loss of collisional fragments during the final disc clearing.

Type I is most important for protoplanets (i. e. 0.1 earth masses or larger). It leads to an orbital decay of protoplanets, but this does not only imply a loss of protoplanets, but also breaks the conditions for isolation. Migrating bodies can accrete along their way through the disc and are thus not constrained to a fixed feeding zone, which may increase the isolation mass.

Type II and *type III* mainly influences giant planets (larger than 10 earth masses) causing an inward or outward migration, depending on the angular momentum exchange balance. It can explain the large number of giant planets close to their host star (*hot Jupiters*) found in extrasolar systems. An important issue is the timescale of the migration process. If the migration is too fast, virtually all planets spiral inward and leave an empty system behind.

Migration is a powerful process with the capability to reshape an entire planetary system. However, it also requires some ‘parking mechanism’ which terminates migration before all planets (or protoplanets) are lost. Inhomogeneities in the gaseous disc may change the crucial momentum balance of the inner and outer part of the disc, thus stalling or even reversing the drift of a planet. The migration processes end after the dissipation of the gaseous disc due to photoevaporation or star-star encounters (i. e. after a few 10^6 to 10^7 years).

2.6 Summary

The formation of a planetary system is a vital process that is driven by the interplay between the different growth phases and the migration of planets and protoplanetary cores (i. e. the precursors of giant planets). While the preceding sections only summarised the main evolutionary processes, even more processes could influence the formation of planetary systems. A fast accretion of giant planets in the outer parts of a planetary system could introduce further perturbations on the inner part and may even trigger the formation of terrestrial planets. Moreover, the stellar environment in dense star clusters and multiple stellar systems also perturbs planet formation, which would require an even broader view on the problem.

Any approach to planet formation can hardly include this wealth of different phenomena, thus it is important to focus on a well-defined subproblem. We selected the formation of protoplanets for the following reasons:

- The size, growth timescale and spacing of the protoplanets is a key element in the planet formation process.
- The protoplanet growth is well-defined by different growth modes. It starts with the already formed planetesimals ($\approx 1\text{--}5$ km) and ends, when orbital crossing of the protoplanets initiates the final growth phase.
- The planetesimals are large enough to treat the remaining gaseous disc as a small perturbation.

- The protoplanets are small enough to neglect tidal interaction with the disc in the inner planetary system. Collective planetesimal–protoplanet interaction are also negligible.

Though the protoplanet formation is a well-posed subproblem, our approach has to incorporate various mechanisms and techniques to cover the full size range of the problem. However, it is still accessible to theoretical calculations to some extent which provide a safe ground for the analysis of the results.

Chapter 3

Theory

3.1 Solar Nebula

The basis for all planet formation models is the structure of the protoplanetary disc. We summarise the pioneering work of Hayashi 1981 [52] to have a robust initial model at hand. Subsequent evolution of the disc may change this simple approach, but it is still a valuable guideline.

A basic estimate of the minimum surface density of solid material in the disc can be deduced from the mass and location of the present planets in the solar system:

$$\Sigma_{\text{solid}}(r) = \begin{cases} 7.1 (r/1\text{AU})^{-3/2} \text{ g/cm}^2 & \text{for } 0.35 \leq r \leq 2.7 \\ 30.0 (r/1\text{AU})^{-3/2} \text{ g/cm}^2 & \text{for } 2.70 \leq r \leq 36.0 \end{cases} \quad (3.1)$$

The discontinuity at 2.7 AU stems from the location of the ice condensation point (or *snow line*), that allows the formation of icy grains in the outer solar system. Furthermore, the total surface density is estimated through the chemical composition of the disc, which gives the ratio of gas to solids. A fiducial value is 1:0.017 (see Cameron 1973 [30]). The surface density of the gas component is therefore:

$$\Sigma_{\text{gas}}(r) = 1700 \left(\frac{r}{1\text{AU}} \right)^{-3/2} \frac{\text{g}}{\text{cm}^2} \quad (3.2)$$

Since the dust content is rather low, the gaseous component is transparent to the visible solar radiation. Thus the gas temperature follows from the radiation balance:

$$T = T_0 \left(\frac{r}{1\text{AU}} \right)^{-1/2} \left(\frac{L}{L_\odot} \right)^{1/4} \quad T_0 = 280 \text{ K} \quad (3.3)$$

L is the solar luminosity during the early stages, normalised by the present value L_\odot . The three-dimensional density structure is given by an isothermal profile

$$\rho_{\text{gas}}(r, z) = \frac{\Sigma_{\text{gas}}}{\sqrt{2\pi}h} \exp\left(-\frac{z^2}{2h^2}\right) \quad (3.4)$$

with a radially changing *scale height* h :

$$h = \frac{c_s}{\Omega} \quad c_s = \left(\frac{k_B T}{\mu m_H} \right)^{1/2} \quad \mu = 2.34 \quad (3.5)$$

$$= \frac{c_s^{(0)}}{\Omega_0} \left(\frac{r}{1\text{AU}} \right)^{5/4} \left(\frac{L}{L_\odot} \right)^{1/8} \quad c_s^{(0)} = 993.56 \frac{\text{m}}{\text{s}} \quad (3.6)$$

c_s is the sound velocity of an ideal gas with a mean molecular weight μ in units of the hydrogen mass m_H .

Since the density profile is related to a radially varying pressure, the gas velocity deviates from the local Keplerian velocity. The balance of forces relates the angular velocity Ω_g to the pressure gradient:

$$r\Omega_g^2 = r\Omega^2 + \frac{1}{\rho} \frac{dP}{dr} \quad (3.7)$$

Thus the angular velocity Ω_g of the gas is (see e. g. Adachi 1976 [6]):

$$\Omega_g = \Omega \sqrt{1 - 2\eta_g(r)} \quad (3.8)$$

$$\eta_g = -\frac{1}{2} \frac{d \ln(\rho_{\text{gas}} c_s^2)}{d \ln(r)} \left(\frac{c_s}{v_K} \right)^2 \quad (3.9)$$

It is more appropriate to formulate the rotation of the gaseous disc in terms of a velocity lag Δv_g normalised to the local Keplerian velocity v_K :

$$\Delta v_g = r(\Omega_g - \Omega) \quad (3.10)$$

$$\approx -\eta_g v_K \quad (3.11)$$

A typical value of Δv_g for the minimum mass solar nebula at 1 AU is $\Delta v_g = -60$ m/s.

This simple model provides a brief description of the initial disc. However, the subsequent evolution further modifies the structure of the protoplanetary disc. Since embedded dust grains are coupled to the gas, it is likely that a global migration of solid material changes the surface density. Moreover, the dust grains are chemically processed, depending on the local temperature and composition which introduces additional spatial inhomogeneities. When the growing particles pass the critical size of ~ 1 metre, the strong onset of radial migration may lead to a final reshaping of the distribution of solid material. While these restrictions weaken the validity of this approach as the ‘true’ initial model, it is still a robust guideline to choose reasonable surface densities for the solid and the gaseous component after the formation of planetesimals.

3.2 Kepler Orbits

Planetesimals in a protoplanetary disc are subjected to various perturbations: Close encounters change their orbits, a small but steady gas drag gives rise to a radial drift and accretion changes the mass of the planetesimals. While all these processes drive the disc evolution on a timescale of at least a few thousand years, each planetesimal moves most of the time on an orbit close to an unperturbed Kepler ellipse. Though the protoplanetary disc introduces additional perturbations, the central potential dominates for typical disc masses around $0.01 M_\odot$. Therefore the classical orbital elements still provide a proper framework to study planetesimal dynamics.

The orbital elements of a test particle moving around a mass M are:

$$E = \frac{v^2}{2} - \frac{GM}{r} \quad (3.12) \quad \mathbf{L} = \mathbf{r} \times \mathbf{v} \quad (3.16)$$

$$a = -\frac{GM}{2E} \quad (3.13) \quad e \cos(\phi_E) = \frac{rv^2}{GM} - 1 \quad (3.17)$$

$$e = \sqrt{1 - \frac{L^2}{GMa}} \quad (3.14) \quad e \sin(\phi_E) = \frac{\mathbf{r} \cdot \mathbf{v}}{\sqrt{GMa}} \quad (3.18)$$

$$\cos(i) = \frac{L_z}{L} \quad (3.15)$$

a is the semimajor axis, e is the eccentricity and i is the inclination of the orbit. As long as no dominant body is structuring the protoplanetary disc, it is justified to assume axisymmetry.

Hence the argument of the perihelion ω , the longitude of the ascending node Ω and the eccentric anomaly ϕ_E are omitted in the statistical description.

The deviation of planetesimal orbits from a circle is quite small. Thus it is appropriate to expand the above set of equations. A planetesimal at a distance r_0 , in a distance z above the midplane and with a velocity (v_r, v_ϕ, v_z) with respect to the local circular velocity v_K has orbital elements (leading order only):

$$a \approx r_0 + 2 \frac{r_0 v_\phi}{v_K} \quad (3.19)$$

$$e^2 \approx \frac{v_r^2 + 4v_\phi^2}{v_K^2} \quad (3.20)$$

$$i^2 \approx \frac{z^2}{r_0^2} + \frac{v_z^2}{v_K^2} \quad (3.21)$$

These expressions allow a convenient transformation between the statistical representation through orbital elements and the utilisation of a velocity distribution function.

3.3 Hill's Problem

When two planetesimals pass by each other, they exchange energy and angular momentum and separate with modified orbital elements. Successive encounters transfer energy between planetesimals with different masses, driving an evolution of the overall velocity distribution.

It seems that an encounter is a two-body problem, as there are only two planetesimals involved, but the central mass has also a major influence turning the problem into a *three-body encounter*¹. The complexity of the problem is considerably simplified by reducing it to Hill's problem (Hill 1878 [56]).

Consider two masses m_1 and m_2 that orbit a much larger mass M_c , where both masses are small compared to the central mass M_c . The mass ratio $m_1 : m_2$ could be arbitrary. This special type of a three body problem is denoted as Hill's problem, originally devised to calculate the orbit of the moon. It provides a convenient framework to examine planetesimal encounters in the potential of a star. The equations of motion² of the two planetesimals including the central potential and their mutual interaction are:

$$\ddot{\mathbf{r}}_1 = -\mathbf{r}_1 \frac{GM_c}{r_1^3} - (\mathbf{r}_1 - \mathbf{r}_2) \frac{Gm_2}{r_{12}^3} \quad (3.22)$$

$$\ddot{\mathbf{r}}_2 = -\mathbf{r}_2 \frac{GM_c}{r_2^3} - (\mathbf{r}_2 - \mathbf{r}_1) \frac{Gm_1}{r_{12}^3} \quad (3.23)$$

It is appropriate to introduce the relative vector \mathbf{r} and the centre of mass \mathbf{R} :

$$\mathbf{r} = \mathbf{r}_2 - \mathbf{r}_1 \quad \mathbf{R} = \frac{m_2 \mathbf{r}_2 + m_1 \mathbf{r}_1}{m_1 + m_2} \quad (3.24)$$

Furthermore, the equations of motion are transformed to a corotating set of coordinates which are

¹The term *three-body encounter* does not imply a close passage of all involved bodies, but emphasises the strong influence of a third one.

²The following derivation is quite common to the literature, see e. g. Ida 1990 [61] or Hénon and Petit 1986 [54]. The later paper uses a slightly different scaling.

scaled by the *mutual Hill radius* r_{Hill} and the local Kepler frequency Ω

$$x = \frac{r' - a_0}{r_{\text{Hill}}} \quad (3.25)$$

$$y = \frac{a_0(\phi - \Omega t)}{r_{\text{Hill}}} \quad (3.26)$$

$$z = \frac{z'}{r_{\text{Hill}}} \quad (3.27)$$

$$r_{\text{Hill}} = a_0 \sqrt[3]{\frac{m_1 + m_2}{3M_c}} \quad (3.28)$$

where (r', ϕ, z') are heliocentric cylindrical coordinates. a_0 is the radius of a properly chosen reference orbit, while the *mutual Hill radius* r_{Hill} provides an intrinsic length scale of the problem (its meaning is clarified in the following). As the two orbiting planetesimals are small compared to the central star, the Hill radius is much smaller than the size a_0 of the reference orbit. Hence it is possible to expand the central potential about the reference orbit. This yields approximate equations for the relative motion and the centre of mass:

$$\left. \begin{aligned} \ddot{x} &= 2\dot{y} + 3x - 3x/r^3 \\ \ddot{y} &= -2\dot{x} - 3y/r^3 \\ \ddot{z} &= -z - 3z/r^3 \end{aligned} \right\} \quad (3.29) \quad \left. \begin{aligned} \ddot{X} &= 2\dot{Y} + 3X \\ \ddot{Y} &= -2\dot{X} \\ \ddot{Z} &= -Z \end{aligned} \right\} \quad (3.30)$$

The equations 3.29 and 3.30 have some interesting properties: Firstly, the centre of mass motion separates from the interaction of the two bodies. Secondly, the scaled relative motion is independent of the masses m_1 and m_2 , implying a fundamental similarity of planetesimal encounters³. As Eq. 3.30 is a simple linear differential equation, one readily obtains the solution of the centre of mass motion

$$\left. \begin{aligned} X &= b - e \cos(t - \tau) \\ Y &= -\frac{3}{2}bt + \psi + 2e \sin(t - \tau) \\ Z &= i \sin(t - \omega) \end{aligned} \right\} \quad (3.31)$$

which is equivalent to a first-order expansion of a Kepler ellipse. ω and τ are the longitudes of the ascending node and the pericentre, while e and i are the eccentricity and inclination scaled by the *reduced* (i. e. dimensionless) *Hill radius* r_{Hill}/a_0 . The value of b depends on the choice of the reference orbit, but it is natural to set $b = 0$ which implies that the centre of mass defines the reference orbit.

While the nonlinear nature of the relative motion (see Eq. 3.29) prevents any general analytical solution, Eq. 3.31 provides at least an asymptotic solution for a large separation of the planetesimals, where b can be interpreted as an *impact parameter*. Small b do not necessarily imply close encounters, as opposed to the standard definition of the impact parameter. However, the expression $b = a_2 - a_1$ provides a measure of the distance of the two colliding bodies without invoking the complicated encounter geometry. A special solution to Eq. 3.29 are the unstable equilibrium points L_1 and L_2 at $(x, y, z) = (\pm 1, 0, 0)$, denoted as *Lagrange points*⁴. In addition, an inspection of Eq. 3.29 reveals that the *Jacobi energy* E_J is conserved:

$$E_J = \frac{1}{2}(\dot{x}^2 + \dot{y}^2 + \dot{z}^2 + z^2 - 3x^2) - \frac{3}{r} \quad (3.32)$$

Since the kinetic energy is always a positive quantity, the following inequality holds:

$$E_J \geq U \quad (3.33)$$

$$U = \frac{1}{2}(z^2 - 3x^2) - \frac{3}{r} \quad (3.34)$$

³Chapter 8 makes extensive use of this property.

⁴The additional Lagrange points L_3 – L_5 are missing due to the Hill approximation.

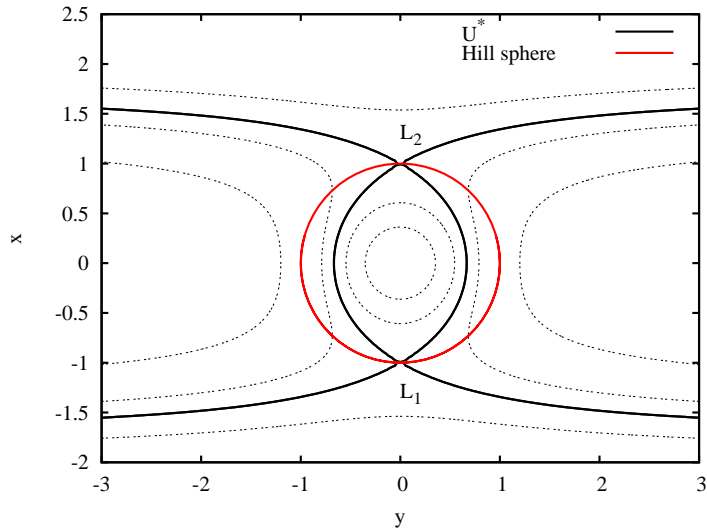


Figure 3.1: Equipotential lines for the effective potential U at $z = 0$ (see Eq. 3.34). $U = U^*$ refers to the largest allowed volume, which is enclosed by the Hill sphere and the two Lagrange points L_1 and L_2 .

Thus the allowed domain of the particle motion is enclosed by the equipotential surfaces of the effective potential U . A subset of these equipotential surfaces restricts the allowed domain to the vicinity of the origin (see Fig. 3.1). The largest of these surfaces passes through the Lagrange points L_1 and L_2 . Hence we identify the Hill radius (or Hill sphere) as the maximum separation which allows the bound motion of two planetesimals⁵.

Beside the numerical solution of the equations of motion, it is useful to define *osculating* (or *instantaneous*) orbital elements

$$b = 4x + 2\dot{y} \quad (3.35) \quad \psi = -2\dot{x} + y + \frac{3}{2}bt \quad (3.38)$$

$$i^2 = z^2 + \dot{z}^2 \quad (3.36) \quad \omega = t - \arctan(z, \dot{z}) \quad (3.39)$$

$$e^2 = \dot{x}^2 + (3x + 2\dot{y})^2 \quad (3.37) \quad \tau = t - \arctan(\dot{x}, 3x + 2\dot{y}) \quad (3.40)$$

$$E_J = \frac{1}{2}(e^2 + i^2) - \frac{3}{8}b^2 - \frac{3}{r} \quad (3.41)$$

which provide a convenient summary of the initial relative orbit and the modified orbit after the encounter.

3.4 Protoplanet Growth

Our work follows the evolution of a planetesimal disc into few protoplanets, including the full set of interaction processes. Hence we summarise the main aspects of protoplanet growth first to provide a robust framework.

Although the sizes of the planetesimal cover a wide range, they virtually form two main groups: The smaller field planetesimals and the embedded protoplanets (or their precursors). This *two-group approximation* (e.g. Wetherill and Stewart 1989 [150], Ida and Makino 1993b [64]) allows a clearer insight into the growth process.

⁵The same argument applies to the tidal boundary in cluster dynamics or the Roche lobe in stellar dynamics, which are equivalent to the Hill sphere.

During the initial phase all planetesimals share the same velocity dispersion independent of their mass. The initial random velocities are low enough to allow for an efficient gravitational focusing. Hence the growth rate of a protoplanet with mass M and radius R can be estimated as (e. g. Ida and Makino 1993 [63]):

$$\dot{M} \approx v_{\text{rel}} \frac{\Sigma}{H} \pi R^2 \left(1 + \frac{2GM}{Rv_{\text{rel}}^2} \right) \quad (3.42)$$

Eq. 3.42 is the *two-body accretion rate*, which should be modified due to the gravity of the central star. Nevertheless this approximation gives an appropriate description to discuss the basic properties of the growth mode. The scale height H (Eq. 8.16) and the relative velocity v_{rel} are related to the mean eccentricity $e_m = \sqrt{\langle e^2 \rangle}$ of the field planetesimals:

$$H \approx v_{\text{rel}}/\Omega \quad v_{\text{rel}} \approx e_m a \Omega \quad (3.43)$$

Thus the accretion rate in the limit of strong gravitational focusing ($2GM/R \gg v_{\text{rel}}^2$) is:

$$\dot{M} \approx 2\pi R \frac{\Sigma GM}{a^2 \Omega e_m^2} \quad (3.44)$$

$$\propto M^{4/3} \quad (3.45)$$

If the protoplanets are massive enough, they start to control the velocity dispersion of the planetesimals in their vicinity. The width Δa of this sphere of influence, the *heating zone*, is related to the Hill radius R_{Hill} of the protoplanet (see Ida and Makino 1993b [64]):

$$\Delta a = \Delta \tilde{a} R_{\text{Hill}} = 4R_{\text{Hill}} \sqrt{\frac{4}{3}(\tilde{e}_m^2 + \tilde{i}_m^2) + 12} \quad (3.46)$$

$$h = \sqrt[3]{\frac{M}{3M_c}} \quad (3.47)$$

\tilde{e}_m and \tilde{i} are eccentricity and inclination of the field planetesimals, scaled by the *reduced Hill radius* h of the protoplanet. M_c is the mass of the central star. The condition that the protoplanet controls the velocity dispersion of the field planetesimals reads (see Ida and Makino 1993 [63]):

$$\frac{2M^2}{2\pi a \Delta a} > \Sigma m \quad (3.48)$$

This condition is equivalent to a lower limit of the protoplanetary mass:

$$\frac{M}{m} > \left(\frac{\pi \Delta \tilde{a}}{\sqrt[3]{3}} \right)^{3/5} \left(\frac{\Sigma a^2}{M_c} \right)^{3/5} \left(\frac{m}{M_c} \right)^{3/5} \quad (3.49)$$

M/m depends on several parameters, but reasonable values yield $M/m \approx 50$ – 100 . The velocity dispersion in the heated region is roughly

$$v \approx R_{\text{Hill}} \Omega \quad (3.50)$$

which gives an interesting relation to the condition that leads to *gap formation*. A protoplanet can open a gap in the planetesimal component if it is larger than a critical mass M_{gap} (Rafikov 2001 [125])

$$M_{\text{gap}}/M_c \approx \begin{cases} \frac{\Sigma a^2}{M_c} \left(\frac{m}{M_c} \right)^{1/3} & \text{for } v \lesssim \Omega r_{\text{Hill}} \\ \frac{\Sigma a^2}{M_c} \left(\frac{m}{M_c} \right)^{1/3} \left(\frac{\Omega r_{\text{Hill}}}{v} \right)^2 & \text{for } v \gg \Omega r_{\text{Hill}} \end{cases} \quad (3.51)$$

where r_{Hill} is the Hill radius of the field planetesimals. If the velocity dispersion v is controlled by the protoplanet, Eq. 3.51 together with Eq. 3.50 demonstrate that the condition for gap formation

is equivalent to Eq. 3.49, i. e. the efficient heating of the field planetesimals implies gap formation and vice versa. The higher velocity dispersion of the field planetesimals (see Eq. 3.50) reduces the growth rate given by equation 3.44 to

$$\dot{M} \approx 6\pi\Sigma\Omega\frac{RR_{\text{Hill}}}{\tilde{e}_m^2} \quad (3.52)$$

$$\propto M^{2/3} \quad (3.53)$$

Different mass accretion rates imply different growth mode. If two protoplanets have different masses M_1 and M_2 , their mass ratio evolves as:

$$\frac{d}{dt} \frac{M_2}{M_1} = \frac{M_2}{M_1} \left(\frac{\dot{M}_2}{M_2} - \frac{\dot{M}_1}{M_1} \right) \quad (3.54)$$

When the growth timescale M/\dot{M} decreases with mass, a small mass difference increases with time. This is the case for Eq. 3.44, which gives rise to *runaway accretion*. As soon as the protoplanets control the velocity dispersion of the field planetesimals, the growth timescale increases with mass and therefore the protoplanet masses become more similar as they grow *oligarchically*.

The field planetesimals also damp the excitation due to protoplanet–protoplanet interactions and keep them on nearly circular orbits. The balance between these scatterings and the dynamical friction due to smaller bodies establishes a roughly constant orbital separation b (Kokubo and Ida 1997 [81]):

$$b = R_{\text{Hill}} \sqrt[5]{\frac{7\tilde{e}_m^2 M}{2\pi\Sigma a R}} \quad (3.55)$$

$$\tilde{b} = b/R_{\text{Hill}} \quad (3.56)$$

R is the radius of the protoplanet, M is its mass and \tilde{e} is the reduced eccentricity of the field planetesimals. The stabilised spacing prevents collisions between protoplanets, but it also restricts the *feeding zone* – the area from which a protoplanet accretes. If all matter in the feeding zone is accreted by the protoplanet, it reaches its final *isolation mass* (Kokubo and Ida 2000 [84]):

$$M_{\text{iso}} = 2\pi b a \Sigma \quad (3.57)$$

Inserting Eq. 3.55 yields the isolation mass in units of the mass of the host star M_c :

$$M_{\text{iso}}/M_c = (112\pi^4)^{3/8} \left(\frac{1}{3}\right)^{5/8} \left(\frac{4\pi}{3}\right)^{1/8} (\tilde{e}_m^2)^{3/8} \left(\frac{a^2\Sigma}{M_c}\right)^{3/2} \left(\frac{a^3\rho}{M_c}\right)^{1/8} \quad (3.58)$$

$$\approx 19.67 \times (\tilde{e}_m^2)^{3/8} \left(\frac{a^2\Sigma}{M_c}\right)^{3/2} \left(\frac{a^3\rho}{M_c}\right)^{1/8} \quad (3.59)$$

There is a weak dependence on the density ρ of the protoplanet, but the most important parameter by far is the surface density Σ . If we take the minimum mass solar nebula as an example, the radial dependence of the surface density implies an isolation mass that grows with increasing distance to the host star. Hence protoplanets beyond some critical radial distance are massive enough (larger than $\approx 15 M_{\oplus}$, Bodenheimer and Pollack 1986 [23]) to initiate gas accretion from the protoplanetary disc.

As the protoplanets approach the isolation mass, interactions with the gaseous disc and neighbouring protoplanets become increasingly important. We estimate the onset of orbit crossing by a comparison of the perturbation timescale τ_{pert} of protoplanet–protoplanet interactions with the damping timescale τ_{damp} due to planetesimal–protoplanet scatterings. Since the protoplanets are

$\Sigma[\text{g}/\text{cm}^2]$	M_{iso}/M_{\odot}	$M_{\text{iso}}/M_{\oplus}$
2	3.91×10^{-8}	0.013
10	4.33×10^{-7}	0.144
100	1.37×10^{-5}	4.548

Table 3.1: Isolation mass for different surface densities at $r = 1$ AU and $M_c = 1 M_{\odot}$.

well separated ($\tilde{b} \approx 5 \dots 10$), it is possible to apply perturbation theory (see e. g. Petit and Hénon 1986 [121]):

$$\tau_{\text{pert}} \approx \frac{\tilde{b}^5}{7h\Omega} \quad (3.60)$$

We anticipate Chapter 8 (see Eq. 8.25) to derive the damping timescale

$$\tau_{\text{damp}} \approx \frac{1}{2} \frac{T_r^{3/2}}{\sqrt{2\pi}G^2 \ln(\Lambda)(M+m)n_0m} \quad (3.61)$$

where T_r and T_z are the radial and vertical velocity dispersion of the field planetesimals. Hence the criterion for the onset of orbital crossing is:

$$\tau_{\text{pert}} < \tau_{\text{damp}} \quad (3.62)$$

As the protoplanets control the velocity dispersion of the field planetesimals (see Eq. 3.50), this condition reduces to:

$$\Sigma_M > \Sigma_m \ln(\Lambda) \frac{72}{7\pi} \left(\frac{\tilde{b}}{\tilde{e}} \right)^4 \quad (3.63)$$

$$> \Sigma_m \times f \quad (3.64)$$

Thus orbital crossing sets in when the mean surface density Σ_M of the protoplanets exceeds some fraction f of the field planetesimal density Σ_m . While the factor f depends strongly on the separation \tilde{b} of the protoplanets, a fiducial value is $f \approx 1$, in agreement with the estimates of Goldreich et al. 2004 [45].

The onset of migration and the resonant interaction of protoplanets with the disc and other protoplanets terminates the local nature of the protoplanet accretion process and requires a global evolution of the planetary system. While the final stage deserves a careful analysis, further research is beyond the scope of this work.

Chapter 4

Integrator

4.1 NBODY6++

The protoplanet formation is essentially an N -body problem. Although we seek for a more elaborated solution to this problem which benefits from statistical methods, the pure N -body approach is a logical starting point. Direct calculations with a few thousand bodies have provided valuable insight into the growth mode (see e.g. Ida and Makino 1992 [62], Kokubo and Ida 1996 [80]), but they are also powerful guidelines that help developing other techniques. Statistical calculations invoke quite a number of approximations, and ‘exact’ N -body calculations provide the necessary, unbiased validation of the derived formula.

The choice of the integrator is a key element in the numerical solution of the equations of motion. Our requirements are the stable long-term integration of few ten thousand planetesimals with the capability of treating close encounters, collisions and the perspective to evolve it into an improved hybrid code. Approximative methods like the Fast Multipole Method or Tree codes provide a scaling of the computational time close to N , but the accuracy in this regime is too poor to guarantee the stable integration of Keplerian orbits (compare the discussion in Hernquist et al. 1993 [55], Spurzem 1999 [135]).

The class of exact methods (all scale asymptotically with N^2) roughly divides in two parts:

Symplectic methods (see Wisdom and Holman 1991 [152] or the SYMBA code, Duncan et al. 1998 [40]) rely on a careful expansion of the Hamiltonian which guarantees that the numerical integration follows a perturbed Hamiltonian. While there is still an integration error, all properties of a Hamiltonian system like conservation of phase-space volume are conserved by the numerical integration. The drawback of these very elegant methods is that the symplecticity is immediately broken by adaptive time steps, collisions or complicated external forces if no special precaution is taken. Even the numerical truncation error breaks the symplecticity to some extent (see Skeel 1999 [132]).

The second group represents the ‘classical’ methods that are based on Taylor expansions of the solution. They come in different flavours like implicit methods, predictor–corrector integrators or iterated schemes. Time symmetric methods stand out among these different approaches, as they show no secular drift in the energy error. These integrators are so well-behaved, that one may even call them ‘nearly symplectic’.

Taking all the requirements into account we have chosen NBODY6++¹, an integrator which is the most recent descendant from the famous N -body code family from S. Aarseth’s ‘factory’. This version was parallelised by Spurzem 1999 [135], which opened the use of current supercomputers.

The plain NBODY6++ version offers many versatile features that were included over the past years and more and more refined as time passed by. While all these elaborated tools deserve advertisement, we restrict ourselves for brevity to the components which contribute to the planetesimal

¹Aarseth 1999 [4] gives a nice review on the remarkable history of the NBODY-codes, more details are given in Aarseth 2003 [5].

problem. The main components of the code are:

- Individual time steps and a block time step scheme.
- Ahmad–Cohen neighbour scheme.
- Hermite scheme.
- KS–Regularisation for close two-body encounters.

The following sections explain each of these features, while the parallelisation is discussed in more detail in Chapter 5.

4.2 Individual Time Steps

The choice of the time step controls the accuracy as well as the efficiency of any given integrator. Too small time steps slow down the integration without necessity, whereas too large values increase the error. An efficient solution to this dilemma is an *adaptive time step* that is adjusted after each integration step according to a specified accuracy limit. While the idea is quite clear, there is no unique receipt how to choose the proper time step. A common approach for N -body systems is to use the parameters at hand (like particle velocity, force, etc.) to derive a timescale of the particle motion. This procedure leaves enough space for a wealth of different time step criteria. NBODY6++ uses the standard Aarseth expression (Aarseth 1985 [2])

$$\Delta t = \sqrt{\eta \frac{F F^{(2)} + (F^{(1)})^2}{F^{(1)} F^{(3)} + (F^{(2)})^2}} \quad (4.1)$$

which makes use of the force and the time derivatives up to third order.

The time step choice is not unique in multi-particle systems. One solution is to take the minimum of all these values as a *shared (or global) time step*, but this is not recommended unless all individual steps are of the same size.

The second option is to evolve each particle track with its own, *individual time step*. This method abandons the convenient synchronisation provided by a global step, therefore each integration of a particle demands a synchronisation of all particles through predictions. Since the prediction of all particles is $\mathcal{O}(N)$, it is outbalanced by the saving of force computations. Nevertheless the overhead is still significant, so a further optimisation might be desired. The basic idea of the *block time step* method is to force particles in groups that are integrated together, which reduces the number of necessary predictions by a factor comparable to the mean group size. These groups are enforced through two constraints. The first condition is a discretisation of the steps in powers of two:

$$\Delta t = 2^{-k} \quad k \geq 0 \quad (4.2)$$

This condition increases the chances that two different particles share the same timelevel, but it also reduces roundoff errors since the time steps are now exactly representable numbers. The second condition locks the ‘phases’ of particles with the same time step

$$T_i \equiv 0 \pmod{\Delta t_i} \quad (4.3)$$

i. e. the particle time T_i is an integer multiple of the actual time step Δt_i so that all particles with the same step share the same block. Note that a step can not be increased at any time T_i , but only when the second condition (Eq. 4.3) for the larger step is met.

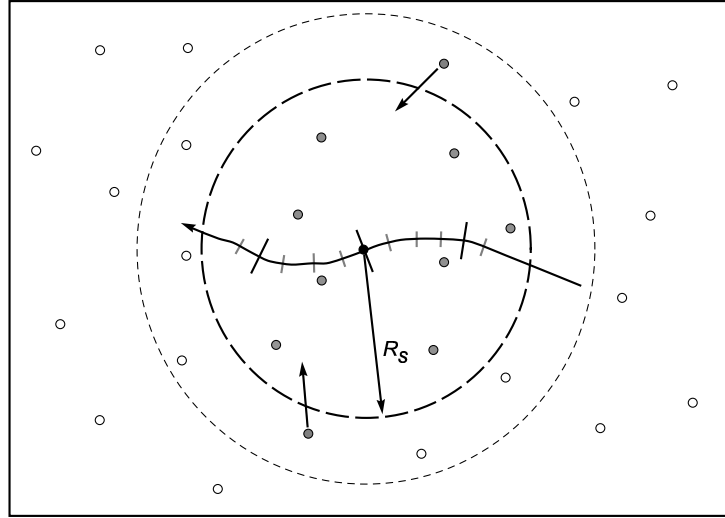


Figure 4.1: All particles inside the neighbour sphere R_s are selected as neighbours (filled circles). As the neighbour list is fixed during regular steps (marked by black lines), a second shell includes possible intruders.

4.3 Ahmad-Cohen Neighbour Scheme

The first N -body codes calculated always the full force (i. e. summation over all particles) to integrate a particle. But not all particles contribute with the same weight to the total force. Distant particles provide a smooth, slowly varying *regular force*, whereas the neighbouring particles form a rapidly changing environment which gives rise to an *irregular force*. The Ahmad-Cohen neighbour scheme (Ahmad and Cohen 1973 [7]) takes advantage of this spatial hierarchy by dividing the surrounding particles in the already mentioned two groups according to the *neighbour sphere radius* R_s . Both partial forces fluctuate on different timescales, which are calculated according to Eq. 4.1. The key to the efficiency of the method is the inequality

$$\Delta t_{\text{irr}} < \Delta t_{\text{reg}} \quad (4.4)$$

Regular forces are extrapolated between two full force calculations

$$\mathbf{F}_{\text{reg}} = \mathbf{F}_{\text{reg}}^{(0)} + \Delta t \mathbf{F}_{\text{reg}}^{(1)} + \frac{1}{2}(\Delta t)^2 \mathbf{F}_{\text{reg}}^{(2)} + \frac{1}{6}(\Delta t)^3 \mathbf{F}_{\text{reg}}^{(3)} \quad (4.5)$$

with a third order accurate expression, whereas the plain NBODY6++ uses only linear extrapolation (see the next sections for a detailed discussion).

4.4 Hermite Scheme

The *Hermite scheme* is a fourth-order accurate integrator that was applied first by Makino and Aarseth 1992 [99] to the integration of a planetesimal system. This scheme is used to integrate single particles and CM-bodies² in the main body of NBODY6++. It is accomplished by a predictor and a corrector step. The prediction is second order accurate:

$$\mathbf{x}_p = \mathbf{x}_0 + \mathbf{v}_0 \Delta t + \frac{1}{2} \mathbf{a}_0 (\Delta t)^2 + \frac{1}{6} \dot{\mathbf{a}}_0 (\Delta t)^3 \quad (4.6)$$

$$\mathbf{v}_p = \mathbf{v}_0 + \mathbf{a}_0 \Delta t + \frac{1}{2} \dot{\mathbf{a}}_0 (\Delta t)^2 \quad (4.7)$$

²CM denotes centre-of-mass, see the section on KS-Regularisation for more details.

Now the acceleration is evaluated at the predicted position to derive the second and third order time derivatives of the force:

$$\mathbf{a}_0^{(2)} = \frac{-4\dot{\mathbf{a}}_0 - 2\dot{\mathbf{a}}_p}{\Delta t} + \frac{-6\mathbf{a}_0 + 6\mathbf{a}_p}{\Delta t^2} \quad (4.8)$$

$$\mathbf{a}_0^{(3)} = \frac{6\ddot{\mathbf{a}}_0 + 6\ddot{\mathbf{a}}_p}{\Delta t^2} + \frac{12\mathbf{a}_0 - 12\mathbf{a}_p}{\Delta t^3} \quad (4.9)$$

Using the additional derivatives one can improve the prediction:

$$\mathbf{x}_c = \mathbf{x}_p + \frac{1}{24}\mathbf{a}_0^{(2)}(\Delta t)^4 + \frac{1}{120}\mathbf{a}_0^{(3)}(\Delta t)^5 + \mathcal{O}(\Delta t^6) \quad (4.10)$$

$$= \mathbf{x}_p + \left(-\frac{3}{20}\mathbf{a}_0 + \frac{3}{20}\mathbf{a}_p\right)(\Delta t)^2 - \left(\frac{7}{60}\dot{\mathbf{a}}_0 + \frac{1}{30}\dot{\mathbf{a}}_p\right)(\Delta t)^3 + \mathcal{O}(\Delta t^6) \quad (4.11)$$

$$\mathbf{v}_c = \mathbf{v}_p + \frac{1}{6}\mathbf{a}_0^{(2)}(\Delta t)^3 + \frac{1}{24}\mathbf{a}_0^{(3)}(\Delta t)^4 + \mathcal{O}(\Delta t^5) \quad (4.12)$$

$$= \mathbf{v}_p + \frac{1}{2}(-\mathbf{a}_0 + \mathbf{a}_p)\Delta t + \left(-\frac{5}{12}\dot{\mathbf{a}}_0 - \frac{1}{12}\dot{\mathbf{a}}_p\right)(\Delta t)^2 + \mathcal{O}(\Delta t^5) \quad (4.13)$$

The corrected positions are fourth order accurate. While the Hermite scheme is robust and stable, even in combination with the neighbour scheme, it is not accurate enough to integrate planetesimal orbits efficiently.

4.5 Hermite Iteration

The Hermite scheme bears the potential for a powerful extension, since it is a predictor–corrector scheme. An essential part of this scheme is the calculation of the new forces with the predicted positions, but it should improve the accuracy if they are recalculated using the corrected positions. The new forces are readily used to improve the corrected values, which closes the scheme to an iteration loop – the *Hermite iteration* (see Kokubo et al. 1998 [82]).

There are only few modifications necessary to obtain the iterated scheme. The particle prediction remains second-order accurate:

$$\mathbf{x}_p = \mathbf{x}_0 + \mathbf{v}_0\Delta t + \frac{1}{2}\mathbf{a}_0(\Delta t)^2 + \frac{1}{6}\dot{\mathbf{a}}_0(\Delta t)^3 \quad (4.14)$$

$$\mathbf{v}_p = \mathbf{v}_0 + \mathbf{a}_0\Delta t + \frac{1}{2}\dot{\mathbf{a}}_0(\Delta t)^2 \quad (4.15)$$

The force and its first time derivative are calculated to derive higher derivatives according to Eq. 4.8 and 4.9:

$$\mathbf{a}_p = \mathbf{f}(\mathbf{x}_p, \mathbf{v}_p) \quad (4.16)$$

$$\dot{\mathbf{a}}_p = \mathbf{f}(\mathbf{x}_p, \mathbf{v}_p) \quad (4.17)$$

The new corrector omits the highest order term in the position, making the velocity and the position to the same order accurate:

$$\begin{aligned} \mathbf{x}_c &= \mathbf{x}_p + \frac{1}{24}\mathbf{a}_0^{(2)}(\Delta t)^4 + \mathcal{O}(\Delta t^5) \\ &= \mathbf{x}_p + \frac{1}{4}(\mathbf{a}_p - \mathbf{a}_0)(\Delta t)^2 + \left(-\frac{1}{6}\dot{\mathbf{a}}_0 - \frac{1}{12}\dot{\mathbf{a}}_p\right)(\Delta t)^3 + \mathcal{O}(\Delta t^5) \end{aligned} \quad (4.18)$$

$$\mathbf{v}_c = \mathbf{v}_p + \frac{1}{2}(-\mathbf{a}_0 + \mathbf{a}_p)\Delta t + \left(-\frac{5}{12}\dot{\mathbf{a}}_0 - \frac{1}{12}\dot{\mathbf{a}}_p\right)(\Delta t)^2 + \mathcal{O}(\Delta t^5) \quad (4.19)$$

It seems unreasonable to drop one order in the position, but a reformulation of the predictor–corrector step reveals that this slight change yields a time symmetric scheme:

$$\mathbf{v}_c = \mathbf{v}_0 + \frac{1}{2}(\mathbf{a}_p + \mathbf{a}_0)\Delta t - \frac{1}{12}(\dot{\mathbf{a}}_p - \dot{\mathbf{a}}_0)(\Delta t)^2 \quad (4.20)$$

$$\mathbf{x}_c = \mathbf{x}_0 + \frac{1}{2}(\mathbf{v}_c + \mathbf{v}_0)\Delta t - \frac{1}{12}(\mathbf{a}_p - \mathbf{a}_0)(\Delta t)^2 \quad (4.21)$$

The iteration is achieved by returning to Eq. 4.16–4.17 with the predicted positions replaced by the more accurate values $\mathbf{x}_c, \mathbf{v}_c$. Although the integration does not need the second and third time derivative of the forces explicitly, it is useful to provide them at the end of the iteration for the calculation of the new time step:

$$\mathbf{a}^{(2)}(t + \Delta t) = \frac{2\dot{\mathbf{a}}_0 + 4\dot{\mathbf{a}}_p}{\Delta t} + \frac{6\mathbf{a}_0 - 6\mathbf{a}_p}{\Delta t^2} \quad (4.22)$$

$$\mathbf{a}^{(3)}(t + \Delta t) = \frac{6\ddot{\mathbf{a}}_0 + 6\ddot{\mathbf{a}}_p}{\Delta t^2} + \frac{12\mathbf{a}_0 - 12\mathbf{a}_p}{\Delta t^3} \quad (4.23)$$

Numerical tests show that convergence is reached after one or two iterations, making this approach very efficient. It needs less force evaluations than the Hermite scheme for the same accuracy. Moreover, its time symmetry suppresses a secular drift of the energy error.

4.6 Extended Hermite Scheme

The Hermite scheme is an integral part of NBODY6++ and proved its value in many applications. It would have been natural to improve the performance with an additional iteration, but our first tentative implementations showed disastrous results: The iterated scheme was more unstable, slower and even less accurate than the plain Hermite scheme. An inspection of the code structure revealed that the Ahmad–Cohen neighbour scheme is the cause of this surprising behaviour.

The conflict is the following:

Each particle integration is composed of two parts – frequent neighbour force evaluations and less frequent total force evaluations including corrections. Every regular correction leads to an additional change in the position of a particle, which introduces a spurious discontinuity in the neighbour force and its derivatives. The Hermite iteration reacts to this artificial jump in two ways: It increases the regular correction, and – what is more important – it amplifies any spurious error during the iteration which leads to the extreme unstable behaviour.

Since the Hermite iteration is a key element in the efficient integration of planetesimal orbits, we sought for a modification of the Hermite scheme that circumvents the depicted instability. The problem gives already an indication to a possible solution. A scheme with much smaller corrections would not suffer from the feedback of spurious errors.

NBODY6++ stores already the second and third time derivative of the forces for the time step calculation. A manifest application of these derivatives at hand is the improvement of the predictions to fourth order:

$$\begin{aligned} \mathbf{x}_p &= \mathbf{x}_0 + \mathbf{v}_0\Delta t + \frac{1}{2}\mathbf{a}_0(\Delta t)^2 + \frac{1}{6}\dot{\mathbf{a}}_0(\Delta t)^3 \\ &\quad + \frac{1}{24}\mathbf{a}_0^{(2)}(\Delta t)^4 + \frac{1}{120}\mathbf{a}_0^{(3)}(\Delta t)^5 \end{aligned} \quad (4.24)$$

$$\begin{aligned} \mathbf{v}_p &= \mathbf{v}_0 + \mathbf{a}_0\Delta t + \frac{1}{2}\dot{\mathbf{a}}_0(\Delta t)^2 \\ &\quad + \frac{1}{6}\mathbf{a}_0^{(2)}(\Delta t)^3 + \frac{1}{24}\mathbf{a}_0^{(3)}(\Delta t)^4 \end{aligned} \quad (4.25)$$

Again, the new forces \mathbf{a}_p and $\dot{\mathbf{a}}_p$ are calculated to improve \mathbf{x}_p and \mathbf{v}_p – but with a modified corrector:

$$\mathbf{a}_p = \mathbf{f}(\mathbf{x}_p, \mathbf{v}_p) \quad (4.26)$$

$$\dot{\mathbf{a}}_p = \mathbf{f}(\mathbf{x}_p, \mathbf{v}_p) \quad (4.27)$$

$$\mathbf{a}_n^{(2)}(t) = \frac{-4\dot{\mathbf{a}}_0 - 2\dot{\mathbf{a}}_p}{\Delta t} + \frac{-6\mathbf{a}_0 + 6\mathbf{a}_p}{\Delta t^2} \quad (4.28)$$

$$\mathbf{a}_n^{(3)}(t) = \frac{6\dot{\mathbf{a}}_0 + 6\dot{\mathbf{a}}_p}{\Delta t^2} + \frac{12\mathbf{a}_0 - 12\mathbf{a}_p}{\Delta t^3} \quad (4.29)$$

$$\mathbf{x}_c = \mathbf{x}_p + \frac{1}{24}(\mathbf{a}_n^{(2)} - \mathbf{a}_0^{(2)})(\Delta t)^4 + \frac{1}{120}(\mathbf{a}_n^{(3)} - \mathbf{a}_0^{(3)})(\Delta t)^5 \quad (4.30)$$

$$\mathbf{v}_c = \mathbf{v}_p + \frac{1}{6}(\mathbf{a}_n^{(2)} - \mathbf{a}_0^{(2)})(\Delta t)^3 + \frac{1}{24}(\mathbf{a}_n^{(3)} - \mathbf{a}_0^{(3)})(\Delta t)^4 \quad (4.31)$$

Finally, the derivatives are updated:

$$\mathbf{a}_0(t + \Delta t) = \mathbf{a}_p \quad (4.32)$$

$$\dot{\mathbf{a}}_0(t + \Delta t) = \dot{\mathbf{a}}_p \quad (4.33)$$

$$\mathbf{a}_0^{(2)}(t + \Delta t) = \mathbf{a}_n^{(2)} + \Delta t \mathbf{a}_n^{(3)} \quad (4.34)$$

$$\mathbf{a}_0^{(3)}(t + \Delta t) = \mathbf{a}_n^{(3)} \quad (4.35)$$

The new scheme has an appealing property, which is related to the usage of the higher force derivatives. As the predictor is fourth-order accurate, it is equivalent to one full Hermite step. Since the corrector uses new forces to improve the two highest orders, it is equivalent to a first iteration step. Thus we obtained a one-fold iterated Hermite scheme at no extra cost. This *extended Hermite scheme* reduces the energy error by three orders of magnitude, compared to the plain NBODY6++ with the same number of force evaluations.

4.7 KS-Regularisation

Two bodies which undergo a close encounter are integrated in a special set of regular coordinates, that separates the relative motion from the motion of the centre of mass. A close encounter poses a numerical problem due to the singularity of the gravitational forces at zero separation. While the growing force amplifies roundoff errors as the two bodies approach each other closely, the collision is only an apparent singularity since the analytic solution stays well defined. This opens the possibility of a proper coordinate transformation which removes the singularity from the equations of motion. The Kustaanheimo–Stiefel (Kustaanheimo and Stiefel 1965 [91]) regularisation takes advantage a four-dimensional set of variables to transform the Kepler problem into a harmonic oscillator. Perturbations are readily included in the new set of equations of motion.

The centre of mass is added as a pseudo-particle, the *CM-body*, which is integrated as a normal particle plus a perturbation force due to the deviation from a point mass. See e.g. Mikkola 1997 [107] or Mikkola and Aarseth 1998 [108] for more details.

4.8 Additional Forces

NBODY6++ only includes the gravitational interaction of all particles, therefore additional forces have to be included manually. A planetesimal disc requires two new forces: The presence of a central star introduces an additional central potential, while the gaseous component of the protoplanetary disc is the source of a friction force. It is important that the new forces are properly included in the neighbour scheme to assure that regular steps remain larger than irregular steps. Since a dissipative force breaks the energy conservation, one has to integrate the energy loss as well to maintain a valid energy error control.

4.8.1 Central Potential

A star is much heavier than a planetesimal. Thus the central star is introduced as a spatially fixed Keplerian potential:

$$\Phi_c = -\frac{GM_c}{r} \quad \mathbf{F} = -\frac{GmM_c \mathbf{x}}{|\mathbf{x}|^3} \quad (4.36)$$

Since the orbital motion of the planetesimals sets the dominant (and largest) dynamical timescale in the system, we included the central force as a component of the regular force. Moreover, the central potential also introduces a strong synchronisation, since planetesimals in a narrow ring share virtually the same regular block time step.

4.8.2 Drag Force

As the whole planetesimal system is embedded in a dilute gaseous disc, each planetesimal is subjected to a small, but noticeable drag force. The drag regime³ depends on the gas density and the size of the planetesimals. Kilometer-sized planetesimals are subjected to the deceleration

$$\frac{d\mathbf{v}}{dt} = -\frac{\pi C_D}{2m} \rho_{\text{gas}} R^2 |\mathbf{v} - \mathbf{v}_g| (\mathbf{v} - \mathbf{v}_g) \quad (4.37)$$

$$C_D = 0.5 \quad (4.38)$$

which is anti-proportional to the radius $R(m)$ of the planetesimal in this drag regime. v_g is the rotational velocity of the gaseous disc, which rotates slower than the planetesimal system as it is partially pressure supported. The drag force leads to an orbital decay \dot{a} of the semimajor axis of a planetesimals:

$$\dot{a} = -\frac{3}{4} C_D \frac{\rho_{\text{gas}} \langle (\Delta v)^2 \rangle}{\rho_{\text{Body}} R(m) \Omega} \quad (4.39)$$

Thus smaller particles migrate faster, with a maximum at $R \approx 1$ m. Even smaller bodies couple to the gas, which reduces the effective drag force. The dissipation rate and its time derivative are:

$$W_{\text{drag}} = \mathbf{F}_{\text{drag}} \cdot \mathbf{v} \quad (4.40)$$

$$\dot{W}_{\text{drag}} = \dot{\mathbf{F}}_{\text{drag}} \cdot \mathbf{v} + \mathbf{F}_{\text{drag}} \cdot \mathbf{F}_{\text{tot}} \quad (4.41)$$

We integrate the dissipation rate W_{drag} to maintain a valid energy error:

$$\Delta E = \int_{t_1}^{t_2} W_{\text{drag}} dt \quad (4.42)$$

$$\Delta t = t_2 - t_1 \quad (4.43)$$

$$\Delta E = \frac{1}{2} (W_{\text{drag},1} + W_{\text{drag},2}) \Delta t + \frac{1}{12} (\dot{W}_{\text{drag},1} - \dot{W}_{\text{drag},2}) \Delta t^2 + \mathcal{O}(\Delta t^5) \quad (4.44)$$

The expression is fourth order accurate in accordance with the order of the extended Hermite scheme.

³The main drag regimes are Stokes (laminar flow), Epstein (mean free molecular path larger than object size) and Newton's drag law (turbulent flow). Weidenschilling 1977 [146] provides a nice review on the different drag regimes.

4.8.3 KS-Pairs

Both new forces also demand a modification of the regularisation treatment. They perturb the relative motion of a KS-pair and modify the orbit of the centre of mass. While the modification of the equations of motion is rather clear, the neighbour scheme requires some additional work. Let $\mathbf{r}_1, \mathbf{r}_2$ be the positions of the two regularised particles. The equations of motion read ($G = 1$)

$$\mathbf{r} = \mathbf{r}_2 - \mathbf{r}_1 \quad (4.45)$$

$$\ddot{\mathbf{r}}_1 = -M_c \frac{\mathbf{r}_1}{r_1^3} + m_2 \frac{\mathbf{r}}{r^3} + \mathbf{F}_{\text{drag},1} \quad (4.46)$$

$$\ddot{\mathbf{r}}_2 = -M_c \frac{\mathbf{r}_2}{r_2^3} - m_1 \frac{\mathbf{r}}{r^3} + \mathbf{F}_{\text{drag},2} \quad (4.47)$$

where the perturbations by other particles are omitted for clarity. Centre of mass motion and the orbital motion are separated:

$$\ddot{\mathbf{r}} = -M \frac{\mathbf{r}}{r^3} - M_c \frac{\mathbf{r}_2}{r_2^3} + M_c \frac{\mathbf{r}_1}{r_1^3} + \mathbf{F}_{\text{drag},2} - \mathbf{F}_{\text{drag},1} \quad (4.48)$$

$$\ddot{\mathbf{R}} = -M_c \frac{m_1}{M} \frac{\mathbf{r}_1}{r_1^3} - M_c \frac{m_2}{M} \frac{\mathbf{r}_2}{r_2^3} + \frac{m_1}{M} \mathbf{F}_{\text{drag},1} + \frac{m_2}{M} \mathbf{F}_{\text{drag},2} \quad (4.49)$$

$$\mathbf{r} = \mathbf{r}_2 - \mathbf{r}_1 \quad M = m_1 + m_2 \quad (4.50)$$

$$\mathbf{R} = \frac{1}{M} (m_1 \mathbf{r}_1 + m_2 \mathbf{r}_2) \quad (4.51)$$

Two new contributions show up due to the external forces: The KS-pair is tidally perturbed by the central star and influenced by the gaseous disc. While the aerodynamic properties of a single particle are well understood, two bodies revolving about each other may induce complex gas flows in their vicinity, which could invalidate the linear combination of the drag forces on each component. Therefore we drop the drag force term to avoid spurious dissipation. Since the dynamic environment allows virtually no stable binaries⁴ in a planetesimal disc, the influence of the drag force on the encounter dynamics is negligible.

We further decompose the additional acceleration of the centre of mass motion, since the neighbour scheme benefits from a clear separation of the timescales. Therefore the tidal perturbation is split in a smooth mean force and a perturbation force:

$$\ddot{\mathbf{R}} = \mathbf{F}_{\text{mean}} + \mathbf{F}_{\text{pert}} \quad (4.52)$$

$$\mathbf{F}_{\text{mean}} = -M_c \frac{\mathbf{R}}{R^3} \quad (4.53)$$

$$\mathbf{F}_{\text{pert}} = M_c \frac{\mathbf{R}}{R^3} - M_c \frac{m_1}{M} \frac{\mathbf{r}_1}{r_1^3} - M_c \frac{m_2}{M} \frac{\mathbf{r}_2}{r_2^3} \quad (4.54)$$

$$= 0 + \mathcal{O}(r^2) \quad (4.55)$$

The mean forces varies on the orbital timescale and is therefore included as a regular force component, while the perturbation is treated as an irregular force as it changes with the internal orbital period of the pair.

⁴Tidal capturing of moons starts in the late stages of planet formation, but is limited to the planets or their precursors. However, the quiescent conditions in an early Kuiper belt allow for a more prominent role of binaries. See the summary of Astakhov et al. 2005 [9].

Chapter 5

Optimising the Code

5.1 Introduction

An astrophysical simulation is a tool to analyse problems and predict dynamical systems, which are not accessible to experiments. The design of a new simulation tool does not only require the careful implementation of the invoked physics, but also an analysis of the code performance to make best use of the available hardware.

We applied NBODY6++ for the first time to planet formation, a subject that is quite different to stellar clusters. The central star forces the planetesimals on regular orbits which need higher accuracy than the random motion of stars in a cluster. In addition, the orbital motion also introduces a strong synchronisation among the planetesimals, thus allowing a more efficient integration. We examine the differences due to the integration of a disc system in the following sections and summarise our achieved optimisations.

5.2 Disc Geometry and Neighbour Scheme

The introduction of the neighbour scheme by Ahmad and Cohen 1973 [7] has provided a technique to save a considerable amount of computational time in star cluster simulations. Since the average ratio of the regular to the irregular time step γ_t is of the order of 10, the integration is speeded up by the same factor. One may expect a similar speedup for planetesimal systems, but it turned out that the time step ratio is roughly three in this case. The time step is calculated with the standard Aarseth time step criterion

$$\Delta t = \sqrt{\eta \frac{FF^{(2)} + (F^{(1)})^2}{F^{(1)}F^{(3)} + (F^{(2)})^2}} \quad (5.1)$$

where $F^{(i)}$ are the force and its time derivatives. It is applied to the calculation of the regular step using the regular force and accordingly to the irregular step taking the irregular force. The regular time step of a particle orbiting the central mass M_c at a distance r_0 is:

$$\Delta t_r = \sqrt{\eta_r} \frac{1}{\Omega} \quad \Omega = \sqrt{\frac{GM_c}{r_0^3}} \quad (5.2)$$

For simplicity, we introduce the scaled timestep ratio $\tilde{\gamma}_t = \gamma_t \sqrt{\eta_{\text{irr}}/\eta_{\text{reg}}}$. The free parameters of the problem are the mean particle distance \bar{r} , the velocity dispersion σ_v (additional to the Keplerian shear), the particle mass m_i and the neighbour number N_{nb} . We employ Hill's approximation for the central potential and obtain:

$$\Delta t_i \approx \frac{\sqrt{\eta_i}}{\Omega} f(\Omega, r_{\text{Hill}}, \bar{r}, \sigma_v, N_{\text{nb}}) \quad r_{\text{Hill}} = r_0 \sqrt[3]{\frac{2m_i}{3M_c}} \quad (5.3)$$

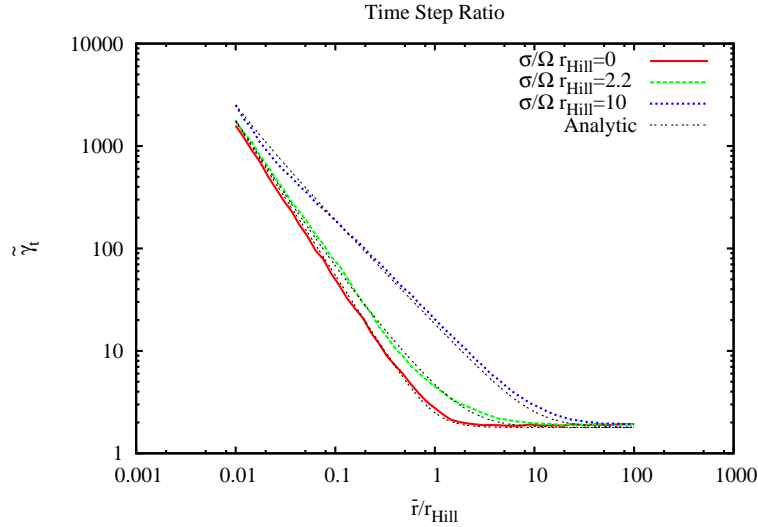


Figure 5.1: Time step ratio for $N_{\text{nb}} = 100$. Curves are plotted for different values of $\sigma_v/(r_{\text{Hill}}\Omega)$. The dotted line is approximation Eq. 5.6.

f is a yet unknown function. Dimensional analysis leads to

$$\Delta t_i \approx \frac{\sqrt{\eta_i}}{\Omega} f\left(\frac{\sigma_v}{r_{\text{Hill}}\Omega}, \frac{\bar{r}}{r_{\text{Hill}}}, N_{\text{nb}}\right) \quad (5.4)$$

$$\tilde{\gamma}_t \approx f\left(\frac{\sigma_v}{r_{\text{Hill}}\Omega}, \frac{\bar{r}}{r_{\text{Hill}}}, N_{\text{nb}}\right) \quad (5.5)$$

which shows that the time step ratio is essentially controlled by the interparticle distance and the velocity dispersion. We generated different random realisations of planetesimal discs with different densities and velocity dispersions to cover the range of possible values. The neighbour number is fixed at $N_{\text{nb}} = 100$ to reduce the noise due to small number statistics, but γ_t converges to a value independent of the neighbour number already for $N_{\text{nb}} > 10$. Fig. 5.1 shows the numerical calculation of the time step ratio for various values of \bar{r} and σ_v . A good approximation to the calculated values of $\tilde{\gamma}_t$ is:

$$\tilde{\gamma}_t \approx 1.79 \times \sqrt{1 + 1.03 \frac{\sigma_v^2}{\bar{r}^2 \Omega^2} + 0.94 \frac{r_{\text{Hill}}^3}{\bar{r}^3}} \quad (5.6)$$

Planetesimal discs have usually a small velocity dispersion (compared to the orbital velocity) and a low density in terms of the Hill radius, which leaves a major influence to the Keplerian shear. Since the shear motion is directly linked to the local Keplerian frequency, this synchronisation reduces γ_t to values smaller than ten. The numerical calculations show larger time step ratios with increasing velocity dispersion and for high densities¹, but planetesimal discs are far from these extreme parameter values.

5.3 Optimal Neighbour Criterion

The standard neighbour criterion uses the geometrical distance: Particles are neighbours if their distance to the reference particle is smaller than a limit R_s . This criterion is simple and probably the best choice for an equal mass system. However, a multi-mass system may require a different

¹ $\bar{r}/r_{\text{Hill}} < 1$ corresponds to an unstable self-gravitating disc.

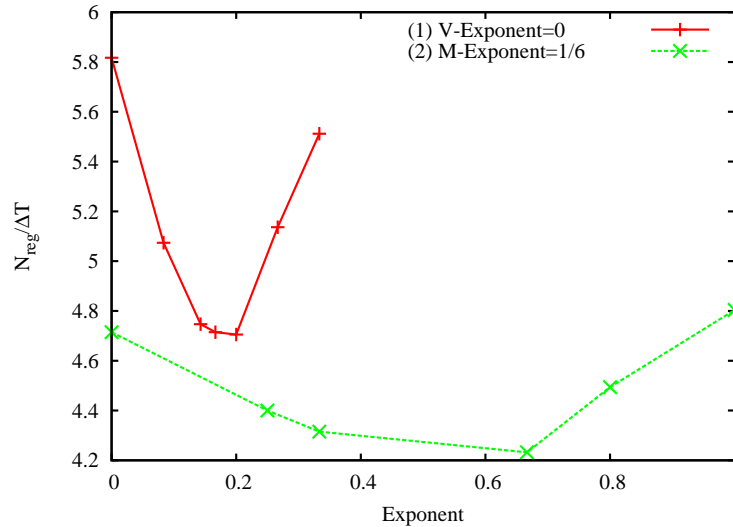


Figure 5.2: Regular steps per particle and per 1 N -body time in the inner core ($R_i < 0.5$) of a 5000 particle plummer model. Plotted are (1) different mass exponents with velocity exponent 0 and (2) different velocity exponents with mass exponent 1/6.

criterion, since a massive particle outside the neighbour sphere could have a stronger influence than lighter particles inside the neighbour sphere. A more appropriate selection should rely on some ‘perturbation strength’ of a particle.

It turned out that a better criterion is the magnitude of the fourth time derivative of the pairwise force $F_{ij}^{(4)}$, i. e. those particles are selected as neighbours which produce the largest integration error in accordance with the Hermite scheme. $F_{ij}^{(4)}$ is a complicated expression (compare Appendix B), but the leading term can be estimated via dimensional analysis:

$$F_{ij}^{(4)} \propto \frac{m_j v_{ij}^4}{r_{ij}^6} \quad (5.7)$$

We use this expression to define a new *apparent distance* between the integrated particle i and a neighbour j :

$$r_{\text{app}} = r_{ij} \left(\frac{m_i}{m_j} \right)^{1/6} \left(\frac{v_s}{v_{ij}} \right)^{2/3} \quad (5.8)$$

v_s is an arbitrary scaling velocity to obtain a distance with dimension length. This new distance definition moves massive or fast neighbours to an apparently smaller distance, thus enforcing that these particles are preferentially included in the neighbour list. In addition, the modified distance is readily included in the conventional neighbour scheme. We tested different mass and velocity exponents to verify that Eq. 5.8 is the optimal choice. Figure 5.2 shows that these exponents are indeed the optimal choice for a Plummer model² with mass spectrum. The new scheme saves 25% of the force evaluations in the core, but the impact on a planetesimals system is smaller, as it is the case for the neighbour scheme. While a velocity dependent distance reduces the number of necessary full force evaluations, it introduces a distance changing with time which destabilises the integration. The result is a much larger energy error compared to the achieved speedup. Therefore we only recommend the mass modification of the apparent distance.

²Appendix C provides a brief summary of the Plummer model.

5.4 Neighbour Changes

The rate at which the neighbours of a given particle change has a noticeable influence on the accuracy of the code. During the course of an integration the second and third time derivative of the regular and irregular force are calculated from an interpolation formula (see Eq. 4.8 and Eq. 4.9). Whenever a particle leaves (or enters) the neighbour sphere, these derivatives are corrected by analytic expressions³. Hence many neighbour changes lead to a pronounced spurious difference.

We estimated the rate at which particles cross the neighbour sphere boundary to quantify this effect. Neighbour changes are due to the Keplerian shear and the superimposed random velocities of the particles. The two effects lead to:

$$N^{+/-} = \Delta t_r \frac{N_{\text{nb}}}{T_{\text{orb}}} \quad \text{Shear} \quad (5.9)$$

$$\begin{aligned} N^{+/-} &= \frac{3}{2} \Delta t_r N_{\text{nb}} \frac{\sigma_v}{R_{\text{nb}}} \\ &= \Delta t_r \frac{N_{\text{nb}}}{T_{\text{orb}}} \frac{3\pi\sigma_v}{R_{\text{nb}}\Omega} \quad \text{Dispersion} \end{aligned} \quad (5.10)$$

R_{nb} and N_{nb} are the neighbour sphere radius and the neighbour number, respectively. In practice, the neighbour changes due to the shear account for up to 80% of the total neighbour changes. The standard regular time step $\Delta t_r = 2^{-5}$ and 50 neighbours yield a change of one particle per regular step, which is fairly safe.

5.5 Neighbour Prediction

Each integration step is preceded by the prediction of all neighbours of the particles that are due. A regular step requires the full prediction of all particles, so there is no possibility to save computing time. In contrast, an irregular step calculates only neighbour forces, which requires the prediction of less particles. Thus the prediction of all particles to prepare an irregular step is a simple, but, depending on the block size, computational costly solution. It seems to be more efficient to predict only the required particles, but random access to the particle data and the complete check of all neighbour list entries introduces an additional overhead. Therefore large block sizes should favour the first approach, whereas the second approach is more suitable for small block sizes.

Both regimes are separated by a critical block size N_{irr}^* . If N_{irr} particles with $\langle N_{\text{nb}} \rangle$ neighbours are due, then only N_{merge} particles need to be predicted:

$$N_{\text{merge}} \approx N_{\text{tot}} \left(1 - \exp \left(- \frac{N_{\text{irr}} \langle N_{\text{nb}} \rangle}{N_{\text{tot}}} \right) \right) \leq N_{\text{irr}} \langle N_{\text{nb}} \rangle \quad (5.11)$$

The size N_{merge} of the merged neighbour lists is smaller than the total number of neighbour list entries, since some particles are by chance members of more than one neighbour list. Performance measurements show that the prediction of the merged neighbour lists is 10 % more costly (per particle) than the full prediction, mainly due to additional sorting and a random memory access. Thus N_{irr}^* satisfies:

$$N_{\text{tot}} = 1.1 \times N_{\text{merge}} \quad (5.12)$$

Inserting Eq. 5.11 yields the critical block size:

$$N_{\text{irr}}^* \approx 2.4 \frac{N_{\text{tot}}}{\langle N_{\text{nb}} \rangle} \quad (5.13)$$

The prediction mode is chosen according to the actual block size.

³Appendix B gives a complete set of the force derivatives up to third order.

Process	0	1	2	3	4	5	6	7
Send to	1	2	3	4	5	6	7	0
Receive from	7	0	1	2	3	4	5	6

Table 5.1: Ring Communication. Communication partners are fixed, while the exchanged data varies. $n_p - 1$ cycles are needed.

Cycle	Process	0	1	2	3	4	5	6	7
1	Exchange with	1	0	3	2	5	4	7	6
2	Exchange with	2	3	0	1	6	7	4	5
3	Exchange with	4	5	6	7	0	1	2	3

Table 5.2: Hierarchical Communication. Communication partners change after every cycle. The exchanged data amount doubles with every new cycle, hence only $\ln_2(n_p)$ cycles are needed.

5.6 Communication Scheme

NBODY6++ is parallelised using a *copy algorithm*. A complete copy of the particle data is located on each node, so the integration step of one particle does not need any communication. Therefore a block of N_{bl} particles is divided in n_p parts (n_p is the processor number), which are integrated by different processors in parallel. The integration step is completed by an all-to-all communication of the different subblocks to synchronise the particle data on all nodes. Hence the amount of communicated data is proportional to $N_{\text{bl}} \times n_p$. A communication in a ring-like fashion (see table 5.1) needs $n_p - 1$ communication cycles, but a hierarchical scheme (see table 5.2) sends the same amount of data with only $\ln_2(n_p)$ communication cycles. The difference between the two approaches remains small, as long as the communication is bandwidth limited, i. e. the blocks are large. Small block sizes shift the bottleneck to the latency, which is significantly reduced by the second scheme – especially if the code runs on many processors.

A hierarchical scheme reduces the latency, but nevertheless it is possible that the parallel integration is actually slower than a single CPU integration. We estimated both the runtime on one CPU and on a parallel machine to explore the transition between these two regimes. The latency time τ_l per communication is included in the wallclock time expressions for one regular/irregular step:

$$\tau_l = \alpha A \quad (5.14)$$

$$t_{\text{single}} = \alpha N_{\text{bl}} N_{\text{nb}} \quad (5.15)$$

$$t_{\text{par}} = \alpha \left(\underbrace{\frac{N_{\text{bl}} N_{\text{nb}}}{n_p}}_{\text{Arithmetic}} + \underbrace{A \ln_2(n_p)}_{\text{Latency}} + \underbrace{B N_{\text{bl}}}_{\text{Communication}} \right) \quad (5.16)$$

Block	n_p	$\alpha [\mu\text{s}]$	$\tau_l [\mu\text{s}]$	A	B
Irregular	10	0.35	51	145	4.5
Regular	10	0.22	113	512	40
Irregular	20	0.35	308	877	8.8
Regular	20	0.22	368	1668	75

Table 5.3: Timings on Hydra. See text for an explanation of the variables. Timings are obtained for a maximal neighbour number LMAX=64. In practice, B is twice as large due to storage rearrangements in NBODY6++. See Appendix F for details on the computers.

Block	n_p	$\alpha[\mu\text{s}]$	$\tau_l[\mu\text{s}]$	A	B
Irregular	8	0.29	255	837	1.7
Regular	8	0.60	981	1763	4.1
Irregular	16	0.28	188	700	1.7
Regular	16	0.60	306	561	6.7
Irregular	64	0.27	241	887	7.7
Regular	64	0.46	401	871	21.7

Table 5.4: Timings on the IBM. More than 32 processors require more than one node.

If t_{single} (runtime on a single CPU) is equal to t_{par} (parallel computation), one can deduce the critical block size N_{min} which gives the minimal block size for efficient parallelisation:

$$t_{\text{single}} = t_{\text{par}} \quad (5.17)$$

$$N_{\text{min}} = \frac{A \ln_2(n_p) n_p}{N_{\text{nb}}(n_p - 1) - B n_p} \quad (5.18)$$

The hierarchical communication gives a minimal block size that increases logarithmically with the processor number. Eq. 5.16 gives immediately the speedup S and the optimal processor number for a certain block size N_{bl} :

$$S = \frac{n_p}{1 + A n_p \frac{\ln_2(n_p)}{N_{\text{bl}} N_{\text{nb}}} + B \frac{n_p}{N_{\text{nb}}}} \quad (5.19)$$

$$n_{p,\text{opt}}(N_{\text{bl}}) = \frac{\ln(2) N_{\text{bl}} \times N_{\text{nb}}}{A} \quad \text{Hierarchical Communication} \quad (5.20)$$

A comparison to the optimal processor number for a ring communication

$$n_{p,\text{opt}}(N_{\text{bl}}) = \sqrt{\frac{N_{\text{bl}} \times N_{\text{nb}}}{A}} \quad \text{Ring Communication} \quad (5.21)$$

$$t_{\text{par}} = \alpha \left(\frac{N_{\text{bl}} N_{\text{nb}}}{n_p} + A n_p + B N_{\text{bl}} \right) \quad (5.22)$$

stresses the efficiency of the hierarchical communication, since it allows a much larger processor number for a given problem size. Equation 5.15 and 5.16 are also useful to derive the total wallclock time, since the total runtime scales with the number of regular and irregular blocks:

$$N_{\text{reg}} \approx T \frac{N^{1/3}}{N_{\text{nb}}^{1/3} \sqrt{\eta_{\text{reg}}}} \quad (5.23)$$

$$N_{\text{irr}} \approx T \frac{N^{1/3}}{\sqrt{\eta_{\text{irr}}}} \quad (5.24)$$

These equations are only approximate expressions, but they give the right order of magnitude without detailed calculations that need a precise knowledge of the N -body model. Table 5.3 and table 5.4 summarise the timing parameters drawn from our experience with the Hydra (ARI) and JUMP (Jülich) parallel computers.

5.7 Block Size Distribution

The preceding section showed that the block size is closely related to the efficiency of the parallelisation. Small blocks are dominated by the latency and the parallelisation could be even slower than a single CPU calculation. Therefore we derive the block size distribution for the block time step scheme to assess its influence on the efficiency.

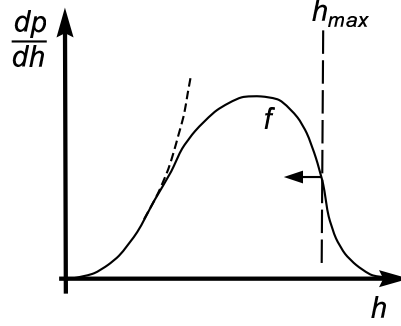


Figure 5.3: Timestep distribution $f = dp/dh$. The short-dashed line on the left indicates approximation Eq. 5.26, whereas the dashed line on the right defines a reasonable upper limit h_{\max} .

Suppose that the time steps⁴ h of all N particles in the model are distributed according to some known function f :

$$dp = f(N, h)dh \quad (5.25)$$

f is in most cases a complicated function. It involves spatial averaging and integration over the velocity distribution, which could be quite complicated even for simple time step formulas. Nevertheless there is a constraint on the time step distribution, simply because every particle has a neighbour within a finite distance: There is some upper limit h_{\max} , that restricts the major fraction of the time steps to a finite interval. Thus it is possible to capture the main features of the time step distribution with an expansion around $h = 0$ (Fig. 5.3 sketches this approximation):

$$f \approx C(N)h^a \quad h \leq h_{\max} \quad (5.26)$$

a is the lowest non-vanishing order of the expansion. Now we consider a block level with the largest possible time step h_k . The number of particles N_{bl} in this block is:

$$N_{\text{bl}} = N \int_0^{h_k} f dh \quad (5.27)$$

$$\approx \frac{C(N)}{a+1} (h_k)^{a+1} \quad (5.28)$$

According to the block time step scheme the number of blocks per time with the largest possible time step h_k is proportional to $(h_k)^{-1}$. Therefore the probability that a block size is in the range $[N_{\text{bl}}, N_{\text{bl}} + dN_{\text{bl}}]$ is

$$dp \propto \sum_k \delta \left(N_{\text{bl}} - \frac{C(N)}{a+1} h_k^{a+1} \right) \frac{1}{h_k} dN_{\text{bl}} \quad (5.29)$$

where δ is Dirac's delta function. The sum over the logarithmically equidistant time steps h_k is approximated by an integral:

$$dp \propto \int_0^\infty \delta \left(N_{\text{bl}} - \frac{C(N)}{a+1} h^{a+1} \right) \frac{d \ln(h)}{h} dN_{\text{bl}} \quad (5.30)$$

$$\approx \frac{1}{a+1} N_{\text{bl}}^{-(a+2)/(a+1)} dN_{\text{bl}} \quad (5.31)$$

⁴We use h instead of Δt in this section to avoid unclear notation.

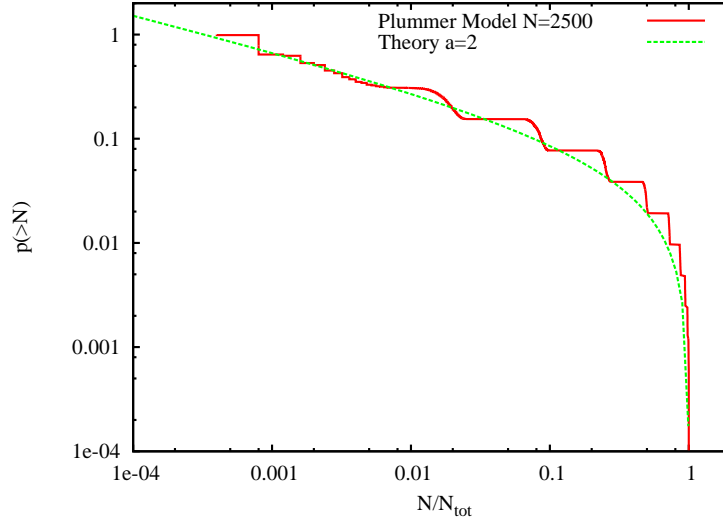


Figure 5.4: Cumulative irregular block size distribution for a $N = 2500$ particle plummer model.

Thus the average block size and the median of the block size distribution are:

$$\langle N_{\text{bl}} \rangle \approx \frac{1}{a} N^{a/(a+1)} \quad (5.32)$$

$$\text{median}(N_{\text{bl}}) \approx 2^{a+1} \quad (5.33)$$

Special expressions for the average block size were already derived by Makino and Hut 1988 [97], but the general relation of the time step distribution to the block size distribution is a new result. The median is surprisingly independent of the particle number, i. e. 50 % of all blocks are always smaller than a fixed value. It seems that this is a threat to the efficiency of the method, but the median of the wallclock time

$$\text{median}(N_{\text{bl}}^2) \approx \frac{N}{2^{(a+1)/a}} \quad (5.34)$$

demonstrates that these small blocks account only for a small fraction of the total CPU time. We confirmed the derived block size distribution (Eq. 5.31) by numerical calculations (see Fig. 5.4). The order parameter a is roughly two in (at least locally) homogenous systems, while an additional Keplerian potential reduces the order to $a = 1$. A planetesimal disc – or more precisely, a narrow ring of planetesimals – has a very narrow distribution of time steps since all particles share nearly the same orbital period. Thus the regular block size is always equal to the total particle number making the parallelisation very efficient.

5.8 Optimal Neighbour Number

We treated the mean neighbour number N_{nb} so far as some fixed value. But it is also a mean to optimise the speed of the integration. Large neighbour spheres reduce fluctuations in the regular forces allowing larger regular steps, which reduces the total number of force evaluations. But larger neighbour lists also imply a larger communication overhead, as all the neighbour lists have to be sent around to synchronise the different nodes. The best choice balances these two extremes, thus maximising the speed.

Before we derive the optimal neighbour number on a parallel machine, we briefly summarise the known solution for a single CPU run (see Makino and Hut 1988 [97] for an extensive derivation). The computational effort of the irregular steps is proportional to the neighbour number, while the

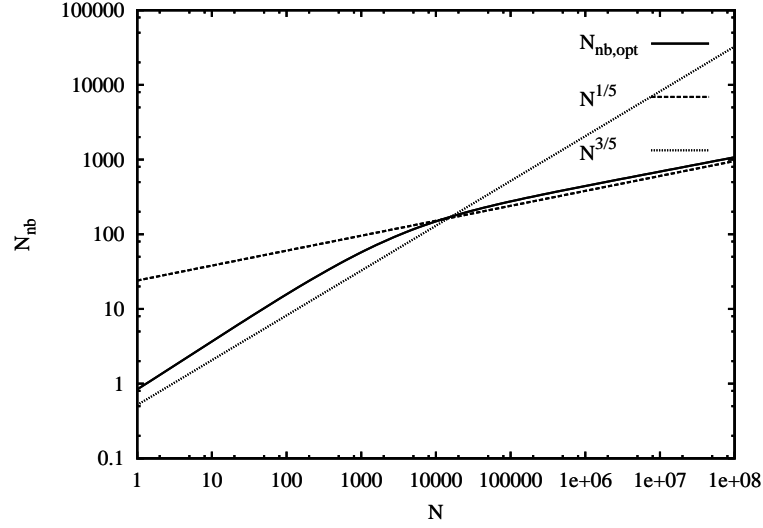


Figure 5.5: Optimal neighbour number as function of particle number N . The plot includes the numerical solution of Eq. 5.51 and the two asymptotic solutions. Timing constants are taken from Hydra.

number of force evaluations for the regular steps is proportional to the total number of particles, reduced by the time step ratio γ_t :

$$\gamma_t := \frac{\Delta t_{\text{reg}}}{\Delta t_{\text{irr}}} \quad (5.35)$$

$$T_{\text{CPU}} = f(N) \left(N_{\text{nb}} + \frac{N}{\gamma_t(N_{\text{nb}})} \right) \quad (5.36)$$

$$\gamma_t(N_{\text{nb}}) \approx N_{\text{nb}}^{1/3} \quad (5.37)$$

$f(N)$ collects all factors depending only on the total number of particles. Optimisation with respect to the neighbour number N_{nb} yields the well known result:

$$0 = \frac{d}{dN_{\text{nb}}} T_{\text{CPU}} \quad (5.38)$$

$$N_{\text{nb,opt}} \propto N^{3/4} \quad (5.39)$$

The calculation of the elapsed time for NBODY6++ on a PC cluster includes more terms. For clearness, we restrict ourselves to a rather simple model that involves only the dominant terms to show how parallelisation influences the optimal neighbour number. We make the following approximations:

- We only take the force calculation and communication into account.
- We use the same time constants for regular and irregular expressions.
- We neglect all numerical factors that are comparable to unity.

The total CPU time is an extension of Eq. 5.22, which is applied to the regular and the irregular step. A new constant B_n includes the neighbour list communication separately, while all factors

depending on N are represented by $f(N)$:

$$N_{\text{bl}} \approx N^{2/3} \quad (5.40)$$

$$\gamma_t \approx N_{\text{nb}}^{1/3} \quad (5.41)$$

$$T_{\text{irr}} = f(N) \left(\frac{N_{\text{bl}}N_{\text{nb}}}{p} + Ap + BN_{\text{bl}} \right) \quad (5.42)$$

$$T_{\text{reg}} = \frac{1}{\gamma_t} f(N) \left(\frac{N_{\text{bl}}N}{p} + Ap + (B + B_n N_{\text{nb}})N_{\text{bl}} \right) \quad (5.43)$$

$$T_{\text{tot}} = T_{\text{irr}} + T_{\text{reg}} \quad (5.44)$$

Optimisation with respect to the processor number p leads to:

$$0 = \frac{\partial}{\partial p} T_{\text{tot}} \quad (5.45)$$

$$p_{\text{opt}} = \sqrt{\frac{N^{2/3}N_{\text{nb}}^{4/3} + N^{5/3}}{A(N_{\text{nb}}^{1/3} + 1)}} \quad (5.46)$$

$$\approx \frac{N^{5/6}}{\sqrt{AN_{\text{nb}}^{1/6}}} \quad (5.47)$$

Further optimisation with respect to the neighbour number gives the expression:

$$0 = \frac{\partial}{\partial N_{\text{nb}}} T_{\text{tot}} \quad (5.48)$$

$$0 = N_{\text{nb}}^{4/3} - \frac{1}{3}N - \frac{1}{3}AN^{-2/3}p^2 - \frac{1}{3}Bp + \frac{2}{3}N_{\text{nb}}B_n p \quad (5.49)$$

For a fixed p or $B_n = 0$ (very fast neighbour list communication), we recover for large N :

$$N_{\text{nb,opt}} \propto N^{3/4} \quad (5.50)$$

In general, one can not neglect the neighbour list communication. Therefore we seek for the optimal choice of p and N_{nb} , thus combining Eq. 5.47 and Eq. 5.49:

$$AN_{\text{nb}}^{5/3} + \left(\frac{2}{3}N_{\text{nb}} - \frac{B}{3B_n} \right) B_n \sqrt{AN_{\text{nb}}^{1/6}} N^{5/6} = \frac{1}{3}(N_{\text{nb}}^{1/3} + 1)NA \quad (5.51)$$

Since this equation has no closed solution, we identify the dominant terms in Eq. 5.51 to calculate the asymptotic solution for large N :

$$N_{\text{nb,opt}} \approx \left(\frac{A}{4B_n^2} \right)^{3/5} N^{1/5} \quad N \gg \left(\frac{3A}{4B_n^2} \right)^{3/2} \quad (5.52)$$

For small N we get the approximated solution:

$$N_{\text{nb,opt}} \approx \left(\frac{N}{3} \right)^{3/5} \quad N < \left(\frac{3A}{4B_n^2} \right)^{3/2} \quad (5.53)$$

Fig. 5.5 compares the approximate expressions with the numerical solution of equation 5.51. In spite of the complicated structure of Eq. 5.51, both approximate expressions are reliable solutions. The example uses timing constants derived from our local PC cluster Hydra (ARI):

$$A \approx 200 \quad B \approx 5 \quad B_n \approx 0.5 \quad (5.54)$$

If we compare the new optimal neighbour number to the single CPU expression (Eq. 5.39), we find that the influence of the neighbour list communication favours much smaller neighbour numbers. N_{nb} increases so slowly with the particle number, that a neighbour number around 100 is a safe choice.

Chapter 6

Collisional Model

6.1 Introduction

The growth of planetesimals proceeds through collisions among planetesimals which form, at least in a sufficient fraction of incidents, larger bodies with a net gain of accreted matter. But some collisions are mere destructive events that shatter and disperse the colliding planetesimals. Small bodies are more susceptible to destruction, but they are also driven to high relative velocities due to the global energy equipartition making them even more vulnerable. A model that attempts to cover the full size range from one kilometre-sized to Mars-sized objects needs a realistic collision algorithm that covers both *fragmentation* and accretion.

Such a model was developed by Glaschke 2003 [43] and applied to asteroid families. The following section gives a general introduction to the theory of fragmentation and a concise overview of the main aspects of the fragmentation model.

6.2 Concepts

Two colliding bodies are equal in the sense that their intrinsic properties are not different. Only the comparison of two bodies defines the larger body – usually denoted as *target* – and the smaller one denoted as *projectile*. The two terms stem from laboratory experiments where they indicate much more than different sizes. A small projectile is shot on a target at rest to study the various parameters related to fragmentation. In the following, projectile and target only indicate the relative size of the two bodies.

The collision of two bodies initiates a sequence of complex phenomena. Shock waves run through the material, flaws start to grow rapidly breaking the bodies in many pieces apart. Some kinetic energy is transferred to the fragments, which leads to the ejection of fragments at different velocities in various directions. If the fragment cloud is massive enough, some of the larger fragments may capture debris. This post-collisional accretion is denoted as *reaccumulation*.

Although the depicted scenario is quite complex, there are a few measures that capture the most important aspects:

- Mass of the largest fragment M_L , or dimensionless $f_l = M_L/M$ where M is the combined mass of the two colliding bodies.
- $f_l < \frac{1}{2}$ refers to *fragmentation*, whereas $f_l > \frac{1}{2}$ is denoted as *cratering*.
- Energy per volume S that yields $f_l = \frac{1}{2}$ is denoted as *impact strength*.
- $f_{KE} := 2E_{kin}^{frag}/E_{kin}$: Fraction of the impact energy that is converted into kinetic energy of the fragments.

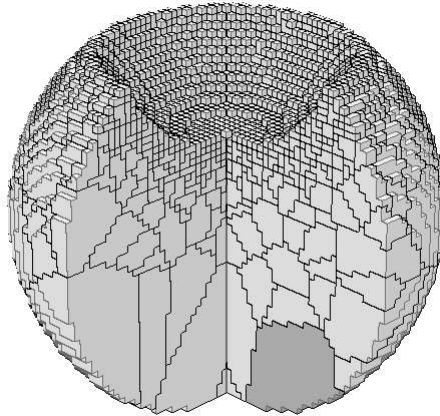


Figure 6.1: Section for $f_l = 0.04$ and $n = 3$. The largest fragment is coloured in dark-grey. In this calculation $60 \times 60 \times 60$ grid cells are used. Note the decomposition in grid cells and the Voronoi polyhedra which form the fragments.

Different fragment sizes and velocities are summarised by appropriate distribution functions. m_i , D_i and v_i are mass, diameter and modulus of the velocity of a given fragment, respectively.

1. Fragment size distribution:

- (a) $N_m(m)$: Number of all fragments with a mass $m_i \geq m$,
- (b) $M(m)$: Mass of all fragments with a mass $m_i \geq m$,
- (c) $N_D(D)$: Number of all fragments with a diameter $D_i \geq D$.

The distribution functions are related to each other:

$$\begin{aligned} N_m(m) &= N_D(D(m)) \\ M(m) &= \int_m^\infty x \left| \frac{dN_m(x)}{dx} \right| dx \\ N_m(m) &= \int_m^\infty \frac{1}{x} \left| \frac{dM(x)}{dx} \right| dx \end{aligned}$$

$D(m)$ is the size–mass relation.

2. Velocity distribution:

- (a) $\bar{v}(m)$: mean velocity as a function of mass.

6.3 Theory

Any theoretical or empirical prescription of a collision has to relate the afore mentioned parameters, namely the impact energy, to the sizes and velocities of the produced fragments. The central quantity is the impact strength, which is a measure for the overall stability of a body. Objects smaller than 1 metre are accessible to laboratory experiments, while collisions of larger bodies up to asteroid size have to be analysed by complex computer simulations. Asteroid families, which

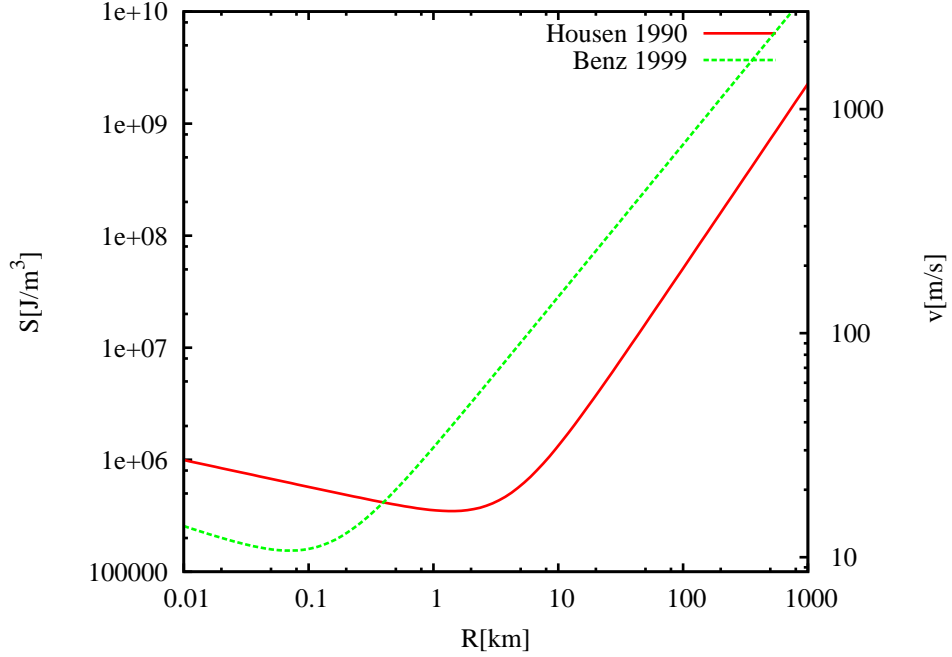


Figure 6.2: Impact strength according to Eq. 6.1 and Eq. 6.3. The right axis gives the corresponding impact velocity according to $S = 1/2\rho v^2$ with $\rho = 2.7 \text{ g/cm}^3$.

are remnants of giant collisions in the asteroid belt, provide independent insight, although the data is difficult to interpret.

We selected two different impact strength models as reference for our work. The first was obtained by Housen and Holsapple 1990 [58] through the combination of asteroid family data and laboratory experiments via scaling laws:

$$S = S_0 \left(\frac{R}{1 \text{ m}} \right)^{-0.24} \left(1 + 1.6612 \times 10^{-7} \left(\frac{R}{1 \text{ m}} \right)^{1.89} \right) \quad f_{\text{KE}} = 0.1 \quad (6.1)$$

$$S_0 = 1.726 \times 10^6 \text{ Jm}^{-3} = 1.726 \times 10^7 \text{ erg cm}^{-3} \quad (6.2)$$

A more recent result was obtained by Benz and Asphaug 1999 [17] through SPH simulations (for basalt, $v = 3 \text{ km/s}$):

$$S = S_0 \left(\frac{R}{1 \text{ m}} \right)^{-0.38} \left(1 + 6.989 \times 10^{-5} \left(\frac{R}{1 \text{ m}} \right)^{1.74} \right) \quad f_{\text{KE}} \approx 0.01 \quad (6.3)$$

$$S_0 = 6.082 \times 10^5 \text{ Jm}^{-3} \quad (6.4)$$

$$\rho = 2.7 \frac{\text{g}}{\text{cm}^3} \quad (6.5)$$

f_{KE} is a measure of the kinetic energy that is transferred to the fragments:

$$E_{\text{kin}}^{\text{frag}} = \frac{f_{\text{KE}}}{2} E_{\text{kin}} \quad (6.6)$$

We introduce a dimensionless measure γ of the relative importance of gravity for the result of a collision. It is defined as the ratio of the energy per volume S_G that is necessary to disperse the

Largest Fragment

γf_l^i	0.1	0.2	0.3	0.4	0.5	0.6	0.7	0.8
0.02552	0.10000	0.20000	0.30000	0.40000	0.50000	0.60000	0.70000	0.80000
0.19897	0.10000	0.20000	0.30000	0.40000	0.50000	0.60000	0.70000	0.80000
0.67985	0.10000	0.20000	0.30000	0.40000	0.57612	0.67315	0.82006	0.96073
1.14050	0.10000	0.31526	0.35708	0.61362	0.83511	0.92832	0.94380	0.97572
1.77057	0.10884	0.58883	0.75974	0.87922	0.92755	0.93662	0.97107	0.97924
2.26021	0.15895	0.68891	0.87217	0.89592	0.92965	0.96089	0.96701	0.98727
3.11626	0.30954	0.83774	0.90272	0.92682	0.95943	0.95565	0.97677	0.98791

Second largest Fragment

γf_l^i	0.1	0.2	0.3	0.4	0.5	0.6	0.7	0.8
0.02552	0.08171	0.10770	0.06471	0.08107	0.04976	0.03982	0.03171	0.02155
0.19897	0.09174	0.09533	0.08410	0.06967	0.04930	0.04825	0.03510	0.02077
0.67985	0.07713	0.08365	0.07791	0.08387	0.07026	0.06147	0.06082	0.00847
1.14050	0.08621	0.07256	0.10331	0.09640	0.02467	0.00675	0.00783	0.00265
1.77057	0.07909	0.05549	0.06961	0.02035	0.00329	0.00719	0.00273	0.00161
2.26021	0.06693	0.02288	0.00528	0.00882	0.00584	0.00268	0.00664	0.00126
3.11626	0.06940	0.00884	0.00384	0.00488	0.00064	0.01007	0.00225	0.00162

Table 6.1: Data compilation of the fragmentation calculations.

fragments to the impact strength S_0 :

$$S_G = 2\pi \frac{4 - 2\sqrt[3]{2}}{5f_{\text{KE}}} GR^2 \rho^2 \quad (6.7)$$

$$\gamma := S_G/S \quad (6.8)$$

The first step towards the prediction of a collisional outcome is to relate the impact energy and the impact strength to ascertain the size of the largest fragment f_l . Laboratory experiments and simulations indicate the functional form

$$\epsilon(f_l) = \begin{cases} 2(1 - f_l) & \text{for } f_l > \frac{1}{2} \\ (2f_l)^{-\frac{1}{K}} & \text{otherwise.} \end{cases} \quad (6.9)$$

$$\epsilon = \frac{E_{\text{kin}} \rho}{2SM} \quad (6.10)$$

which is both valid in the fragmentation regime and the cratering limit. The size of the largest fragment is used to derive the full size distribution. To accomplish the decomposition ‘seed fragments’ are distributed inside the target according to the largest desired fragment. The full set of fragment is derived from a *Voronoi tessellation*¹ using these seed points. Fig. 6.1 depicts the result of such a decomposition. The fragment velocities are calculated from the total kinetic energy after the collision to initiate a post-collisional N -body calculation to treat reaccumulation.

We conducted a large set of such calculations to cover a sufficient range in f_l^i (i. e. impact energy) and γ (i. e. body size). Table 6.1 summarises the derived values of the largest and second largest fragment including reaccumulation.

¹The Voronoi tessellation assigns every volume element to the closest seed point. First applications date back to the 17th century, but Georgy Fedosevich Voronoy putted it on a general base in 1908.

Chapter 7

Collisional Cascades

7.1 Introduction

A first well-defined application of the fragmentation model is a *collisional cascade*. The term *cascade* denotes that fragments of one collision in a many-body system may hit other bodies, whose fragments further shatter even more bodies. Thus the particle number increases exponentially with every subsequent collision.

Although the formation of planets requires a net growth due to collisions, this destructive process plays a role in the formation of larger bodies as the overall size distribution controls the accretion rate of the protoplanets. Therefore it is worth to have a closer look on this mechanism to have a well founded theory at hand, which provides deeper understanding and a safe ground that supports numerical calculations.

7.2 Self-similar Collisions

A system of colliding bodies is usually embedded in a broader context, like stars moving in a galaxy or asteroids orbiting in our own solar system. First, we simplify this dynamical background as well as some aspects of the collisions to make the problem tractable.

The first step is to decompose an inhomogeneous system into smaller subvolumes which are locally homogenous. Furthermore, it is assumed that these subvolumes hardly interact with each other. Hence it is possible to apply the *particle-in-a-box-method* (Safronov 1969 [130]) to analyse collisions within the small subvolumes:

- All particles are contained in a constant volume.
- The particle sizes are described by a distribution function $n(m)$, i. e. the particle number per volume and mass interval.
- For convenience, we assume a constant (or typical) relative velocity for a given pair of colliding bodies.

The distribution function is evolved by the *coagulation equation*. We modified the equation given by Tanaka et al. 1996b [141] by introducing a new function M_{red} to arrive at a more concise expression:

$$0 = \frac{\partial}{\partial t} mn(t, m) + \frac{\partial}{\partial m} F_m(t, m) \quad (7.1)$$

The mass flux F_m is given by:

$$F_m = - \iint n(t, m_1)n(t, m_2) \underbrace{\sigma(m_1, m_2)v_{\text{rel}}M_{\text{red}}(m, m_1, m_2)}_{\text{Coagulation Kernel}} dm_1 dm_2 \quad (7.2)$$

$$M_{\text{tot}} = \int n(t, m)mdm \quad (7.3)$$

$$\frac{\partial}{\partial t}M_{\text{tot}} = F_m(m_{\text{min}}) \quad (7.4)$$

n is the already introduced size distribution, v_{rel} is the mean relative velocity, σ is the cross section for colliding bodies (m_1, m_2) and M_{red} is the newly introduced *fragment redistribution function*. M_{red} contains all information on the fragments arising from the breakup of body m_1 due to the impact of body m_2 . Its definition avoids double counting of collisions in the above integral. The redistribution function is related to the differential number distribution function $n_{\text{coll}}(m_1, m_2, m)$, i. e. the number of fragments produced by a collision per mass interval. Since the target m_1 formally disappears, it is included as a negative contribution:

$$M_{\text{red}}(m, m_1, m_2) := \int_0^m (n_{\text{coll}}(m_1, m_2, \tilde{m}) - \delta(\tilde{m} - m_1))\tilde{m}d\tilde{m} \quad (7.5)$$

Mass conservation in each collision is reflected by $M_{\text{red}}(0, m_1, m_2) = M_{\text{red}}(\infty, m_1, m_2) = 0$. The cross section σ depends on the velocities and radii R_i of the particles. A simple approach is the *geometric cross section*:

$$\sigma(m_1, m_2) = \pi(R_1 + R_2)^2 \quad (7.6)$$

If gravity plays an important role during encounters, two colliding bodies move on hyperbolic orbits with a pericentre distance that is smaller than the impact parameter. This leads to an additional enlargement of the cross section, denoted as *gravitational focusing*:

$$\sigma(m_1, m_2) = \pi(R_1 + R_2)^2 \left(1 + \frac{2G(m_1 + m_2)}{v_{\text{rel}}^2(R_1 + R_2)} \right) \quad (7.7)$$

A special class of collisional models are self-similar collisions. Self-similarity implies an invariance of the collisional outcome with respect to the scale of the colliding bodies. If the target mass as well as the projectile mass are enlarged by a factor of two, then only the masses of all fragments doubles without further changes in the collisional outcome. They allow the convenient introduction of a dimensionless fragment redistribution function f_m :

$$M_{\text{red}}(m, m_1, m_2) = mf_m(m_1/m, m_2/m) \quad (7.8)$$

We follow Tanaka et al. 1996b [141] and employ the substitution¹ $m_1 = mx_1$, $m_2 = mx_2$ to simplify Eq. 7.2:

$$F_m = - \iint n(t, mx_1)n(t, mx_2)m^{11/3}\sigma(x_1, x_2)v_{\text{rel}}f_m(x_1, x_2)dx_1dx_2 \quad (7.9)$$

A simple solution is a steady-state cascade with $F_m = \text{const}$. The loss of bodies of a given size is balanced by the fragment supply from larger bodies, hence the system maintains a steady-state $\frac{\partial}{\partial t}n(t, m) = 0$. Eq. 7.9 inspires the ansatz $n(m) \propto m^{-k}$, which yields $k = 11/6$. This is the well known equilibrium slope in self-similar collisional cascades, which was already found by Dohnanyi 1969 [39]. Strong gravitational focusing changes the exponent² to $k = 13/6$. Both steady-state

¹A similar approach to the solution of the coagulation equation is the Zakharov transformation, see Connaughton et al. 2004 [36].

²Tanaka et al. 1996b [141] state that $k < 2$ is a necessary condition for a finite mass flux. However, their analysis is not valid for all possible collisional models.

solutions seem to be rather artificial, as they contain an infinite amount of mass and require a steady mass influx from infinity. However, they provide an appropriate description for the relaxed fragment tail of a size distribution, as long as the largest bodies provide a sufficient flux of new fragments. Once the largest bodies start to decay, the finite amount of mass in the system leads to an overall decay of the collisional cascade. Thus we seek for a more general solution to Eq. 7.1 using the ansatz $n(t, m) = a(t)n_0(m)$:

$$\frac{\partial}{\partial t}a(t) = -Ca(t)^2 \quad (7.10)$$

$$mn_0(m) = \frac{1}{C} \frac{\partial}{\partial m} F_m \quad (7.11)$$

C is determined by fixing n_0 at an arbitrary value m^* . $a(t)$ is independent of the collision model:

$$a(t) = \frac{1}{1 + Ct} \quad (7.12)$$

$$C \propto n(m^*) \quad (7.13)$$

A power law solution is $n_0(m) \propto -Cm^{-k+1}$ which is only valid for $C < 0$ (agglomeration dominates). To examine $C > 0$, we perturb the already known equilibrium solution:

$$n_0(m) = N_0m^{-k} - CN_1m^{-2k+2} + \mathcal{O}(C^2) \quad (7.14)$$

$$\frac{1}{N_1} = (2 - k) \iint x_1^{-k} x_2^{-2k+2} \sigma(x_1, x_2) v_{\text{rel}} (f_m(x_1, x_2) + f_m(x_2, x_1)) dx_1 dx_2 \quad (7.15)$$

N_1 is small if the integral on the right hand side is large. This is the case for a sufficiently large impact strength. Eq. 7.14 has the interesting property that $n(m') = 0$ for some mass m' , given that $k < 2$. This mass m' represents the largest body in the system, e. g. the largest asteroid in a fictitious asteroid belt.

7.3 Size-dependent Strength

Self-similarity is an enormous help in analysing the coagulation equation. It releases completely the need to know any specific details of the collisional process and provides valuable insight at the same time. But self-similarity is also a strong limitation on the underlying collisional physics.

A major component of a fragmentation model is the knowledge of the impact strength as a function of size. Simulations as well as asteroid families establish that it is not some fixed value, but changes with size which immediately breaks the self-similarity. Larger bodies are weaker due to an increasing number of flaws (there are no big monocrystals), but then gravity leads to a turnover and increases the strength.

We model the size dependent strength S with a power law to examine the influence on the equilibrium solution. The velocity dispersion v and the collisional cross section σ are also modelled with power laws to account for relaxation processes:

$$v = v_0 \left(\frac{m}{m_0} \right)^w \quad (7.16)$$

$$\sigma = \sigma_0 \left(\frac{m}{m_0} \right)^s \quad (7.17)$$

$$S = S_0 \left(\frac{m}{m_0} \right)^\alpha \quad (7.18)$$

The subscript '0' denotes values for an arbitrarily chosen scaling mass. Since smaller bodies are more abundant than larger ones, we safely assume that most collisions involve a large mass ratio.

In addition, we assume $w < 0$, since we expect energy equipartition to some degree in most cases. These restrictions lead to the following simplifications ($m_1 > m_2$):

$$\sigma(m_1, m_2) \approx \sigma(m_1) \quad (7.19)$$

$$v_{\text{rel}} \approx v(m_2) \quad (7.20)$$

$$\epsilon \approx \frac{1}{2} \frac{m_2 \rho v_{\text{rel}}^2}{m_1 S_1} \quad (7.21)$$

Therefore the smaller body m_2 enters only through the specific energy ϵ :

$$F_m \approx - \iint n(t, m_1) n(t, m_2) \sigma(m_1) v_{\text{rel}}(m_2) m_1 f_m(m_1/m, \epsilon) dm_1 dm_2 \quad (7.22)$$

We introduce new dimensionless quantities with the help of Eq. 7.19–7.21 to simplify the integral:

$$m_1 = m x_1 \quad (7.23)$$

$$m_2 = m_0 \left(\frac{m_1}{m_0} \right)^{\frac{1+\alpha}{1+2w}} \left(\frac{2S_0}{\rho v_0^2} \right)^{\frac{1}{1+2w}} \epsilon^{\frac{1}{1+2w}} \quad (7.24)$$

Again we assume a power law for the density $n \propto m^{-k}$ and change the integration parameters to (x_1, ϵ) . Applying the constant-flux condition yields the equilibrium exponent

$$k \approx \frac{s + 3 + \alpha + w(2s + \alpha + 5)}{2 + \alpha + 2w} \quad (7.25)$$

and the scaling exponent k' of the total mass loss:

$$k' \approx \frac{s - w + 1}{2 + \alpha + 2w} \quad (7.26)$$

$$\frac{\partial}{\partial t} M_{\text{tot}} \propto -\tilde{S}^{-k'} \quad \tilde{S} = \frac{2S_0}{\rho v_0^2} \quad (7.27)$$

The exponent k' in Eq. 7.27 is close to unity for realistic values of the free parameters. Thus the mass loss is roughly anti-proportional to the strength of the bodies. The general formula Eq. 7.25 contains the special solution of Brien and Greenberg 2003 [110], who concentrated on the parameters $s = 2/3$, $w = 0$ and a special collisional model. In fact, the derivation applies to a much wider class of collisional models, that we denote as *scalable collisional models*. Scalable indicates that the model is self-similar except a scaling of the impactor mass.

7.4 Perturbation of Equilibrium

The derived scaling relations provide insight into the overall properties of a collisional cascade, which is in (or close to) equilibrium. However, they do not provide information on how the equilibrium is attained or how the system responds to various external perturbations. A rigorous approach would be the approximate solution of the coagulation equation³, which is by no means simple since it requires a careful analysis of the collision model.

Hence we turn to perturbations of the equilibrium size distribution, as it is easier to assess the quality of the derived expression for a variety of collision models. In addition, all equations are linear in the perturbation, allowing the detailed analysis of the solution.

If the equilibrium solution $n(m) = n_0(m/m_0)^{-k}$ is perturbed with a small deviation $\Delta n(m)$, we get to first order:

$$0 = \frac{\partial}{\partial t} m \Delta n(m) + \frac{\partial}{\partial m} F_p(t, m) \quad (7.28)$$

$$F_p = - \iint \Delta n(m_1) n(t, m_2) \sigma(m_1, m_2) v_{\text{rel}} \times (M_{\text{red}}(m, m_1, m_2) + M_{\text{red}}(m, m_2, m_1)) dm_1 dm_2 \quad (7.29)$$

³Appendix E highlights a possible approach.

Despite of the expansion in Δn , Eq. 7.28 is still a complicated *integro-differential equation*. Thus it is not possible to obtain a solution without further information about the problem. While there is no general solution, we restrict our attention to self-similar collisional processes. In virtue of this assumption it is possible to simplify Eq. 7.28:

$$0 = \frac{\partial}{\partial t} m \Delta n(m) - n_0 m_0^3 \sigma_0 v_0 \frac{\partial}{\partial m} \int \Delta n(t, m x_1) F(x_1) (m x_1 / m_0)^k dx_1 \quad (7.30)$$

$$F(x_1) = \int m_0^{2k-3} x_1^{-k} x_2^{-k} \frac{\sigma(x_1, x_2) v_{\text{rel}}}{\sigma_0 v_0} (f_m(x_1, x_2) + f_m(x_2, x_1)) dx_2 \quad (7.31)$$

σ_0 and v_0 are velocity and cross section of an arbitrarily chosen scaling mass m_0 . $F(x_1)$ contains all information about the collisional process. If collisions do not result in extreme outcomes, like cratering or a complete destruction of the target, most of the fragment mass is contained in bodies with similar size as the parent body. Hence we expect that $F(x_1)$ peaks around $x_1 \approx 1$ and drops to zero as x_1 gets larger (or smaller). We introduce the dimensionless relative perturbation $g(m)$:

$$g(m) = \frac{\Delta n(m)}{n(m)} \quad (7.32)$$

$$= \frac{\Delta n(m) m^k}{n_0 m_0^k} \quad (7.33)$$

Thus the new differential equation reads:

$$0 = \frac{\partial}{\partial t} (m/m_0)^{1-k} \Delta g(m) - n_0 m_0^2 \sigma_0 v_0 \frac{\partial}{\partial m} \int \Delta g(t, m x_1) F(x_1) dx_1 \quad (7.34)$$

We change to logarithmic coordinates to arrive at a convolution integral:

$$u = \ln(m/m_0) \quad u_1 = \ln(x_1) \quad (7.35)$$

Furthermore we define a collisional timescale τ_0

$$\tau_0 = (n_0 m_0 \sigma_0 v_0)^{-1} \quad (7.36)$$

to obtain a more concise expression. The transformed equation is:

$$0 = \frac{\partial}{\partial t} g(t, u) e^{u(2-k)} - \frac{1}{\tau_0} \frac{\partial}{\partial u} \int g(t, u + u_1) G(u_1) du_1 \quad (7.37)$$

$$G(u) = F(e^u) e^u \quad (7.38)$$

If $g(u)$ is varying on a scale larger than the width of the kernel $G(u)$ (compare Fig. 7.1), it is justified to expand $g(u)$ under the integral. We retain the first two moments of $G(u)$:

$$0 = \frac{\partial}{\partial t} g(t, u) e^{u(2-k)} - \frac{G_0}{\tau_0} \frac{\partial}{\partial u} g(t, u) - \frac{G_1}{\tau_0} \frac{\partial^2}{\partial u^2} g(t, u) \quad (7.39)$$

$$G_k = \int u^k G(u) du \quad (7.40)$$

The first order moment G_1 , which introduces a diffusive term, is omitted in the following for clarity⁴. We introduce a fragmentation time $\tau_{\text{frag}}(u)$ and transform Eq. 7.39 back to m :

$$0 = \frac{\partial}{\partial t} g(t, m) - \frac{m}{\tau_{\text{frag}}(m)} \frac{\partial}{\partial m} g(t, m) \quad (7.41)$$

$$\tau_{\text{frag}} = \frac{\tau_0}{G_0} e^{u(2-k)} \quad (7.42)$$

$$= \frac{\tau_0}{G_0} (m/m_0)^{2-k} \quad (7.43)$$

⁴The study of wave-like structures in the size distribution (see e.g. Bagatin et al. 1994 [10]) requires even the second order moment G_2 .

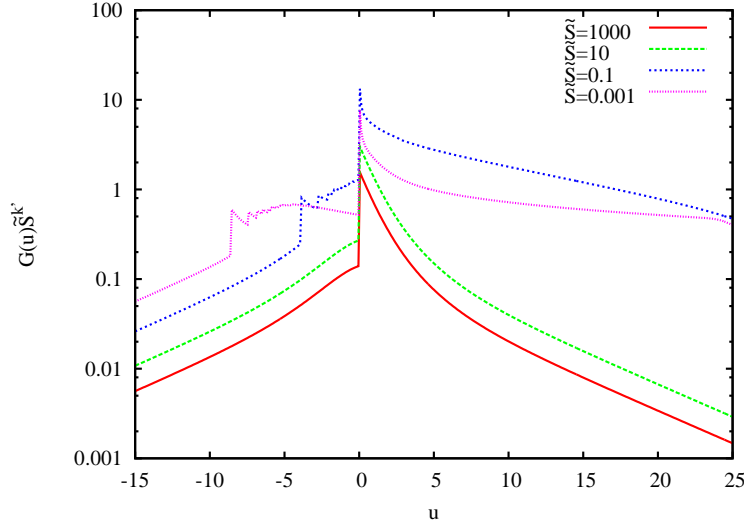


Figure 7.1: Scaled fragmentation kernel $G(u)$ for a simple fragmentation model (see Eq. 7.74) and different scaled impact strength \tilde{S} .

Eq. 7.41 is a modified *advection equation*, which conserves the total mass. It is possible to derive equations similar to Eq. 7.41 for any collisional model. However, the general approach is less fruitful, as it lacks a robust frame of a known equilibrium solution and reliable scaling relations. Therefore we provide only the extension to scalable collisional models in Appendix D. We readily obtain the general solution:

$$g(t, m) = f\left(t + \tau_0 \frac{(m/m_0)^{(2-k)}}{G_0(2-k)}\right) \quad (7.44)$$

$$\Delta n(t, m) = n(m) f\left(t + \tau_0 \frac{(m/m_0)^{(2-k)}}{G_0(2-k)}\right) \quad (7.45)$$

The function f is determined by the initial value $g(0, m)$ of the perturbation. As the collisional cascade evolves, the initial perturbation function is shifted as a whole to smaller masses. This evolution becomes more clearer if we attach labels $M(0)$ to the initial perturbation function and follow the time evolution of these tags. The functions $M(t)$ are the *characteristics*⁵ of the differential equation 7.41:

$$M(t) = m_0 \left((M(0)/m_0)^{(2-k)} - t/\tau_0 G_0(2-k) \right)^{1/(2-k)} \quad (7.46)$$

The meaning of the fragmentation time τ_{frag} becomes clear by the relation

$$\frac{M}{\dot{M}} = -\tau_{\text{frag}} \quad (7.47)$$

which is the time until a body has lost a significant fraction of its mass due to destructive collisions. A comparison of the perturbation equation 7.41 with the scaling relations from the previous section gives the scaling of the zeroth order moment G_0 with respect to the impact strength:

$$G_0 = G'_0 \tilde{S}^{-k'} \quad (7.48)$$

G'_0 should only depend on the fragmentation model (i.e. fragment size distribution as a function of the largest fragment f_l) within the limits of this approximation. Fig. 7.1 shows that the scaling

⁵In general, characteristics of a partial differential equation are paths along which the solution is constant.

with the impact strength works quite well, except slight variations which are small compared to the covered range of impact strengths. Likewise, it is possible to restate the total equilibrium flux F_{eq} in terms of G'_0 :

$$F_{\text{eq}}(m) \approx -\frac{G'_0}{2} n(m)^2 \sigma(m) m^3 v_{\text{rel}} \tilde{S}^{-k'} \quad (7.49)$$

The fragmentation timescale $\tau_{\text{frag}}(m)$ allows a more intuitive expression:

$$F_{\text{eq}}(m) \approx -\frac{1}{2} \frac{n(m)m^2}{\tau_{\text{frag}}(m)} \quad (7.50)$$

Our simple collisional model (see Fig. 7.1 and Eq. 7.74) refers to:

$$F_{\text{eq}}(m) = -(1 \dots 30) \times n(m)^2 \sigma(m) m^3 v_{\text{rel}} \tilde{S}^{-k'} \quad (7.51)$$

7.5 Migration and Collisions

The local perturbation analysis is only applicable to a planetesimal disc, if the migration velocity of the planetesimals is negligible small. This assures that collisional cascades at different radial distances do not couple to each other, so that the whole disc is composed of many local cascades. While this assumption is justified for larger bodies, migration is strongly influencing bodies below 1 km in size. Hence we extend our analysis to examine the influence of migration on the (no longer) local collisional processes.

We assume that the collisional evolution of the system leads to an equilibrium planetesimal distribution everywhere in the disc:

$$\Sigma_0(r, m) = \Sigma_{r,0}(r) C_0(m) \quad (7.52)$$

$\Sigma_r(r)$ is the total surface density at a given distance r , while $C_0(m)$ is the universal equilibrium distribution. Though the planetesimal distribution at larger sizes is likely different at different locations in the disc, we only demand a universal function at smaller sizes, where migration is important. The power law exponent k depends on the details of the invoked physics, but numerical simulations show that $k \approx 2$ is a fiducial value. Eq. 7.52 does not yet include migration effects. If we include migration, the surface density is modified to

$$\Sigma(r, m) = g(r, m) \Sigma_0(r, m) \quad (7.53)$$

where the dimensionless function g contains the changes due to migration. The collisional evolution is governed by the continuity equation with an additional collisional term

$$\frac{\partial \Sigma(r, m)}{\partial t} - \frac{1}{r} \frac{\partial}{\partial r} (v(r, m) r \Sigma(r, m)) = \dot{\Sigma}_{\text{coll}} \quad (7.54)$$

where $v(r, m)$ is the migration velocity (see Eq. 4.39), defined such that positive v imply an inward migration. We express the collisional term with the help of Eq. 7.41 and seek for a steady-state solution $\dot{\Sigma} = 0$:

$$\frac{1}{\tau_{\text{frag}}(m, r)} \frac{\partial g}{\partial m} m \Sigma_{r,0}(r) + \frac{1}{r} \frac{\partial}{\partial r} (g v r \Sigma_{r,0}(r)) = 0 \quad (7.55)$$

$\tau_{\text{frag}}(m, r)$ is the fragmentation timescale of a mass m at a distance r . Since the surface density Σ and the various contributions to the drag force are well described by a power law (with respect to radius), Eq. 7.55 further simplifies to:

$$\frac{1}{\tau_{\text{frag}}(m, r)} \frac{\partial g}{\partial m} m + \frac{\partial g}{\partial r} v - \frac{b}{r} g v = 0 \quad (7.56)$$

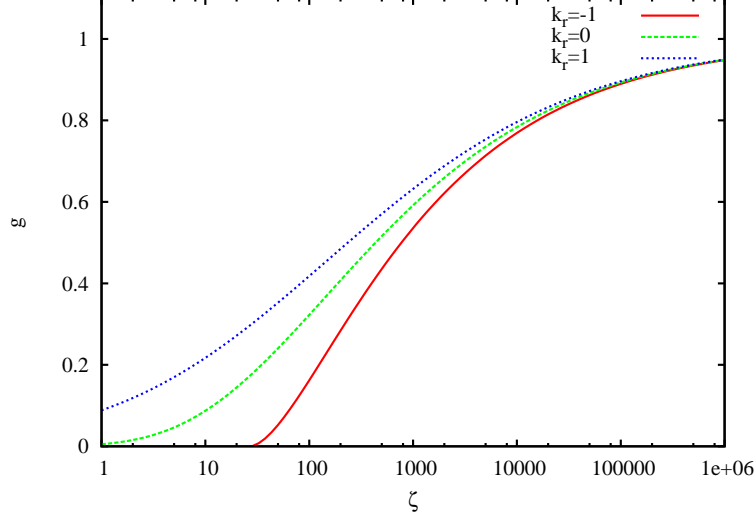


Figure 7.2: Cut-off function g according to Eq. 7.64. The mass exponent is $k_m = 1/3$, while the mass influx exponent is $b = 1.75$ according to the minimum solar nebula.

b is a combination of the various invoked power law exponents. As the surface density Σ and the gas density drop with increasing radius in any realistic disc model, it is safe to assume $b > 0$. We choose a self-similar ansatz for g :

$$g(r, m) = g(\zeta) \quad , \quad \zeta = mg_m(r) \quad (7.57)$$

The new differential equation is

$$\frac{1}{\tau_{\text{frag}}(m, r)} \frac{dg}{d\zeta} mg_m(r) + m \frac{dg}{d\zeta} \frac{dg_m}{dr} v - \frac{b}{r} gv = 0 \quad (7.58)$$

which is equivalent to the more concise expression:

$$\frac{d \ln(g)}{d \ln(\zeta)} \left(\frac{r}{v\tau_{\text{frag}}} + \frac{d \ln(g_m)}{d \ln(r)} \right) = b \quad (7.59)$$

We assume a power-law dependence for the timescale ratio $\tau_{\text{mig}}/\tau_{\text{frag}}$:

$$\frac{r}{v\tau_{\text{frag}}} = \frac{\tau_{\text{mig}}}{\tau_{\text{frag}}} \quad (7.60)$$

$$= (m/m_0)^{k_m} (r/r_0)^{k_r} \quad (7.61)$$

The cut-off mass m_0 at a distance r_0 has a timescale ratio $\tau_{\text{mig}}/\tau_{\text{frag}} = 1$, which defines a proper lower cut-off within this context. Hence the solution is:

$$b = \frac{d \ln(g)}{d \ln(\zeta)} \left(\zeta^{k_m} + \frac{k_r}{k_m} \right) \quad (7.62)$$

$$g_m(r) = \frac{(r/r_0)^{k_r/k_m}}{m_0} \quad (7.63)$$

$$g(\zeta) = \left(1 + \frac{k_r}{k_m \zeta^{k_m}} \right)^{-b/k_r} \quad (7.64)$$

Though the analytical solution Eq. 7.64 provides a complete description of the lower cut-off of the size distribution, it is more appropriate within the frame of this discussion to translate the

equilibrium solution to an equilibrium mass loss due to migration:

$$\dot{\Sigma}_{\text{mig}}(r, m) = -\frac{bv}{r}\Sigma + \frac{bv}{r}\Sigma \frac{k_r/k_m}{\zeta^{k_m} + k_r/k_m} \quad (7.65)$$

$$= -\frac{b\Sigma}{\tau_{\text{mig}} + k_r/k_m \tau_{\text{frag}}} \quad (7.66)$$

An inspection of the timescale ratio shows that the mass exponent k_m should be positive, whereas simple estimations of k_r on the basis of the minimum mass solar nebula are somewhat inconclusive. The value of k_r is so close to zero, that any change in the assumed equilibrium slope or the impact strength scaling gives easily both positive and negative values. Moreover, Eq. 7.66 requires a globally relaxed planetesimal disc, but the huge spread in the various involved timescales at different radii inhibits any significant relaxation in the early stages.

However, it is possible to gain valuable information from the two limiting cases $k_r > 0$ and $k_r < 0$. Both values of k_r give the proper limit $g \rightarrow 1$ at large masses, where the migration timescale is much larger than the fragmentation timescale and we recover the steady-state collisional cascade.

A positive exponent k_r reduces the effective mass loss due to migration, as fragments from the outer part of the disc replenish the local mass loss. Hence the fragmentation timescale controls the net loss of smaller planetesimals. In contrast, a negative exponent k_r leads to a pronounced cut-off in the size distribution, since only larger planetesimals are replenished through inward migration. Though the mass loss rate is singular at some mass m' , this sharp cut-off is an artifact due to the perturbation approximation.

Our analysis is subjected to several restrictions. We applied the perturbation equation to values of g , that exceed the limit for a safe application (i. e. $g \approx 1$) of the perturbation expansion. Furthermore, the steady-state solution requires a global relaxation of the collisional processes, which is practically never obtained during the disc evolution. Despite of these restrictions, we gained insight on a more qualitative level. Numerical calculations indicate, that the perturbation approximation is inappropriate close to the lower cut-off of the size distribution. However, a comparison of different exponents k_r (see Fig. 7.2) attributes only a minor role to the replenishment of fragments due to inward migration. Only unrealistic small slopes b of the migrational mass influx would strengthen the importance of this process. Though temporally non-equilibrium phenomena are not ruled out by the previous derivation, their study would require the global simulation of the system.

7.6 Coagulation

While most coagulation kernels are only restricted to a limited analytical analysis (e. g. scaling relations), there exist some special kernels that allow the closed solution of the coagulation equation. All rely on the assumption of perfect mergers, which allows the reformulation of the general equation 7.1 to

$$\begin{aligned} \frac{\partial n(m, t)}{\partial t} &= \frac{1}{2} \int_0^m \mathcal{K}(m - m', m') n(m - m', t) n(m', t) dm' \\ &\quad - n(m, t) \int_0^\infty \mathcal{K}(m, m') n(m', t) dm' \end{aligned} \quad (7.67)$$

where \mathcal{K} is the coagulation kernel. One of these particular kernels was introduced by Safronov 1969 [130]:

$$\mathcal{K}(m_1, m_2) = A_1(m_1 + m_2) \quad (7.68)$$

This coagulation kernel implies perfect mergers, where the coalescence rate of two particles m_1 and m_2 is assumed to be proportional to the sum of their masses. It seems that this is an artificial choice, devised to allow an analytic solution. However, the Safronov cross section provides an

ρ	2,700 kg/m ³
k	1/6
Model	Gaussian Scatter
f_{KE}	0.1
K	1.24

Table 7.1: Main parameters of the collisional model.

intermediate case between a geometric cross section ($\sigma \propto m^{2/3}$) and strong gravitational focusing ($\sigma \propto m^{4/3}$). A special solution to the initial condition

$$n(m, 0) = \frac{n_0}{m_0} \exp(-m/m_0) \quad (7.69)$$

is the function (see e. g. Ohtsuki et al. 1990 [113])

$$n(m, \tau) = \frac{n_0 \tilde{g}}{m \sqrt{1 - \tilde{g}}} \exp(-(2 - \tilde{g})m/m_0) I_1(2m/m_0 \sqrt{1 - \tilde{g}}) \quad (7.70)$$

$$\tilde{g} = \exp(-\tau) \quad \tau = A_1 \rho t \quad (7.71)$$

$$\rho = \int_0^\infty mn(m) dm = n_0 m_0 \quad (7.72)$$

where τ is the dimensionless time and I_1 is a modified Bessel function of the first kind.

7.7 Models for M_{red}

Though we already obtained insight into the nature of collisional cascades without a detailed specification of the coagulation kernel, any detailed study of a collisional system requires the specification of a realistic collisional model.

First, we restate the well-known perfect accretion model. While it is a gross oversimplification for collisions among kilometre-sized planetesimals, its simplicity allows a reliable code testing and eases the comparison with other works:

$$M_{\text{red}}(m, m_1, m_2) = -m_1 \Theta(m - m_1) - m_2 \Theta(m - m_2) + (m_1 + m_2) \Theta(m - m_1 - m_2)$$

Although our fragmentation model (see Chapter 6) provides a very detailed description of the outcome of a collision, we abandon most of the details for the following reasons. The computational effort of the numerical solution of the coagulation equation scales with the third power of the number of mass bins. Hence we chose a mass grid whose resolution is by far smaller than the information provided by the detailed collisional model. As a mismatch of the mass resolution could produce undesired artifacts, a lower resolution of the collisional model is needed for consistency. Thus only the largest fragment $f_l(f_l^i, \gamma)$ and the second fragment $f_l^{(2)}(f_l^i, \gamma)$ (which contains information on reaccumulation) enter the fragment size distribution:

$$M_{\text{red}}(xM)/M = \begin{cases} 1 & \text{if } x \geq f_l \\ 1 - f_l & \text{if } f_l > x \geq f_l^{(2)} \\ (1 - f_l - f_l^{(2)})(x/f_l^{(2)})^{f_l} & \text{otherwise} \end{cases} \quad (7.73)$$

Both values f_l and $f_l^{(2)}$ are interpolated from table 6.1, where the initial fragment size f_l^i is calculated from the dimensionless impact energy ϵ . We used a reduced fragmentation model for test purposes:

$$M_{\text{red}}(xM)/M = \begin{cases} 1 & \text{if } x \geq f_l \\ (1 - f_l)(x/f_l)^{f_l} & \text{otherwise} \end{cases} \quad (7.74)$$

Table 7.1 summarises the most important model parameters.

Chapter 8

Statistical Model

8.1 Fokker–Planck Equation

The direct approach to the integration of an N -body system is, in principle, possible for any particle number. While this procedure becomes computationally too expensive for very large particle numbers, a by far more efficient approach is applicable in this regime. Instead of tracking all particle orbits, a *distribution function* f (also *phase-space density*), which gives the probability to find a particle at a position \mathbf{x} with a velocity \mathbf{v} , contains the state of the system:

$$dp = f(\mathbf{x}, \mathbf{v}) d^3x d^3v \quad (8.1)$$

As long as only dynamical interactions are taken into account, the number of all particles (e.g. stars, planetesimals) is conserved. The continuity equation reads:

$$0 = \frac{\partial f}{\partial t} + \mathbf{v} \cdot \nabla f - \nabla \Phi \cdot \frac{\partial f}{\partial \mathbf{v}} \quad (8.2)$$

This is the *collisionless Boltzmann equation*. Collisions lead to an additional term

$$\left(\frac{\partial f}{\partial t} \right)_{\text{coll}} = \frac{\partial f}{\partial t} + \mathbf{v} \cdot \nabla f - \nabla \Phi \cdot \frac{\partial f}{\partial \mathbf{v}} \quad (8.3)$$

which will be discussed later. f is a function of six variables, so an exact solution is usually very complicated or even impossible. However, it is possible to gain valuable insight into the problem by taking the *moments* of the distribution function:

$$\langle x_i^n v_j^m \rangle = \int f(\mathbf{x}, \mathbf{v}) x_i^n v_j^m d^3x d^3v \quad n, m > 0 \quad (8.4)$$

The spatial density (particles per volume) is related to distribution function:

$$\nu(\mathbf{x}) = \int f(\mathbf{x}, \mathbf{v}) d^3v \quad (8.5)$$

Integration of Eq. 8.3 over all velocities yields the corresponding continuity equation:

$$\frac{\partial \nu}{\partial t} + \frac{\partial \nu \bar{v}_i}{\partial x_i} = \left(\frac{\partial \nu}{\partial t} \right)_{\text{coll}} \quad (8.6)$$

The first order moment with respect to velocity gives the time evolution of the mean velocity \bar{v}

$$\nu \frac{\partial \bar{v}_j}{\partial t} + \nu \bar{v}_i \frac{\partial \bar{v}_j}{\partial x_i} = -\nu \frac{\partial \Phi}{\partial x_j} - \frac{\partial (\nu \sigma_{ij}^2)}{\partial x_i} + \nu \left(\frac{\partial \bar{v}_j}{\partial t} \right)_{\text{coll}} \quad (8.7)$$

$$\bar{v}_i = \int f(\mathbf{x}, \mathbf{v}) v_i d^3v \quad (8.8)$$

$$\sigma_{ij}^2 = \overline{v_i v_j} - \bar{v}_i \bar{v}_j \quad (8.9)$$

where σ_{ij} is the anisotropic velocity dispersion and the continuity equation was used to arrive at a more concise formulation. Equations 8.6 and 8.7 are the *Jeans equations*. While the structure of the moment equations is already familiar from hydrodynamics, they do not provide a closed set of differential equations, since each differential equation of a given moment is related to (yet unknown) higher order moments. Hence any finite set of momenta needs a *closure relation* – additional constraints that relate the highest order moments to known quantities. The choice of this relation is a key element in the validity of the equations, but it is not unique and depends well on the problem at hand (compare e. g. Larson 1970 [92]).

Owing to the geometry of a planetesimal disc, it is useful to state the Boltzmann equation in cylindrical coordinates

$$\frac{\partial f}{\partial t} + v_r \frac{\partial f}{\partial r} + v_z \frac{\partial f}{\partial z} + \left(\frac{v_\phi^2}{r} - \frac{\partial \Phi}{\partial r} \right) \frac{\partial f}{\partial v_r} - \frac{v_r v_\phi}{r} \frac{\partial f}{\partial v_\phi} - \frac{\partial \Phi}{\partial z} \frac{\partial f}{\partial v_z} = 0 \quad (8.10)$$

where all derivatives with respect to ϕ have been dropped due to the assumed axisymmetry of the disc.

8.2 Distribution Function

Any statistical description of a planetesimal disc requires the knowledge of the distribution function. Since the full problem including collisions, encounters and gas drag has no analytic solution, a collisionless planetesimal disc (i. e. no perturbations) is a natural basis for further investigations. The distribution function that describes such a simplified system is a solution of the Boltzmann equation. A special solution to Eq. 8.10 is a thin homogenous planetesimal disc

$$f(z, v) = \frac{\Omega \Sigma}{2\pi^2 T_r T_z m} \exp \left(-\frac{v_r^2 + 4v_\phi^2}{2T_r} - \frac{v_z^2 + \Omega^2 z^2}{2T_z} \right) \quad (8.11)$$

provided that the radial velocity dispersion T_r and the vertical dispersion T_z are small compared the mean orbital velocity v_K . The azimuthal velocity dispersion T_ϕ is locked to T_r by the local epicyclic frequency κ in a central potential, where the ratio 1 : 4 is a special solution of (see e. g. Binney and Tremaine 1994 [20])

$$\kappa^2 T_r = 4\Omega^2 T_\phi \quad (8.12)$$

All velocities v_r , v_ϕ and v_z refer to the local Keplerian velocity. The normalisation is the same as in Stewart and Ida 2000 [137]:

$$\int d^3v dz f(z, v) = \frac{\Sigma}{m} \quad (8.13)$$

A planetesimal disc is a slowly evolving system compared to the orbital time, hence it is reasonable to use Eq. 8.11 as a general solution of the perturbed problem. Σ , T_z and T_r are now functions of time and of the radial distance to the star. All information on the system is contained in these three momenta of the distribution function, where higher order moments can be deduced from Eq. 8.11. Thus the functional form of the distribution function represents an implicit closure relation.

The validity of this approximation can be further assessed by a closer examination of the Boltzmann equation. We summarise all perturbations in an evolution timescale T_{evol} and reduce the radial structure to some typical length scale Δr to estimate the deviation from the functional form Eq. 8.11. A comparison with Eq. 8.10 shows that the difference is small if the migration timescale and the evolution timescale are large compared to the orbital time T_0 :

$$T_0 \ll \Delta r / \langle v_r \rangle \quad (8.14)$$

$$T_0 \ll T_{\text{evol}} \quad (8.15)$$

An order-of-magnitude estimate of the evolution time supports condition 8.14 and 8.15. Furthermore, numerical calculations confirm that the velocity distribution stays triaxial gaussian (see Ida and Makino 1992 [62]).

The distribution function is equivalent to an isothermal vertical density structure with scale height h :

$$h = \sqrt{\frac{T_z}{\Omega^2}} \quad (8.16)$$

$$\rho(z) = \rho_0 \exp\left(-\frac{z^2}{2h^2}\right) \quad (8.17)$$

Thus the central density ρ_0 and the mean density $\langle\rho\rangle$ are related to the surface density in a simple way:

$$\rho_0 = \frac{\Sigma}{\sqrt{2\pi}h} \quad (8.18)$$

$$\langle\rho\rangle = \frac{\rho_0}{\sqrt{2}} \quad (8.19)$$

The triaxial gaussian velocity distribution is equivalent to a *Rayleigh distribution* of the orbital elements e and i^1 :

$$dn(e^2, i^2) = \frac{1}{\langle e^2 \rangle \langle i^2 \rangle} \exp\left(-\frac{e^2}{\langle e^2 \rangle} - \frac{i^2}{\langle i^2 \rangle}\right) de^2 di^2 \quad (8.20)$$

$$\langle e^2 \rangle = \frac{2T_r}{(\Omega r_0)^2} \quad \langle i^2 \rangle = \frac{2T_z}{(\Omega r_0)^2} \quad (8.21)$$

Planetesimal encounters couple the time evolution of eccentricity and inclination, so that the ratio i^2/e^2 tends to an equilibrium value after a few relaxation times. It is close to 1/4 in a Kepler potential, but the precise value also depends on the potential itself (Ida et al. 1993 [63]).

8.3 Dynamical Friction

Planetesimal–planetesimal scatterings change the velocity distribution through two different processes. Firstly, it is unlikely that two planetesimals scatter each other on circular orbits. Thus we expect a steady increase of the velocity dispersion due to this *viscous stirring*. Secondly, encounters between unequal masses lead successively to energy equipartition, slowing down the larger bodies through *dynamical friction*. The later mechanism is not related to the disc geometry at all, but operates in any multi-mass system. A special case is the systematic deceleration of a massive body M in a homogeneous sea of lighter particles m with density n_0 , which is given by the *Chandrasekhar dynamical friction formula* (Chandrasekhar 1942 [32])

$$\frac{d\mathbf{v}_M}{dt} = -\mathbf{v}_M \frac{4\pi \ln \Lambda G^2 (M+m) n_0 m}{v_M^3} \left(\operatorname{erf}(X) - \frac{2X}{\sqrt{\pi}} e^{-X^2} \right) \quad (8.22)$$

$$X = \frac{v_M}{\sqrt{2}\sigma_v} \quad (8.23)$$

where σ_v is the velocity dispersion of the lighter particles. The *coulomb logarithm* Λ arises from an integration over all impact parameters smaller than an upper limit l_{\max} and is given by

$$\Lambda \approx \frac{\sigma_v^2 l_{\max}^2}{G(m+M)} \quad (8.24)$$

Although encounters in the gravitational field of the sun deviate from pure two-body scatterings, it is safe to neglect the presence of the sun if the encounter velocity is large compared to the *Hill velocity*² ΩR_{Hill} . Thus the classical dynamical friction formula is also applicable to planetesimal

¹Eq. 3.20–3.21 provide the coordinate transformation.

²Whenever relative velocities are classified as ‘high’ or ‘low’ in the following sections, a comparison with the Hill velocity is implied.

encounters in the high velocity regime, though a generalisation to triaxial velocity distributions σ_i is necessary (see e. g. Binney 1977 [19]):

$$\frac{dv_{M,i}}{dt} = -v_{M,i}\sqrt{2\pi}G^2 \ln(\Lambda)(M+m)n_0mB_i \quad (8.25)$$

$$B_i = \int_0^\infty \exp\left(-\frac{1}{2}\sum\frac{v_j^2}{\sigma_j^2+u}\right) \frac{du}{\sqrt{(\sigma_1^2+u)(\sigma_2^2+u)(\sigma_3^2+u)(\sigma_i^2+u)}} \quad (8.26)$$

An additional complication is the choice of l_{\max} (i. e. the choice of the coulomb logarithm). There are several scale lengths, which could determine the largest impact parameter l_{\max} : The scale height of the planetesimal disc, the radial excursion due to the excentric motion of the planetesimals and the Hill radius of the planetesimals. As it is not possible to derive a unique expression for l_{\max} from first principles, a proper formula is often fitted to N -body calculations (compare Eq. 8.56). The velocity dispersion of a planetesimal disc is triaxial with $T_\phi/T_r = 1/4$ and $T_z/T_r \approx 1/4$. We take these values and expand Eq. 8.25 for small velocities v_M :

$$\frac{dv_{M,r}}{dt} \approx -1.389 v_{M,r} \frac{\sqrt{2\pi}G^2 \ln(\Lambda)(M+m)n_0m}{T_r^{3/2}} \quad (8.27)$$

$$\frac{dv_{M,\phi}}{dt} \approx -3.306 v_{M,\phi} \frac{\sqrt{2\pi}G^2 \ln(\Lambda)(M+m)n_0m}{T_r^{3/2}} \quad (8.28)$$

$$\frac{dv_{M,z}}{dt} \approx -3.306 v_{M,z} \frac{\sqrt{2\pi}G^2 \ln(\Lambda)(M+m)n_0m}{T_r^{3/2}} \quad (8.29)$$

The derived expressions provide a compact tool to analyse dynamical friction in disc systems. However, the involved approximations are too severe compared to the needs of an accurate description. While these concise expressions are valuable for basic estimations, the following sections derive viscous stirring and dynamical friction formulas for a planetesimal system in a rigorous way.

8.4 High Speed Encounters

We recede to the Boltzmann equation as a starting point for the derivation of the scattering coefficients:

$$\left(\frac{\partial f}{\partial t}\right)_{\text{coll}} = \frac{\partial f}{\partial t} + \mathbf{v} \cdot \nabla f - \nabla \Phi \cdot \frac{\partial f}{\partial \mathbf{v}} \quad (8.30)$$

In virtue of the ansatz for the distribution function (see Eq. 8.11), it is sufficient to derive the time derivative of the second order velocity moments T_r and T_z . Since the distribution function is time independent in the absence of encounters, only the collisional term contributes to the time derivative of the velocity dispersions T_k ($k \in (r, z, \phi)$ in the following):

$$\frac{d\rho T_k}{dt} = \int d^3v m v_k^2 \left(\frac{\partial f}{\partial t}\right)_{\text{coll}} \quad (8.31)$$

The collisional term invokes the averaging over many different scattering trajectories and is, given that the underlying encounter model is analytically solvable, still too complex to derive an exact expression. If most of the encounters are weak – a realistic assumption in a planetesimal disc – it is possible to expand the collisional contribution in terms of the velocity change Δv_i . This is the *Fokker-Planck approximation*. It writes (see e. g. Binney and Tremaine, 8-53 [20])

$$\left(\frac{\partial f}{\partial t}\right)_{\text{coll}} = -\sum_i \frac{\partial}{\partial v_i} [f D(\Delta v_i)] + \frac{1}{2} \sum_{i,j} \frac{\partial^2}{\partial v_i \partial v_j} [D(\Delta v_i, \Delta v_j)] \quad (8.32)$$

where the *diffusion coefficients* D contain all information on the underlying scattering process. Next we consider two interacting planetesimal populations m, m^* with distribution functions

$$f = \frac{\Omega\Sigma}{2\pi^2 T_r T_z m} \exp\left(-\frac{v_r^2 + 4v_\phi^2}{2T_r} - \frac{v_z^2 + \Omega^2 z^2}{2T_z}\right) \quad (8.33)$$

$$f^* = \frac{\Omega\Sigma^*}{2\pi^2 T_r^* T_z^* m^*} \exp\left(-\frac{v_r^2 + 4v_\phi^2}{2T_r^*} - \frac{v_z^2 + \Omega^2 z^2}{2T_z^*}\right) \quad (8.34)$$

to evaluate the terms in equation 8.32. We follow Stewart and Ida 2000 [137] except some minor changes in the notation. The collisional term requires an averaging over the velocities of the two interacting planetesimals m and m^* :

$$\frac{d\langle\rho v_k^2\rangle}{dt} = 2\pi G^2 m m^{*2} \int d^3 v \int d^3 v^* f f^* \times \left[-\frac{2A(m+m^*)u_k v_k}{m^* u^3} + \frac{B u^2 + (2C-B)3u_k^2}{u^3} \right] \quad (8.35)$$

$$u_k = v_k - v_k^* \quad (8.36)$$

$$A = \ln(\Lambda^2 + 1) \quad C = \frac{\Lambda^2}{\Lambda^2 + 1} \quad B = A - C \quad (8.37)$$

A coordinate transformation to the relative velocity u and the modified centre of mass velocity w

$$w_k = \begin{cases} V_k + \frac{(m^* T_r^* - m T_r) u_k}{(m+m^*)(T_r + T_r^*)} & \text{for } k \in \{r, \phi\} \\ V_k + \frac{(m^* T_z^* - m T_z) u_k}{(m+m^*)(T_z + T_z^*)} & \text{for } k = z \end{cases} \quad (8.38)$$

$$\mathbf{V} = \frac{m\mathbf{v} + m^*\mathbf{v}^*}{m+m^*} \quad (8.39)$$

further simplifies the double integral. Thus the integration separates in a simple integral over w and a more demanding u -integration:

$$\frac{d\langle\rho v_r^2\rangle}{dt} = 2\pi G^2 m m^{*2} \int d^3 w \int d^3 u f f^* \times \left[\frac{2A(m^* T_r^* - m T_r) u_r^2}{m^* (T_r + T_r^*) u^3} + \frac{B(u^2 - 3u_r^2)}{u^3} \right] \quad (8.40)$$

$$\frac{d\langle\rho v_\phi^2\rangle}{dt} = 2\pi G^2 m m^{*2} \int d^3 w \int d^3 u f f^* \times \left[\frac{2A(m^* T_r^* - m T_r) u_\phi^2}{m^* (T_r + T_r^*) u^3} + \frac{B(u^2 - 3u_\phi^2)}{u^3} \right] \quad (8.41)$$

$$\frac{d\langle\rho v_z^2\rangle}{dt} = 2\pi G^2 m m^{*2} \int d^3 w \int d^3 u f f^* \times \left[\frac{2A(m^* T_z^* - m T_z) u_z^2}{m^* (T_z + T_z^*) u^3} + \frac{B(u^2 - 3u_z^2)}{u^3} \right] \quad (8.42)$$

f	J_r	J_ϕ	J_z	H_r	H_ϕ	H_z
c_0	-10.34660733	1.81674741	8.52985992	11.00434580	6.94989422	4.71219005
c_1	4.69990443	2.95397208	-7.65387651	-2.64707927	-2.06510182	1.47084771
c_2	-1.25533220	-1.18724874	2.44258094	0.60969641	0.58700192	-0.62294130
c_3	0.30288875	0.37775788	-0.68064662	-0.13815856	-0.16311494	0.18968657
c_4	-0.07040537	-0.11070339	0.18110876	0.03112047	0.04455314	-0.05271757
c_5	0.01540098	0.02922947	-0.04463045	-0.00669979	-0.01130929	0.01331068
Δ	0.006	0.015	0.022	0.0025	0.0058	0.0066

Table 8.1: Chebyshev coefficients of the auxiliary functions J_k and H_k .

All integrals are solvable and give the result

$$\frac{d\langle v_{r,\phi}^2 \rangle}{dt} = \frac{G^2 \rho^*}{2\sqrt{2}(T_r + T_r^*)^{3/2}} \times [B(T_r^* + T_r)m^* J_{r,\phi}(\beta) + 2A(T_r^* m^* - mT_r)H_{r,\phi}(\beta)] \quad (8.43)$$

$$\frac{d\langle v_z^2 \rangle}{dt} = \frac{G^2 \rho^*}{2\sqrt{2}(T_r + T_r^*)^{1/2}(T_z + T_z^*)} \times [B(T_z^* + T_z)m^* J_z(\beta) + 2A(T_z^* m^* - mT_z)H_z(\beta)] \quad (8.44)$$

$$\beta^2 := \frac{T_z + T_z^*}{T_r + T_r^*} \quad (8.45)$$

where six auxiliary functions are introduced to arrive at a more compact notation:

$$a = \sqrt{4 - 3x^2} \quad b = \sqrt{1 - (1 - \beta^2)x^2} \quad (8.46)$$

$$H_r := 8\sqrt{\pi} \int_0^1 \frac{x^2}{ab} dx \quad (8.47)$$

$$H_\phi := 8\sqrt{\pi} \int_0^1 \frac{1 - x^2}{a(\beta a + b)} dx \quad (8.48)$$

$$H_z := 8\sqrt{\pi} \int_0^1 \frac{\beta(1 - x^2)}{b(\beta a + b)} dx \quad (8.49)$$

$$J_r := -2H_r + H_\phi + H_z \quad (8.50)$$

$$J_\phi := H_r - 2H_\phi + H_z \quad (8.51)$$

$$J_z := H_r + H_\phi - 2H_z \quad (8.52)$$

Since these are non-trivial functions, we apply a standard Chebyshev approximation for $\beta \in [0, 1]$:

$$f(x) \approx \sum_{k=0}^5 c_k T_k(x) - \frac{1}{2}c_0 \quad (8.53)$$

Table 8.1 summarises the Chebyshev coefficients. A final z -averaging yields the expressions:

$$\frac{d\langle v_{r,\phi}^2 \rangle}{dt} = \frac{G^2 \Omega \Sigma^*}{4\sqrt{\pi}(T_r + T_r^*)^{3/2}(T_z + T_z^*)^{1/2}} \times [B(T_r^* + T_r)m^* J_{r,\phi}(\beta) + 2A(T_r^* m^* - mT_r)H_{r,\phi}(\beta)] \quad (8.54)$$

$$\frac{d\langle v_z^2 \rangle}{dt} = \frac{G^2 \Omega \Sigma^*}{4\sqrt{\pi}(T_r + T_r^*)^{1/2}(T_z + T_z^*)^{3/2}} \times [B(T_z^* + T_z)m^* J_z(\beta) + 2A(T_z^* m^* - mT_z)H_z(\beta)] \quad (8.55)$$

The determination of a proper coulomb logarithm Λ leaves room for further optimisation.

A careful comparison with N -body models gives rise to the empirical choice (Ohtsuki et al. 2002 [116]):

$$\Lambda = \frac{1}{12}(\langle \tilde{e}^2 \rangle + \langle \tilde{i}^2 \rangle) \langle \tilde{i}^2 \rangle^{1/2} \quad (8.56)$$

$$\tilde{e} = \frac{\sqrt{2T_r}}{\Omega R_{\text{Hill}}} \quad \tilde{i} = \frac{\sqrt{2T_z}}{\Omega R_{\text{Hill}}} \quad (8.57)$$

Ohtsuki et al. 2002 also report a further improvement by setting $B \equiv A$.

8.5 Low Speed Encounters

Encounters in the low velocity regime exhibit a wealth of different orbits, as the solar gravity field perturbs the two-body scattering. Only a small subset of the trajectories represents simple, regular orbits like Tadpole or Horseshoe orbits³. Hence an examination of this velocity regime is done best with a numerical study of the parameter space by integrating the equations of motions numerically (see Eq. 3.29).

Ohtsuki et al. 2002 [116] integrated a large set of planetesimal encounters and extracted fitting formulas that cover the low velocity regime. Their expressions for viscous stirring are:

$$\frac{dT_r}{dt} = \frac{Gr_0\Omega h\Sigma^*}{6(m+m^*)} 73C_1 m^* \quad (8.58)$$

$$\frac{dT_z}{dt} = \frac{Gr_0\Omega h\Sigma^*}{6(m+m^*)} C_2 m^* \left(4\langle \tilde{i}^2 \rangle + 0.2(\langle \tilde{e}^2 \rangle)^{3/2} \sqrt{\langle \tilde{i}^2 \rangle} \right) \quad (8.59)$$

$$\tilde{e} = e/h \quad \tilde{i} = i/h \quad (8.60)$$

$$C_1 := \frac{\ln(10\Lambda^2/\tilde{e}^2 + 1)}{10\Lambda^2/\tilde{e}^2} \quad (8.61)$$

$$C_2 := \frac{\ln(10\Lambda^2\sqrt{\tilde{e}^2} + 1)}{10\Lambda^2\sqrt{\tilde{e}^2}} \quad (8.62)$$

The stirring rate of the radial velocity dispersion approaches a finite value for very low velocity dispersions, while the stirring rate for the vertical velocity dispersion drops to zero as the velocity dispersion decreases. This different behaviour of the two limits is due to the encounter geometry: If two planetesimals have zero inclination, they may still excite higher eccentricities during an encounter, but they remain confined to the initial orbital plane preventing any excitation of inclinations.

The respective expressions for the dynamical friction rates are:

$$\frac{dT_r}{dt} = \frac{Gr_0\Omega h\Sigma^*}{6(m+m^*)(T_r+T_r^*)} 10C_3 \langle \tilde{e}^2 \rangle (T_r^* m^* - T_r m) \quad (8.63)$$

$$\frac{dT_z}{dt} = \frac{Gr_0\Omega h\Sigma^*}{6(m+m^*)(T_z+T_z^*)} 10C_3 \langle \tilde{i}^2 \rangle (T_z^* m^* - T_z m) \quad (8.64)$$

$$C_3 := \frac{\ln(10\Lambda^2 + 1)}{10\Lambda^2} \quad (8.65)$$

As the stirring rates are only valid in the low velocity regime, Ohtsuki et al. 2002 [116] introduced special interpolation coefficients C_i . These coefficient tend to unity for very small velocity dispersions, and drop to zero in the high velocity regime. Thus the interpolation formulas are properly ‘switched off’ in the high velocity regime, so they do not interfere with the known high velocity stirring rates.

³The most famous example of such a regular orbit are the two saturnian moons Janus and Epimetheus which share nearly the same orbit.

8.6 Distant Encounters

All formulas include only the stirring rates due to close encounters, but non-crossing orbits also contribute to the overall change of the velocity distribution. As these distant encounters lead to small changes of the orbital elements, the problem is accessible to perturbation theory (see Hasegawa and Nakazawa 1990 [51] for a detailed treatment). Stewart and Ida 2000 [137] integrated the perturbation solution over all impact parameters to derive the collective effect of all distant encounters:

$$\frac{d\langle e^2 \rangle}{dt} = \frac{\Omega m^* \Sigma^* r_0^2}{(m + m^*)^2} \langle P_{VS,dist} \rangle \quad (8.66)$$

$$\langle P_{VS,dist} \rangle = 7.6 \frac{\alpha (m + m^*)^2}{M_c^2} \times \quad (8.67)$$

$$\frac{\text{EXINT} \left(\alpha \frac{h^2}{(\langle e^2 \rangle + \langle e^{*2} \rangle)} \right) - \text{EXINT} \left(\alpha \frac{h^2}{(\langle i^2 \rangle + \langle i^{*2} \rangle)} \right)}{\langle e^2 \rangle + \langle e^{*2} \rangle - \langle i^2 \rangle - \langle i^{*2} \rangle}$$

$$\text{EXINT}(x) := \exp(x) \Gamma(0, x) \quad h = \sqrt[3]{\frac{m + m^*}{3M_c}} \quad (8.68)$$

$$\alpha \approx 1 \quad (8.69)$$

α accounts for the uncertainty in the smallest impact parameter that is regarded as a distant encounter. While distant encounters are already included in the interpolation formula of the low-velocity regime, we use the modified expression:

$$\left(\frac{dT_r}{dt} \right)_{\text{dist}} = \frac{1}{2} (\Omega r_0)^2 \left(\frac{d\langle e^2 \rangle}{dt} \right)_{\text{dist}} (1 - C_1) \quad (8.70)$$

$$= \frac{GM_c r_0 \Omega m^* \Sigma^*}{2(m + m^*)^2} \langle P_{VS,dist} \rangle (1 - C_1) \quad (8.71)$$

Stewart and Ida 2000 [137] omitted the change in the inclination, as it is small due to the encounter geometry. Nevertheless we derived the integrated stirring rate for completeness:

$$\frac{d\langle i^2 \rangle}{dt} = \frac{\Omega m^* \Sigma^* r_0^2}{(m + m^*)^2} \langle Q_{VS,dist} \rangle \quad (8.72)$$

$$\langle Q_{VS,dist} \rangle = 0.4 \frac{\alpha^2 (m + m^*)^2}{M_c^2} \times \frac{1}{\langle e^2 \rangle + \langle e^{*2} \rangle - \langle i^2 \rangle - \langle i^{*2} \rangle} \times \quad (8.73)$$

$$\left(1 - \frac{\alpha h^2}{\langle i^2 \rangle + \langle i^{*2} \rangle} \text{EXINT} \left(\alpha \frac{h^2}{(\langle i^2 \rangle + \langle i^{*2} \rangle)} \right) \right. \\ \left. - (\langle i^2 \rangle + \langle i^{*2} \rangle) \frac{\text{EXINT} \left(\alpha \frac{h^2}{(\langle e^2 \rangle + \langle e^{*2} \rangle)} \right) - \text{EXINT} \left(\alpha \frac{h^2}{(\langle i^2 \rangle + \langle i^{*2} \rangle)} \right)}{\langle e^2 \rangle + \langle e^{*2} \rangle - \langle i^2 \rangle - \langle i^{*2} \rangle} \right)$$

A close inspection of the integrated perturbation shows that the above formula is roughly a factor $\langle i^2 \rangle + \langle i^{*2} \rangle$ smaller than the corresponding changes in the eccentricity.

8.7 Gas Damping

The presence of a gaseous disc damps the velocity dispersion of the planetesimals and introduces a slow inward migration. Adachi et al. 1976 [6] used the drag law Eq. 4.37 to approximate⁴ the

⁴A formal expansion at $e = 0$, $i = 0$, $\eta_g = 0$ is not possible, since the drag law involves the modulus of the relative velocity. Kary et al. 1993 [72] corrected a missing factor 3/2 in Eq. 8.75.

average change of the orbital elements:

$$\tau_0 = \frac{2m}{\pi C_D \rho_g R^2 v_K} \quad \eta_g = \frac{|v_K - v_g|}{v_K} \quad (8.74)$$

$$\frac{d}{dt}e^2 \approx -\frac{2e^2}{\tau_0} \left(0.77e + 0.64i + \frac{3}{2}\eta_g \right) \quad (8.75)$$

$$\frac{d}{dt}i^2 \approx -\frac{2i^2}{\tau_0} \left(0.39e + 0.43i + \frac{1}{2}\eta_g \right) \quad (8.76)$$

$$\frac{d}{dt}a \approx -\frac{2a}{\tau_0} \eta_g (0.97e + 0.64i + \eta_g) \quad (8.77)$$

η_g is the dimensionless velocity lag of the sub-Keplerian rotating gaseous disc.

8.8 Unified Expressions

All expressions for the different velocity regimes are constructed such that a smooth transition between the different regimes is assured. Thus, a simple addition of all contributions yields already the unified expressions

$$\frac{dT_r}{dt} = \left(\frac{dT_r}{dt} \right)_{\text{high}} + \left(\frac{dT_r}{dt} \right)_{\text{low}} + \left(\frac{dT_r}{dt} \right)_{\text{gas}} + \left(\frac{dT_r}{dt} \right)_{\text{dist}} \quad (8.78)$$

$$\frac{dT_z}{dt} = \left(\frac{dT_z}{dt} \right)_{\text{high}} + \left(\frac{dT_z}{dt} \right)_{\text{low}} + \left(\frac{dT_z}{dt} \right)_{\text{gas}} + \left(\frac{dT_z}{dt} \right)_{\text{dist}} \quad (8.79)$$

which cover the full range of relative velocities. Although only two populations m and m^* were assumed, Eq. 8.78 and Eq. 8.79 are readily generalised to a multi-mass system by adding a summation over all masses.

8.9 Inhomogeneous Disc

The preceding derivations assumed a homogeneous disc. This simplified the calculation, since the integration over all impact parameters needed no special precaution. A more sophisticated consequence is, that the spatial density and the density in semimajor axis space are equal:

$$\Sigma(r) = \Sigma(a) = \Sigma_0 \quad (8.80)$$

Density inhomogeneities brake this simple relation, as a particles at the same radial distance could have different semimajor axes, and particles with the same semimajor axis are located at different positions at a given time. While both representations are equivalent (i. e. describe the same system in different ways), we chose the density in semimajor axis space as the primary density⁵. The spatial density is derived as:

$$\Sigma(r) = \int \frac{1}{\sqrt{2\pi a^2 \langle e^2(a) \rangle}} \exp\left(-\frac{(a-r)^2}{2a^2 \langle e^2(a) \rangle}\right) \Sigma(a) da \quad (8.81)$$

Likewise, T_r and T_z are also functions of the semimajor axis.

Furthermore, an inhomogeneous surface density invalidates the averaging over all impact parameters. Planetesimal encounter are most efficient for impact parameters smaller than a few Hill radii, so the derivation is still valid if the surface density is roughly constant on that length scale.

⁵We denote $\Sigma(a)$ also as ‘surface density’ and refer to a as a radial coordinate. However, all formulas are precise in discriminating both representations in r and a .

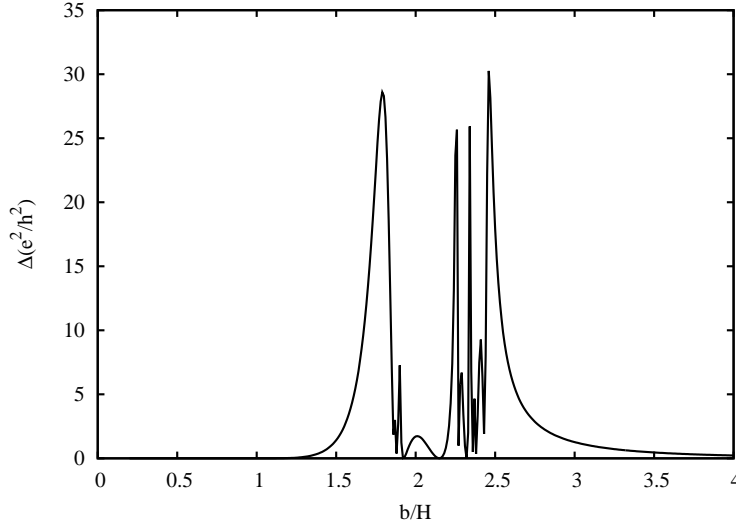


Figure 8.1: Change of the relative eccentricity e^2 due to an encounter of two bodies initially on circular orbits. b/H is the impact parameter in units of the Hill radius. The plot was obtained by integrating Eq. 3.29.

However, a planetesimal that is large enough will ‘feel’ the spatial inhomogeneities or even generates density fluctuations. Hence it is essential to extend the validity of the averaged expressions to inhomogeneous systems. We use the averaged expressions

$$\left\langle \frac{dT_{r,z}}{dt} \right\rangle = \Sigma(a) \int_{-\infty}^{\infty} \frac{d\tilde{T}_{r,z}(b)}{dt} db \quad (8.82)$$

as a starting point ($d\tilde{T}_{r,z}/dt$ excludes the surface density, as opposed to the averaged expressions). The (yet unknown) scattering contribution $d\tilde{T}_{r,z}/dt$ as a function of the impact parameter b is our starting point for a general expression for a varying surface density:

$$\frac{dT(a_0)_{r,z}}{dt} = \int_{-\infty}^{\infty} \Sigma(a_0 + b) \frac{d\tilde{T}_{r,z}(b)}{dt} db \quad (8.83)$$

We restate Eq. 8.83 in terms of a weight function $w(b)$:

$$\frac{dT(a_0)_{r,z}}{dt} = \left\langle \frac{dT_{r,z}}{dt} \right\rangle \frac{1}{\Sigma(a_0)} \int_{-\infty}^{\infty} \Sigma(a_0 + b) w(b) db \quad (8.84)$$

$$w(b) = \Sigma(a_0) \frac{d\tilde{T}_{r,z}(b)}{dt} \left\langle \frac{dT_{r,z}}{dt} \right\rangle^{-1} \quad (8.85)$$

The numerical solution of the Hill problem (see Eq. 3.29) gives some insight into how the weight function $w(b)$ changes with the impact parameter. Fig. 8.1 shows exemplary the change in e^2 of the relative motion during an encounter of two planetesimals that were initially on circular orbits. While the details depend on the initial inclination and eccentricity as well as on the selected orbital element, all result share some basic features. Small (compared to the Hill radius) impact parameters allow for a horseshoe orbit and the change in the orbital elements is small except a change in the semimajor axis. Intermediate impact parameters which lead to close encounters provide the strongest perturbation, but they are also more susceptible to complicated dynamics (compare the resonant structures in Fig. 8.1). As the gravitational attraction drops with increasing distance, non-crossing orbits yield ever smaller perturbations with increasing impact parameter.

Aside from this qualitative behaviour, it is very difficult to derive precise expressions. While the limit of high velocities is accessible through the two-body approximation, any general formula involves some empiric interpolation to cover the full parameter space (see the approximations of Rafikov 2003 [126], 2003b [127]). Therefore we decided to approximate the weight function such that the main features of the true weight function $w(b)$ are reproduced. While this approach is less accurate, it provides better insight into the involved approximations. We expand the surface density under the integral in Eq. 8.84 and compare the expansion coefficients for $w(b)$ and the approximation $\tilde{w}(b)$ to derive constraints on the choice of $\tilde{w}(b)$. The lowest non-vanishing order is:

$$l^2 = \int_{-\infty}^{\infty} b^2 w(b) db = \int_{-\infty}^{\infty} b^2 \tilde{w}(b) db \quad (8.86)$$

l can be interpreted as the width of the heating zone. Condition 8.86 inspires our choice of the weight function $\tilde{w}(b)$

$$\tilde{w}(b) = \frac{1}{\sqrt{2\pi}l} \exp\left(-\frac{b^2}{2l^2}\right) \quad (8.87)$$

$$l^2 = \frac{1}{\Omega^2} (T_r^{(i)} + T_r^{(j)}) + R_{\text{Hill}}^2 \quad (8.88)$$

where $T_r^{(i)}$ and $T_r^{(j)}$ are the radial velocity dispersions of the interacting radial bins and l is adjusted to the findings of Ida and Makino 1993b [64]. The advantage of the bell curve is that it has a discrete counterpart

$$\tilde{w}(b) \approx \frac{1}{\Delta a 2^N} \binom{N}{b/\Delta a + N/2} \quad N = 4l^2/(\Delta a)^2 \quad (8.89)$$

which makes the weight function readily applicable to the summation on an equidistant radial grid with spacing Δa .

8.10 Diffusion Coefficient

We concentrated on the evolution of the velocity dispersion so far, but scatterings among planetesimals also change the semimajor axis of the disc particles, inducing a diffusive evolution of the surface density:

$$\frac{\partial \Sigma}{\partial t} = \Delta_a (D \Sigma) \quad (8.90)$$

The *diffusion coefficient* D is related to the typical change in semimajor axis Δa and the timescale $T_{2\text{Body}}$ on which planetesimal encounters operate:

$$D \approx \frac{(\Delta a)^2}{T_{2\text{Body}}} \quad (8.91)$$

If we neglect the radial displacement during an encounter, the change in semimajor axis is solely due to the change of the velocity:

$$-\frac{GM}{2a} = -\frac{GM}{r} + \frac{1}{2}v^2 \quad (8.92)$$

$$\Delta a \approx \frac{2a^2}{GM} \mathbf{v} \cdot \Delta \mathbf{v} \quad (8.93)$$

An average over all orientations of the velocity \mathbf{v} and the velocity change $\Delta \mathbf{v}$ yields the mean square change in semimajor axis:

$$\langle (\Delta a)^2 \rangle \approx \frac{4a^3}{3GM} \langle (\Delta v)^2 \rangle \quad (8.94)$$

$$= \frac{4}{3\Omega^2} (\Delta T_r + \Delta T_\phi + \Delta T_z) \quad (8.95)$$

This yields the mean diffusion coefficient

$$D \approx \frac{4}{3\Omega^2} \left(\frac{5}{4} \frac{d}{dt} T_r + \frac{d}{dt} T_z \right) \quad (8.96)$$

where the time derivatives of the velocity dispersions T_r and T_z are taken with respect to encounters.

8.11 Coagulation Equation

We already stated the coagulation equation for a multi-mass system:

$$0 = \frac{\partial}{\partial t} mn(t, m) + \frac{\partial}{\partial m} F_m(t, m) \quad (8.97)$$

$$F_m = - \iint n_1(t, m_1) n_2(t, m_2) \sigma(m_1, m_2) v_{\text{rel}} M_{\text{red}}(m, m_1, m_2) dm_1 dm_2 \quad (8.98)$$

Since the vertical density profile of a planetesimal disc is specified by the known distribution function, we insert the isothermal density profile (see Eq. 8.17) in the coagulation equation 8.97 and integrate over z :

$$0 = \frac{\partial}{\partial t} \Sigma(t, m) + \frac{\partial}{\partial m} F_m(t, m) \quad (8.99)$$

$$F_m = - \iint \frac{1}{\sqrt{2\pi(h(m_1)^2 + h(m_2)^2)}} \frac{\Sigma_1(t, m_1)}{m_1} \frac{\Sigma_2(t, m_2)}{m_2} \times \tilde{\sigma}(m_1, m_2) v_{\text{rel}} M_{\text{red}}(m, m_1, m_2) dm_1 dm_2 \quad (8.100)$$

$\Sigma(m)$ is a short-hand notation for the differential surface density $\frac{d\Sigma}{dm}$. Further integration over all masses gives the total mass balance:

$$\Sigma_{\text{tot}} = \int_{m_{\text{min}}}^{m_{\text{max}}} \Sigma(t, m) dm \quad (8.101)$$

$$\frac{\partial}{\partial t} \Sigma_{\text{tot}} = F_m(m_{\text{min}}) - F_m(m_{\text{max}}) \quad (8.102)$$

The calculation of collisional cross sections is closely related to the underlying encounter dynamics. A homogenous system introduces no systematic perturbation, hence an encounter is a pure two-body problem which is analytically solvable. Thus it is possible to derive the cross section without any approximation. Since encounters in the field of a central star deviate noticeably from the pure Kepler solution, the cross sections are also modified. While the cross section in the high velocity regime reduces to the two-body formula (except minor corrections), the low velocity regime is explored best by numerical calculations. It is not appropriate to disentangle the different contributions in Eq. 8.100, but to combine the various terms to the *collisional probability*

$$P_{\text{coll}} = \frac{\tilde{\sigma}(m_1, m_2) v_{\text{rel}}}{\sqrt{2\pi(h(m_1)^2 + h(m_2)^2)}} \quad (8.103)$$

which can be easily deduced from the fraction of colliding orbits in Monte-Carlo simulations. An accurate expression for the collisional probability should include the two-body cross section in the limit of high velocities and the numerical data for the low velocity regime as well. We use numerical calculations from Greenberg and Botke 1991 [48] and Greenzweig and Lissauer 1992

[50]⁶ as a basis for a unified fitting formula

$$\tilde{\sigma} = \sigma \times 0.572 (1 + 3.67v_{\text{Hill}}/v_{\text{rel}}) \left(1 + 1.0 \frac{\sigma \Omega^2}{T_z}\right)^{-1/2} \quad (8.104)$$

$$\sigma = \sigma_{\text{geom}} \left(1 + \frac{v_{\infty}^2}{v_{\text{rel}}^2 + 1.8v_{\text{Hill}}^2}\right) \quad (8.105)$$

$$v_{\text{rel}}^2 = \frac{1}{2}(T_r + T_{\phi} + T_z) \quad v_{\text{Hill}} = \Omega r_{\text{Hill}} \quad (8.106)$$

which gives an effective cross section $\tilde{\sigma}$ for planetesimal–planetesimal encounters. Eq. 8.104 reduces to the well-known gravitational focusing formula in the limit of high velocities:

$$\tilde{\sigma} \propto \sigma_{\text{geom}} \left(1 + \frac{v_{\infty}^2}{v_{\text{rel}}^2}\right) \quad (8.107)$$

$$v_{\infty}^2 = \frac{2G(m_1 + m_2)}{R_1 + R_2} \quad (8.108)$$

If the vertical velocity dispersion is small, the disc becomes two-dimensional and the cross section is proportional to R . The main differences to the two-body cross section 8.107 is a finite gravitational focusing factor, since the Keplerian shear inhibits a zero relative velocity, and a finite collisional probability for very small velocities, again due to the shear which provides a finite influx of particles.

The precise calculation of the coagulation kernel should include an integration over all semi-major axes with a proper weighting kernel. As collisions among particles in the statistical model play only a major role when the system is still homogenous, we omitted this contribution. In addition, this helps saving computational time, since the solution of the coagulation equation is very costly. However, interactions between N -body particles and the statistical model include spatial inhomogeneities properly (see Chapter 9).

8.12 Collisional Damping

Collisions are a dissipative process that removes kinetic energy from the planetesimal system. Low speed encounters leave the colliding bodies intact and damp the relative velocities through inelastic collisions. In contrast, high velocity encounters disrupt the colliding bodies and turn them into an expanding cloud of fragments. As a major part of the initial kinetic energy is converted into heat, the fragments disperse with rather low velocities thus reducing the overall velocity dispersion. We formulate the dissipation due to collisions analogue to Eq. 8.99:

$$0 = \frac{\partial}{\partial t} T_k \Sigma(t, m) + \frac{\partial}{\partial m} F_{Q,k}(t, m) \quad (8.109)$$

$$F_{Q,k} = - \iint \frac{1}{\sqrt{2\pi(h(m_1)^2 + h(m_2)^2)}} \frac{\Sigma_1(t, m_1)}{m_1} \frac{\Sigma_2(t, m_2)}{m_2} \times \tilde{\sigma}(m_1, m_2) v_{\text{rel}} Q_{\text{red},k}(m, m_1, m_2) dm_1 dm_2 \quad (8.110)$$

$$k \in \{r, z\} \quad (8.111)$$

$Q_{\text{red},k}$ is the *kinetic energy redistribution function* and $F_{Q,k}$ is the associated flux across the mass distribution. k indicates the two velocity dispersions. $Q_{\text{red},k}$ is a complex function, since the disruption of a planetesimal produces fragments with a large scatter in velocities and a complicated velocity field. The velocity of a fragment consists of two contributions: The ejection velocity relative to the target and the velocity \bar{v} of the target within the corotating coordinate system. Owing to the strong dissipation, fragment velocities are dominated by the motion of the centre of

⁶Their work includes an averaging over the rayleigh distributed inclinations and eccentricities of the colliding planetesimals.

mass of the two colliding bodies. Thus we neglect the ejection velocities and estimate the centre of mass motion. The initial kinetic energy of two colliding bodies is:

$$E_{\text{ini}} = \frac{1}{2}m_1v_1^2 + \frac{1}{2}m_2v_2^2 \quad (8.112)$$

We separate E_{ini} into centre of mass motion and relative motion and average over $\mathbf{v}_1, \mathbf{v}_2$:

$$E_{\text{ini}} = \frac{1}{2}M \left(\frac{m_1\mathbf{v}_1 + m_2\mathbf{v}_2}{M} \right)^2 + \frac{1}{2}\mu(v_1^2 + v_2^2) \quad (8.113)$$

$$\langle E_{\text{ini}} \rangle = \frac{1}{2M} (m_1^2T_1 + m_2^2T_2) + \frac{1}{2}\mu(T_1 + T_2) \quad (8.114)$$

Most of the relative kinetic energy is dissipated during the collision, so we neglect the relative motion after the incident. The final energy is

$$\frac{\langle E_{\text{final}} \rangle}{\langle E_{\text{ini}} \rangle} = \frac{m_1^2T_1 + m_2^2T_2}{M(m_1T_1 + m_2T_2)} \quad (8.115)$$

which gives the drift motion \bar{v} of the expanding fragment cloud:

$$\bar{v}^2 = \frac{2}{M} \langle E_{\text{final}} \rangle \quad (8.116)$$

Q_{red} is therefore coupled to the fragment redistribution function M_{red}

$$Q_{\text{red}} = \bar{v}^2 M_{\text{red}} + Q_{\text{diss}} \quad (8.117)$$

where the additional function Q_{diss} removes the dissipated energy.

8.13 Correlation

The statistical model of a planetesimal disc does not only require a large particle number to assure a proper description of the system by a distribution function, but also the *uncorrelated motion* of the planetesimals. Each of the afore derived formula involves the averaging over different impact parameters to some extent, in combination with the vital assumption that all distances are equally probable. As long as all particles are subjected to perturbations by surrounding bodies, strong correlations are suppressed. This applies to the early stages, but the formation of protoplanets introduces a few dominant bodies that are not susceptible to the perturbation of the field planetesimals. Orbit repulsion gives rise to a regular spacing of the protoplanets, which prevents mutual collisions. Therefore not all impact parameters are equally probable due to this strong correlation. Hence a statistical model is inherently not applicable to the late stages of protoplanetary growth.

Since statistical models are superior to N -body calculations with respect to speed and (effective) particle number, modifications have been proposed to remedy this problem.

The statistical model by Wetherill and Stewart 1993 [151] uses the following solution: A *gravitational range* Δa (or buffer zone) is attached to each planetesimal, which represents the minimal spacing that allows for stable orbits. They propose the expression

$$\Delta a = f_{\Delta} R_{\text{Hill}} + \sqrt{2T_r/\Omega^2} \quad (8.118)$$

where f_{Δ} is the minimal spacing in terms of the Hill radius. The value of f_{Δ} is adopted from Birn 1973 [21], who derived the minimal spacing that allows for stable orbits:

$$f_{\Delta} = 2\sqrt{3} \quad (8.119)$$

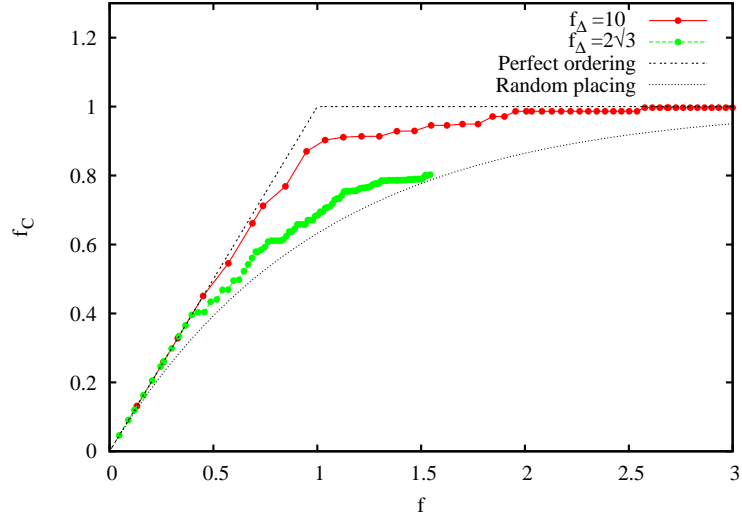


Figure 8.2: Covered fraction f_C as a function of f for simulation S1FB at $T = 10^5$ years. The protoplanets are already formed and grow oligarchically.

Thus it is possible to define a minimum mass m_{sep} by the assumption that all bodies larger than this critical mass maintain a clear buffer zone:

$$f = \int_{m_{\text{sep}}}^{\infty} \frac{d\Sigma}{dm} \frac{2\pi a \Delta a}{m} dm \quad (8.120)$$

$$f = 1 \quad (8.121)$$

f is the area covered by the buffer zones (overlapping is not taken into account, therefore $f > 1$ is possible), normalised to the ring area. Planetesimals smaller than m_{sep} can not enforce a minimum distance to their neighbours, as the whole disc surface is already covered by the buffer zones of the largest bodies. Owing to the regular spacing introduced by the buffer zones, planetesimals larger than the critical mass are not allowed to collide with each other. This approach has also been employed by Inaba et al. 2001 [67], who adopted $f_{\Delta} = 10$, which is the mean distance of protoplanets according to the orbit repulsion mechanism.

To shed light on the proper gravitational range and the validity of this approach, we defined an additional quantity f_C which is the true area (i. e. overlapping is handled properly) covered by the buffer zones in terms of the total area:

$$f_C = \int_{m_{\text{sep}}}^{\infty} \frac{d\Sigma}{dm} \frac{2\pi a (\Delta a)_C}{m} dm \quad (8.122)$$

$$f_C \leq 1 \quad (8.123)$$

Fig. 8.2 shows the covered fraction $f_C(m)$ as a function of the integrated buffer zones $f(m)$ for one of our hybrid calculations. Both values for f_{Δ} are included as well as the two limiting cases *random placing* and *perfect ordering*. Though we tested also other values of f_{Δ} , a spacing of ten Hill radii proved to be the best choice.

Our own experience with this method indicates that it works reasonable well, in accordance with Inaba et al. 2001 [67] who used the same technique. However, this modification includes the regular spacing of the protoplanets in a prescribed way, so any exploration of later stages, like the initiation of orbit crossing, is not accessible through this approach. Therefore we use it for comparison purposes only, since the hybrid code (see Chapter 9) provides a much more general framework.

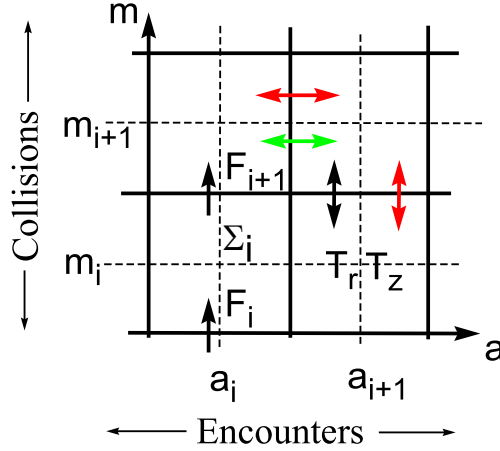


Figure 8.3: Numerical grid. The arrows indicate transport of kinetic energy (red), spatial transport of mass (green) and accretion (black). Non-neighbouring cells are coupled by the coagulation kernel and the radial interpolation kernel.

8.14 Discretisation

All involved quantities are only functions of a and m . Therefore we introduce a two dimensional grid, where Σ , T_r and T_z are cell centred quantities. Fig. 8.3 summarises the definition of the two-dimensional grid. Since the full planetesimal size range covers several orders of magnitude in mass, we chose a logarithmically equidistant discretisation in mass to cover the necessary mass range in a reliable way. The radial spacing of the grid cells is equidistant. Thus the grid setup for the mass discretisation reads (N grid cells from $m_{\min} \dots m_{\max}$):

$$m_i = m_{\min} \delta^{-i} (1/2 + \delta/2) \quad i = 1, \dots, N \quad (8.124)$$

$$\Delta m_i = m_{\min} \delta^{-i} (1 - \delta) \quad (8.125)$$

$$\Sigma_i = \frac{d\Sigma}{dm} \Delta m_i \quad (8.126)$$

$$\delta = \left(\frac{m_{\min}}{m_{\max}} \right)^{1/N} \quad (8.127)$$

The grid spacing δ controls the number of cells which are necessary to cover a specified mass range. As the evaluation of the coagulation equation scales with the third power of the number of grid cells, δ should be as large as possible. If the flux integral (see Eq. 8.97) is approximated in a standard way

$$F_i = - \sum_{j=1}^N \sum_{k=1}^N F_i^{(jk)} \quad (8.128)$$

$$F_i^{(jk)} = \frac{1}{\sqrt{2\pi(h_j^2 + h_k^2)}} \frac{\Sigma_j \Sigma_k}{m_j m_k} \times \sigma(m_j, m_k) v_{\text{rel}} M_{\text{red}}(m_i - \Delta m_i/2, m_j, m_k) \quad (8.129)$$

a spacing δ much smaller than 2 is required to guarantee a sufficient accuracy⁷. However, it is possible to use a spacing of 2 if special precaution is taken. Spaute et al. 1991 [133] approximated

⁷Ohtsuki et al. 1990 [113] give a thorough analysis of the importance of the resolution.

the surface density with a power law, thus taking the gradient with respect to mass into account. While they reached only a sufficient accuracy with further special adaptations, we use a more rigorous approach. A large spacing δ reduces the accuracy, since the partial flux (Eq. 8.129) is strongly varying even inside one grid cell. Thus we rearrange this expression to identify the most important terms:

$$F_i^{(jk)} = \frac{v_{\text{rel}}}{\sqrt{2\pi(h_j^2 + h_k^2)}} \frac{\Sigma_k}{m_k} \frac{\Sigma_j}{m_j} \times \underbrace{\sigma(m_j, m_k) m_j}_{F_V(m_j)} \frac{1}{m_j} M_{\text{red}}(m_i - \Delta m_i/2, m_j, m_k) \quad (8.130)$$

$$j \geq k \quad (8.131)$$

The strongest varying contribution F_V is now approximated by a power law with respect to m_j :

$$F_V(m) \approx F_V(m_j) \left(\frac{m}{m_j} \right)^q \quad (8.132)$$

Thus Eq. 8.132 is used to provide improved partial fluxes $F_i^{(jk)}$:

$$F_i^{(jk)} = \frac{v_{\text{rel}}}{\sqrt{2\pi(h_j^2 + h_k^2)}} \frac{\Sigma_k}{m_k} \int_{m_j - \Delta m_j/2}^{m_j + \Delta m_j/2} \frac{F_V(m)}{m \Delta m_j} M_{\text{red}}(m_i - \Delta m_i/2, m, m_k) dm \quad (8.133)$$

$$j \geq k \quad (8.134)$$

Since the fragment redistribution function is a piecewise power law, an analytical solution of the integral is possible. Eq. 8.133 gives reliable results even with a spacing $\delta = 2$. The time derivative of the surface density reads

$$\dot{\Sigma}_m^i = -F_{i+1} + F_i \quad (8.135)$$

which assures the conservation of mass within numerical accuracy.

8.15 Integrator

All contributions to the evolution of the surface density Σ and the velocity dispersions T_r and T_z are summarised by the following set of differential equations:

$$D = \frac{4}{3\Omega^2} \left(\frac{5}{4} \dot{T}_{r,\text{enc}} + \dot{T}_{z,\text{enc}} \right) \quad (8.136)$$

$$\frac{d\Sigma}{dt} = \Delta_a(D\Sigma) + \dot{\Sigma}_{\text{coll}} \quad (8.137)$$

$$\frac{d\Sigma T_r}{dt} = \Delta_a(D\Sigma T_r) + \Sigma \dot{T}_r + \frac{d}{dt}(\Sigma T_r)_{\text{coll}} \quad (8.138)$$

$$\frac{d\Sigma T_z}{dt} = \Delta_a(D\Sigma T_z) + \Sigma \dot{T}_z + \frac{d}{dt}(\Sigma T_z)_{\text{coll}} \quad (8.139)$$

The Laplace operator is approximated in accordance with the equidistant radial grid:

$$\Delta_a f = \frac{1}{a} \frac{\partial}{\partial a} \left(a \frac{\partial}{\partial a} f \right) \quad (8.140)$$

$$\Delta_a f \approx \frac{f_{i+1}(1 + \Delta a/(2a_i)) - 2f_i + (1 - \Delta a/(2a_i))f_{i-1}}{(\Delta a)^2} \quad (8.141)$$

We chose the *Heun method*⁸ as the basic integrator for the statistical model. It is a second order accurate predictor–corrector scheme (X is a vector containing all the above quantities):

$$\frac{dX}{dt} = f(X) \quad (8.142)$$

$$X^p = X_n + \Delta t f(X_n) \quad (8.143)$$

$$X_{n+1} = X^p + \frac{1}{2} \Delta t (f(X^p) - f(X_n)) + \mathcal{O}(\Delta t^3) \quad (8.144)$$

The Heun method is readily extended to an iterate scheme, which is equivalent to the implicit expression:

$$X_{n+1} = X_n + \frac{1}{2} \Delta t (f(X_{n+1}) + f(X_n)) \quad (8.145)$$

This adds stability to the method and allows the secure integration of stiff configurations that may appear during the runaway accretion phase. In practice, three iterations are sufficient to guarantee a stable integration. As the diffusive part is discretised with a first order accurate formula (see Eq. 8.141), the whole iterated scheme is equivalent to the *Crank–Nicolson method*. We choose a global time step for the statistical model according to the expression

$$\Delta t = \min \left(\eta_{\text{Disc}} \frac{X}{\dot{X}}, X \in \{\Sigma, T_r, T_z\} \right) \quad (8.146)$$

where the hybrid code (see next Chapter) applies an additional discretisation in powers of two to achieve a better synchronisation with the N -body code component.

⁸The name of this method is not unique. Some texts denote it as the *modified Euler method*. The Heun method is a special case of the Runge–Kutta methods.

Chapter 9

Hybrid Code

9.1 Introduction

We introduced two different methods to solve the planetesimal growth problem. On the one hand, we modified NBODY6++, which has been used so far mainly for the simulation of stellar clusters, to adapt it to the special requirements of a long-term integration of planetesimal orbits. On the other hand, we developed a new statistical code with a consistent evolution of the velocity dispersion, the capability to treat spatial inhomogeneities and a thoroughly constructed collision treatment. Neither of the two approaches is powerful enough to provide a complete and accurate description of the planetesimal problem, since each method is confined to a certain range of the particle number. However, these restrictions are complementary in the sense that each method covers a regime where the other method fails. This intriguing relation stimulated the construction of a *hybrid code* which combines the benefits of both methods.

The basic idea is to introduce a transition mass m_{trans} , which separates the two mass regimes. Particles with a lower mass are treated by the statistical model, whereas larger particles belong to the N -body model. Though both parts are clearly divided in different mass ranges, they are connected by various interdependencies:

- Direct collisions between particles lead to a mass exchange. One process is the accretion of small particles by N -body particles, but agglomeration within the statistical model can also produce particles larger than the transition mass. This requires the generation of new N -body particles. Energetic impacts may erode larger particles, so a corresponding particle removal is also required for consistency.
- Mutual scatterings among N -body particles and smaller planetesimals transfer kinetic energy. While energy equipartition leads to a systematic heating of the smaller field planetesimals, a consistent treatment has to include both transfer directions.
- Accretion and scattering by the N -body particles induce spatial inhomogeneities or even gaps in the planetesimal component, if the particles have grown massive enough. Likewise, the small particles could induce some structure in the distribution of the N -body particles. Since the spatial structure is dominated by the stirring from few protoplanets, we neglect the latter process.

Fig. 9.1 summarises this brief overview of the interactions between the two code components in a schematic diagram. The following sections explain the implementation of each interaction term in more detail.

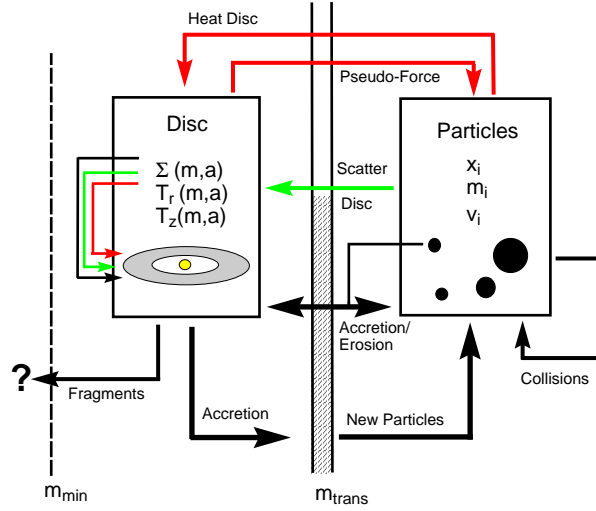


Figure 9.1: Interplay between the N -body component and the statistical component of the hybrid code. Black arrows indicate mass transfer, red arrows exchange of kinetic energy and green arrows indicate spatial structuring, respectively.

9.2 Mass Transfer

An N -body particle accretes smaller particles in its vicinity. We already derived expressions which describe agglomeration within the statistical model, so it is manifest to apply these formulas to derive the accretion rate of an N -body particle.

Most of the material is accreted within the cross-sectional area σ (see Eq. 8.105), but the finite eccentricity of an orbit extends the accessible radial *feeding zone*. Thus we assign the following surface density to each particle

$$\Sigma(a) = \frac{M}{2\pi a \sqrt{2\pi} l} \exp\left(-\frac{(a-a_0)^2}{2l^2}\right) \quad (9.1)$$

$$l^2 = \sigma/\pi + \frac{1}{2}a^2e^2 + T_r/\Omega^2 \quad (9.2)$$

by smearing it out over its feeding zone. T_r is the radial velocity dispersion of particles in the statistical model with semimajor axis a . This density distribution is projected onto the radial grid to calculate the accretion rate. As the time step of the statistical model is much larger than the regular step of an N -body particle, the particle mass update is synchronised with the statistical integration. The projection technique allows the calculation of the accretion rates in a simple way, which gives the right size of the feeding zone and the proper total accretion rate.

Particle generation is included in the following way: A ‘virtual’ mass bin is introduced as the boundary between the statistical grid (denoted by the dashed area in Fig. 9.1) and the N -body component. Its sole task is to store mass and kinetic energy that leaves the statistical model towards higher masses. If the mass content exceeds one m_{trans} , a new particle is created with inclination and eccentricity according to the stored velocity dispersions.

The masses of the N -body particles are regularly checked to detect any particle which dropped below the transition mass. While this procedure would remove the particle and transfer the associated quantities back to the grid, we never observed such a particle erosion.

9.3 Disc Excitation

The projection of an N -body particle onto the grid with the help of a proper weight function is also useful for the calculation of the disc excitation due to stirring by the larger particles. Since the Hill radius sets the proper length scale for planetesimal encounters, the weight function is modified to

$$\Sigma(a) = \frac{M}{2\pi a\sqrt{2\pi}l} \exp\left(-\frac{(a-a_0)^2}{2l^2}\right) \quad (9.3)$$

$$l^2 = R_{\text{Hill}}^2 + \frac{1}{2}a^2e^2 + T_r/\Omega^2 \quad (9.4)$$

where T_r is the radial velocity dispersion of the heated planetesimal component. The velocity dispersion of the stirring N -body particle is (in accordance with Eq. 3.20 and Eq. 3.21):

$$T_{r,0} = \frac{1}{2}(\Omega a_0)^2 e^2 \quad (9.5)$$

$$T_{z,0} = \frac{1}{2}(\Omega a_0)^2 i^2 \quad (9.6)$$

We employ the orbital elements as mediators between the fast varying instantaneous position and velocity of a particle and the slow evolution of the statistical model, which operates on a longer relaxation timescale. In virtue of the projection of the particle, we readily apply the standard interaction terms (see Chapter 8) to evaluate the additional heating due to the presence of N -body particles.

9.4 Pseudo-Force

While an N -body particle is moving through the disc, it also interacts gravitationally with the particles in the statistical model. The collective effect of all these encounters leads to a change in the orbital elements of the N -body particle. Again, we project the N -body particle onto the grid and evaluate the stirring rates \dot{T}_r and \dot{T}_z , which correspond to a change in the orbital elements:

$$\frac{d}{dt}e^2 = \frac{2\dot{T}_r}{(\Omega a_0)^2} \quad (9.7)$$

$$\frac{d}{dt}i^2 = \frac{2\dot{T}_z}{(\Omega a_0)^2} \quad (9.8)$$

These time derivatives of eccentricity and inclination are translated to a pseudo-force, that effects the desired change of the orbital elements. We chose the ansatz

$$\mathbf{F}_{x,y} = C_r(\mathbf{v}_{x,y} - (\mathbf{v}_K)_{x,y}) \quad (9.9)$$

$$\mathbf{F}_z = C_z\mathbf{v}_z \quad (9.10)$$

where \mathbf{v}_K is the local Keplerian velocity. In addition, we tried a simpler expression

$$\mathbf{F}_{x,y} = 2C_r\mathbf{r}_{x,y} \frac{\mathbf{r} \cdot \mathbf{v}}{r^2} \quad (9.11)$$

$$\mathbf{F}_z = C_z\mathbf{v}_z \quad (9.12)$$

without any significant differences in the accuracy or the simulation outcome. The proper friction coefficients are:

$$C_r = \frac{\dot{T}_r}{2T_r} \quad (9.13)$$

$$C_z = \frac{\dot{T}_z}{2T_z} \quad (9.14)$$

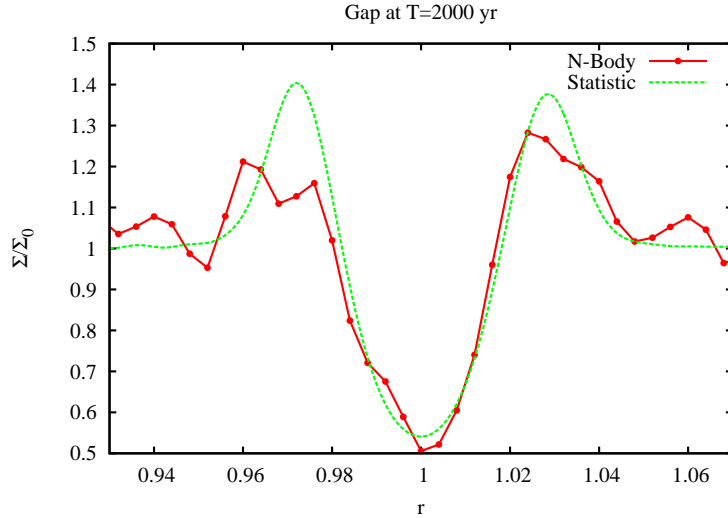


Figure 9.2: Gap opening in a planetesimal disc. The gap is fully developed after 2000 years. Table 9.1 summarises the initial conditions for the comparative runs.

No	Σ	Δa	N	N_{rad}	e^2/h^2	i^2/h^2	m	Type
G1	1.1251×10^{-6}	0.2	1406	—	0.00135	0.00135	1×10^{-9}	N -body
	Perturber	—	1	—	$e = 6.1 \times 10^{-5}$	$i = 3.2 \times 10^{-5}$	1×10^{-7}	
G2	1.1251×10^{-6}	0.2	—	201	0.00135	0.00135	1×10^{-9}	Statistic
	Perturber	—	1	—	$e = 6.1 \times 10^{-5}$	$i = 3.2 \times 10^{-5}$	1×10^{-7}	

Table 9.1: Parameters of the statistical and the N -body gap simulation. The perturber is placed at the centre of the ring.

Since the relevant quantities are the time derivatives of the orbital elements, any other pseudo-force is also applicable. Though this approach yields the right mean change of the orbital elements, it lacks the statistical fluctuations from the particle disc. Hence the distribution of the orbital elements of the N -body particles is artificially narrowed, which is especially important when the N -body particles and the statistical particles have a comparable mass. As the mass contrast between the two code parts is quite significant in planet formation simulations, it is safe to neglect the fluctuating part without major restrictions on the realism of the simulations.

The friction coefficients C_i are kept constant between two integration steps of the statistical model. While a more frequent update of the coefficients would be easily possible, a regular update on the basis of the statistical time step is accurate enough. Moreover, each update poses a considerable computational effort (roughly equivalent to 1000 force evaluations), so our approach also saves valuable computational time.

9.5 Spatial Structure

The first insight into planetesimal formation was obtained by the particle-in-a-box method, which invokes the underlying assumption that the planetesimal disc stays homogeneous throughout the protoplanet growth (see e. g. Greenberg et al. 1978 [47]). While few large bodies introduce some coarse-graininess of the surface density, all smaller bodies are assumed to be evenly spread in the disc. Research on the interaction of protoplanets showed that this is an oversimplification, as bodies that are massive enough could open gaps in their vicinity (see e. g. Lin and Papaloizu 1979 [95], Rafikov 2001 [125]). Gap formation does not only change the overall surface density, but also controls the accretion onto the protoplanet through the amount of planetesimals in the

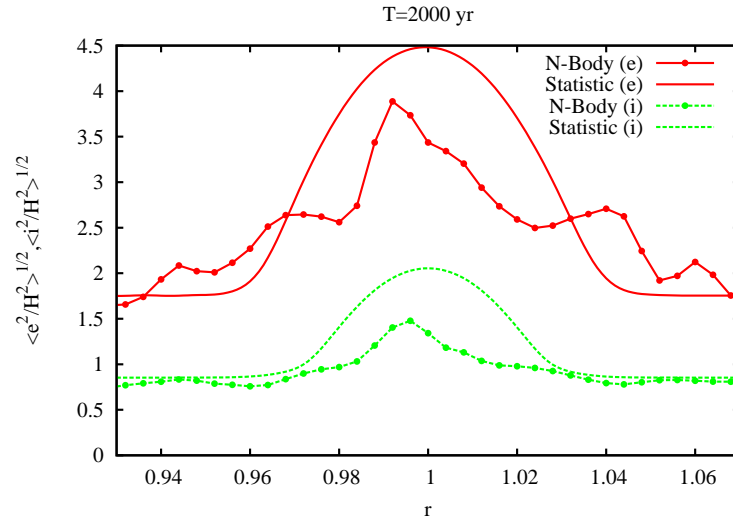


Figure 9.3: Mean square eccentricity and inclination of the smaller planetesimals in terms of the reduced Hill radius H of the protoplanet according to simulation G1 (N -body) and G2 (Statistic).

feeding zone. If gap formation is too effective, the growth of the protoplanet may well stop before the isolation mass is reached. Hence any hybrid code should provide a framework that allows this mechanism to operate. A necessary condition is a radial density grid with a sufficient resolution to describe possibly emerging gaps. A too low resolution suppresses local perturbations from the protoplanets by a simple averaging, thus inhibiting the formation of any spatial inhomogeneities. A second requirement is, that the interaction terms relating statistical model and N -body model include the local interaction between particles and the statistical component in a proper way. Our hybrid approach includes gap formation implicitly through the diffusive terms. A protoplanet heats only the planetesimals in its vicinity (defined by the heating kernel), thus also increasing locally the diffusion coefficient. Hence the surface density drops due to outward diffusion of the planetesimals, given that the protoplanet is massive enough. The minimum gap opening mass is set by the condition, that the protoplanet controls the random velocities of the field planetesimals in its heating zone (see Eq. 3.49), which is equivalent to the independently derived gap formation criterion (compare Eq. 3.51).

Although our algorithm invokes a simplified picture of the protoplanet–planetesimal interaction, it is surprisingly accurate with respect to the width of the forming gap and the opening criterion. Fig. 9.2 shows a simulation which examines the accuracy of our approach. The overall performance of the statistical code is quite remarkable, except a significant overestimation of the surface density at the gap boundary compared to the N -body model. This deviation is due to the improper treatment of strong planetesimal–protoplanet encounters, which exceed the diffusive approximation. Moreover, the higher concentration of planetesimals near the gap boundary leads to an additional overestimation of the velocity dispersion of the smaller planetesimals in the statistical calculation (see Fig. 9.3). While the comparison with the N -body calculation clearly indicates a necessary improvement of the treatment of spatial inhomogeneities, our approach catches the main features of gap formation.

9.6 Transition Mass

Since the inventory of the new hybrid code is now completed, we turn to the specification of the transition mass m_{trans} . The mass boundary between statistical and N -body part has a major influence on the realism and the speed of the simulation. On the one hand, optimisation with

respect to speed favours a large transition mass, whereas a reasonable resolution of the transition between the two components introduces some upper limit.

Hence we identify first the set of large masses, which controls the velocity dispersion of the disc, since these objects are also possible candidates for gap opening. The inspection of all involved stirring terms gives approximately the inequality:

$$\int_0^{m_{\text{trans}}} \frac{d\Sigma}{dm} m dm < \int_{m_{\text{trans}}}^{\infty} \frac{d\Sigma}{dm} m dm \quad (9.15)$$

While this is a necessary condition to select all potential major perturbers, criterion 9.15 does not imply that all particles in the selected mass range exert indeed a strong influence on the disc. The number of possible gaps – and therefore the number of perturbers associated with them – is ultimately limited by the available space. Thus we integrate the area of all potential gaps (width $\approx f_{\Delta} R_{\text{Hill}}$) and normalise it to the total disc area:

$$f_C \approx \int_{m_{\text{trans}}}^{\infty} f_{\Delta} \frac{d\Sigma}{dm} \frac{2\pi a R_{\text{Hill}}}{m} dm \quad (9.16)$$

If the covered fraction f_C is much larger than one, it is possible to increase the transition mass until the condition

$$f_C \lesssim 1 \quad (9.17)$$

is fulfilled. Of course, condition 9.15 and 9.17 defined only an upper limit of the transition mass, so the adaptation of a lower value is also possible. Though there are two reliable conditions at hand, the transition mass is still a function of time owing to the time evolution of the density $\Sigma(m)$. Therefore we chose *a priori* a fiducial value of the transition mass, run the simulation and conduct an *a posteriori* check, whether the initial choice matches our requirements at any evolutionary stage of the disc. A reliable value for a solar system analogue at 1 AU is

$$m_{\text{trans}} \approx 3 \times 10^{-11} M_{\odot} \quad (9.18)$$

which restricts the number of N -body particles to a tractable amount. Later stages would allow an even larger transition mass, but the current hybrid code does not include any dynamical adjustment of the transition mass at runtime.

9.7 Boundary Conditions

Any numerical simulation is limited to a finite simulation volume and a finite time interval. Therefore it is mandatory to introduce proper *boundary conditions* which provide a reasonable closure of the simulation volume.

While boundary conditions with respect to time are the familiar *initial conditions*, the choice of the spatial boundary conditions for the various involved quantities depends on the problem at hand and the type of the boundary. A simulation boundary can be due to physical reasons (like walls of a concert hall, surface of a terrestrial planet) or simply due to a limitation in computational power that inhibits the complete numerical coverage of the problem.

The current capability of the hybrid code sets limits on the radial range as well as on the covered mass range, which a simulation can handle in a reasonable time. Hence we have to introduce artificial boundaries in radius, and a lower limit for the mass grid.

Any migration process couples the evolution of a local ring area in the planetesimal disc to the evolution of the whole disc. Inward (or outward) migrating material also transports information on the radial zone where the material originated from. As this information is not available within the frame of a local simulation, any choice of the boundary condition alters the evolution to some extent.

However, we focus on a formation stage where migration is not a dominant process, but provides only removal of the smaller collisional fragments. Thus we apply closed boundary conditions for

No.	Σ	Δa	N	N_{rad}	e^2/h^2	i^2/h^2	m	Type
T1a	1.1251×10^{-6}	0.02	1000	–	0.04	0.01	1.41×10^{-10}	N -body
T1b	1.1251×10^{-6}	0.02	500	10	0.04	0.01	1.41×10^{-10}	Hybrid
T1c	1.1251×10^{-6}	0.02	–	10	0.04	0.01	1.41×10^{-10}	Statistic
T2a	0.5626×10^{-6}	0.08	800	–	4	1	5×10^{-10}	N -body
	0.5626×10^{-6}		200	–	4	1	2×10^{-9}	
T2b	0.5626×10^{-6}	0.08	–	10	4	1	5×10^{-10}	Hybrid
	0.5626×10^{-6}		200	–	4	1	2×10^{-9}	
T3	Safronov	–	–	–	–	–	–	Statistic
T4a	1.1251×10^{-6}	0.02	10.000	–	4	1	1.41×10^{-11}	N -body
T4b	1.1251×10^{-6}	0.02	–	10	4	1	1.41×10^{-11}	Hybrid
T4c	1.1251×10^{-6}	0.02	–	10	4	1	1.41×10^{-11}	Statistic
T5	1.8789×10^{-6}	–	–	–	620	155	2.4×10^{-15}	Statistic

Table 9.2: Parameters of all test simulations. The transition mass in T4b is $m_{\text{trans}} = 3.1 \times 10^{-10}$. Only simulations T3, T4a–T4c and T5 include collisions. All values are scaled to $M_c = G = r_0 = 1$.

the outer and inner radius of the ring area (i.e. all fluxes vanish at the boundary), and an open boundary for the lower end of the mass range. While these conditions exclude the study of migrational processes, we gain clearer insight into the protoplanet growth.

9.8 Validating the Code

The new hybrid code is a complex system, which required the implementation of rather different methods and the integration of all these components into one code frame. Though such a project is already susceptible to implementation errors, the method itself is new and requires thus a careful assessment of the reliability.

We conducted a variety of test simulations to check all code components, namely the evolution of the velocity dispersion, the accuracy of the coagulation equation solver, the proper joining of statistical and N -body component and an overall comparison of statistical, N -body and hybrid calculations. Table 9.2 summarises the selected test runs with the respective initial conditions.

9.8.1 Energy Balance

The first test run is dedicated to a careful check of the interplay between statistical component and N -body component with respect to the evolution of the velocity dispersion. Collisions and accretion are thus excluded.

We use a homogenous ring of planetesimals as a test case. Since this problem is accessible to a pure statistical calculation, it is possible to compare three different setups – a pure N -body calculation, a pure statistical calculation and a mixed hybrid calculation. All three approaches should reproduce the same result. Hence we prepared a small N -body test run (T1a) and let the system evolve (see Fig. 9.4). As a second test run, we shifted one half of the bodies to the statistical model and conducted the integration again (T1b). While this usage of the hybrid code is somewhat artificial, it provides an excellent setup to examine the interplay between N -body and statistical part, since neither component dominates the result. Finally, we run a complete statistical calculation (T1c).

All different approaches are in excellent agreement. Though the accordance between N -body and statistical calculation is not a new finding – it merely shows that the stirring terms provide a proper description of a planetesimal system (this was already shown by Ohtsuki et al. 2002 [116]) – the agreement demonstrates that the integration accuracy of the statistical model is well adjusted. A more stringent test is posed by the hybrid run, which proves that the pseudo-force

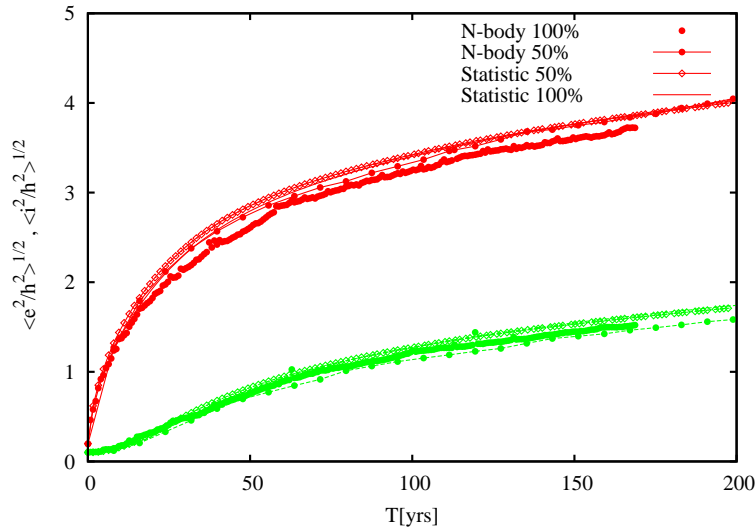


Figure 9.4: Test simulations T1a–T1c (uniform mass). Plotted are the results from the N -body calculation (100 % N -body), the statistical calculation (100 % Statistic) and the hybrid calculation (50 % Statistic refers to the statistical component, whereas 50% N -body is the N -body part). Eccentricity data is coloured red, whereas inclination data is coloured green. See text for details.

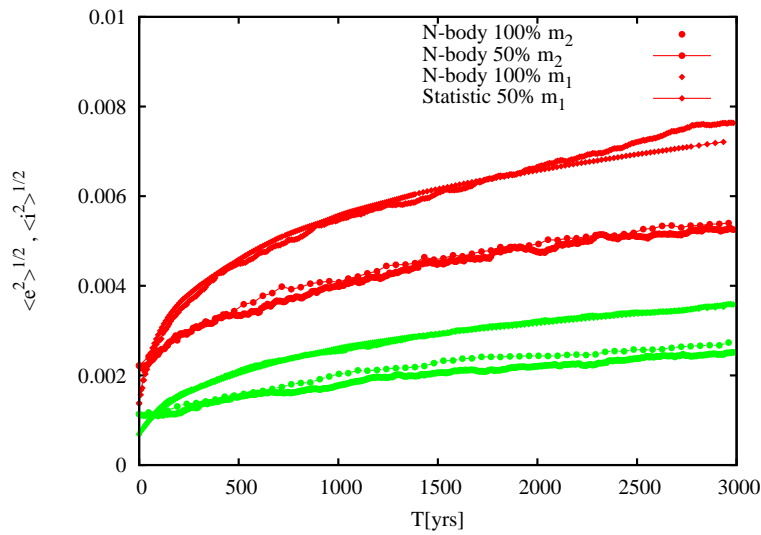


Figure 9.5: Comparison of the N -body calculation T2a with the hybrid calculation T2b. The coding is the same as in Fig. 9.4.

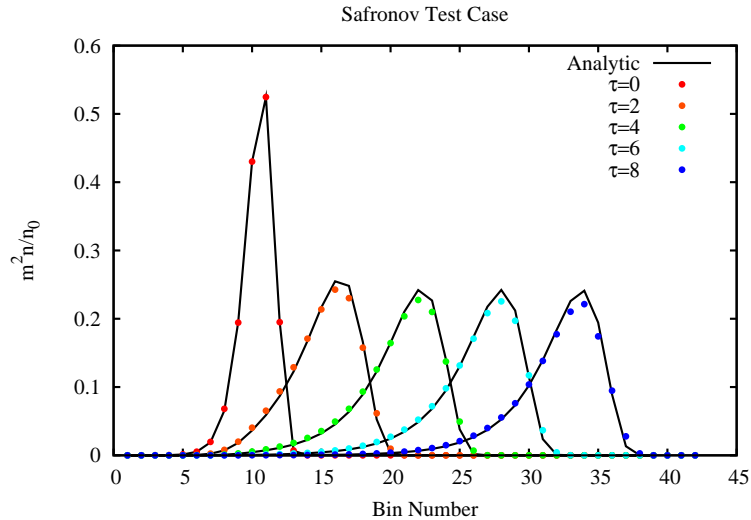


Figure 9.6: Testing the solution of the coagulation equation (T3). The analytical solution is given by Eq. 7.70.

method links both code components in a consistent way without spurious energy transfer. Fig. 9.4 includes both components of the hybrid calculation separately, but the difference is so small that they are hardly distinguishable.

A second set of test runs adopts the same approach, but employs a bimodal mass distribution, where the total mass in both components is equal. The first simulation is a pure N -body calculation (T2a), whereas the second simulation handles the smaller particles with the statistical model. This test is closer to the ‘true’ application of the hybrid code, and Fig. 9.5 shows a satisfactory agreement of the two test runs. Moreover, the hybrid calculation is also superior to the full statistical calculation, which is omitted in Fig. 9.5 for clarity.

9.8.2 Coagulation Equation

We verified the improved numerical solution of the coagulation equation by a comparison with the analytic solution Eq. 7.70 of the Safronov problem. The collisional cross section is assumed to be proportional to the sum of the masses of the colliding bodies. Thus the coagulation kernel is known and an additional integration of the velocity dispersions is not necessary. Fig. 9.6 summarises the numerical solution (T3) of the Safronov test case. The mass bins are spaced by a factor $\delta = 2$. While some slight differences emerge near the maximum of the density distribution, the overall shape is well conserved throughout the integration. This proves that a spacing with a factor two still guarantees a reliable solution of the coagulation equation without a modified growth timescale. However, the Safronov test also indicates that a spacing larger than two is probably too inaccurate.

9.8.3 Complete Code Test

The most stringent test of our hybrid code (or the stand-alone statistical code) would be a comparison with a pure N -body simulation with the same initial setup. While a large particle number is desirable to cover a large range in masses, limits in the hardware speed restrict the particle number for direct N -body techniques to a few 10^4 . Hence we chose a single-mass system with initially 10,000 particles. Planetesimal radii are enhanced by a factor $f = 5$, which speeds up the calculation without modifying the growth mode. The transition mass is twenty times larger than the initial planetesimal mass, keeping the particle number covered by the statistical component

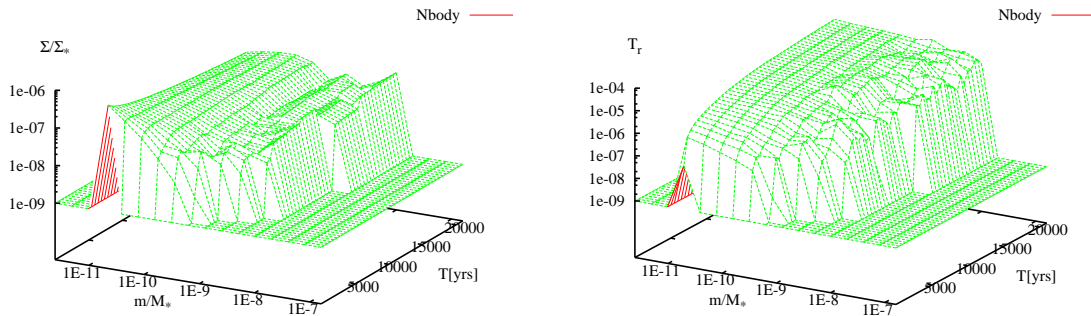


Figure 9.7: Surface density and radial velocity dispersion of the N -body model (T4a).

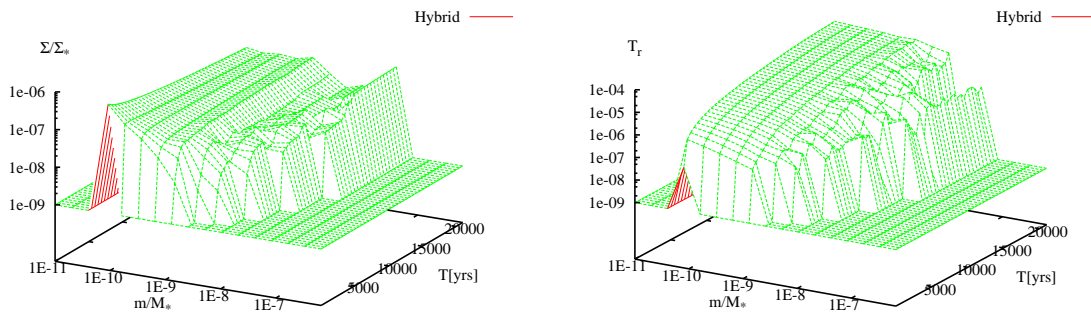


Figure 9.8: Surface density and radial velocity dispersion of the hybrid model (T4b).

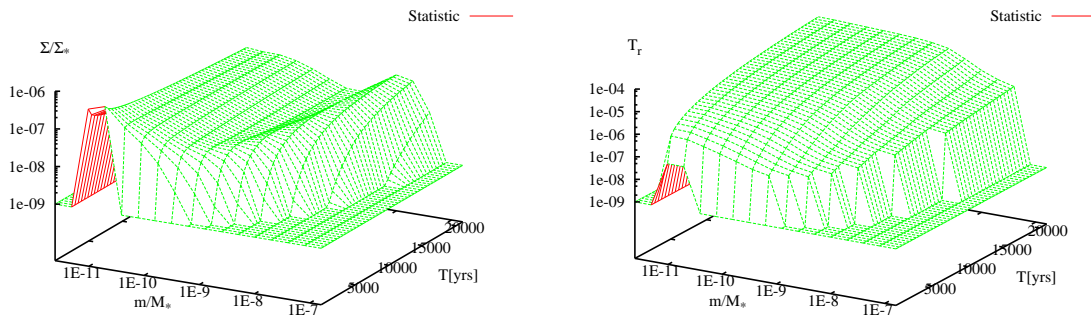


Figure 9.9: Surface density and radial velocity dispersion of the statistical model (T4c).

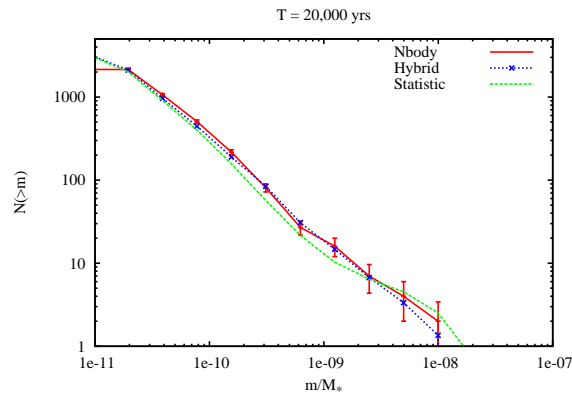


Figure 9.10: Cumulative size distribution of the comparative runs T4a–T4c at $T=20,000$ yr.

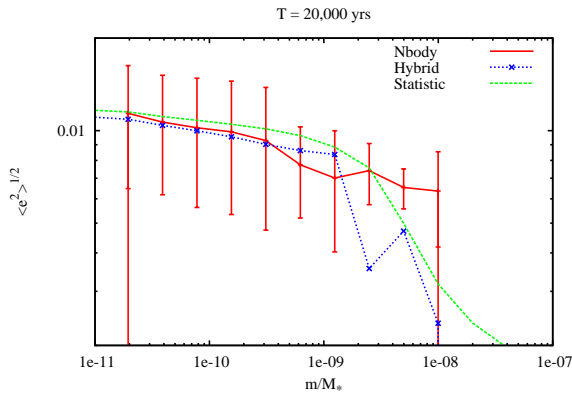


Figure 9.11: Mean square eccentricities of the comparative runs T4a–T4c at $T=20,000$ yr. Error bars indicate the spread due to the rayleigh distribution of the eccentricity.

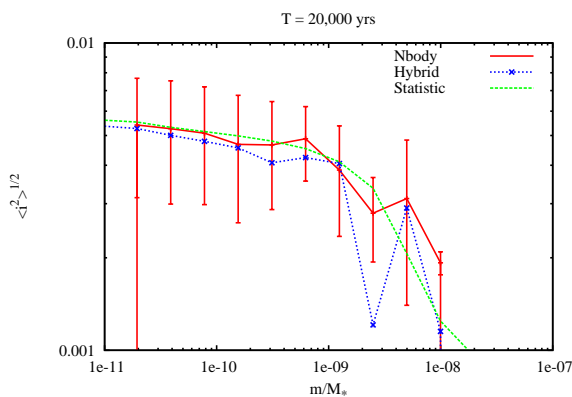


Figure 9.12: The same as Fig. 9.11 for the inclination. The strong deviation at $m = 3 \times 10^{-9}$ is due to a single particle.

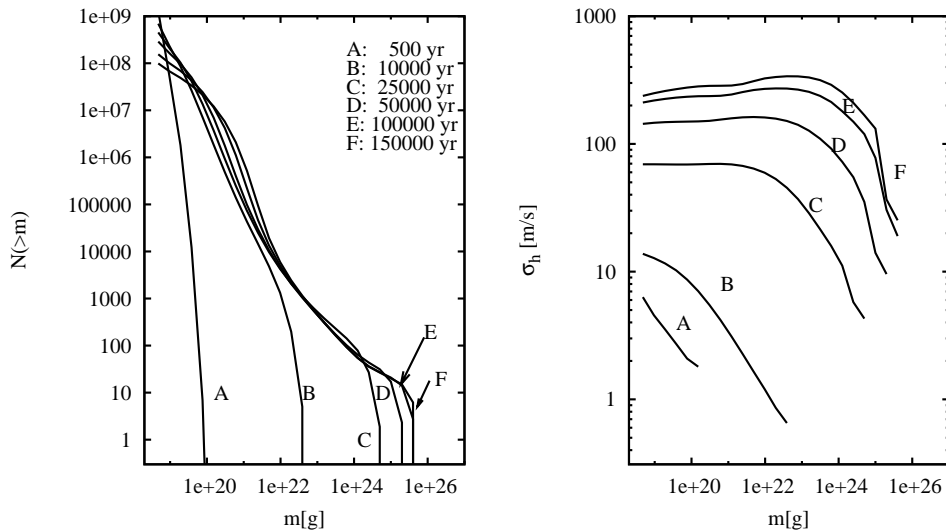


Figure 9.13: Comparative calculation T5 which adopts the initial conditions of Inaba et al. 2001 (their Fig. 9, bottom).

larger than a few thousands. We compare a full N -body run with a hybrid calculation and a pure statistical calculation. Though the stand-alone statistical calculation includes the proper treatment of the runaway bodies via the gravitational range method, no further precaution like the suppression of self-accretion and self-stirring is taken if only few particles reside in one mass bin. While the hybrid approach describes this regime in much more detail, we included the full statistical calculation nevertheless for completeness.

Fig. 9.7–9.9 give an overview of the time evolution of the system, where all quantities are integrated over the whole system. All calculations seem to agree rather well, although the statistical noise in the N -body calculation and the hybrid calculation is quite strong. Runaway growth leads to the fast formation of a few protoplanets on a timescale of a few thousand years, with a good agreement of the fast initial growth phase in the three test runs. The boundary between smooth evolution and noisy data marks the location of the transition mass in the hybrid calculation.

We compare the size distribution and the velocity dispersion at the end of the integration (20,000 yr) in more detail in Fig. 9.10–9.12. Both the N -body data and the hybrid data are projected onto the same grid as the full statistical calculation to allow a convenient comparison.

The agreement of the size distribution $N(> m)$ is excellent, as the small deviations are within the statistical error. While the strong variations in the size distributions in Fig. 9.7–9.9 seem to contradict this finding, these deviations are located at the high mass end, where only few particles dominate the surface density. In addition, the growth in the statistical model seems to be faster than the N -body reference calculation. However, the density at the highest masses refers to less than one particle. This unphysical result is due to the already mentioned poor treatment of the few-body limit.

The comparison of the velocity dispersions is also satisfactory, especially in the low-mass regime, where the statistical error is small. The high mass regime does not only suffer from bad statistics, but also from a pronounced time variability (compare the fluctuations in Fig. 9.7–9.9). Taking these variations into account, all three calculations agree satisfactory (the deviation at $m = 3 \times 10^{-9}$ is due to a single particle).

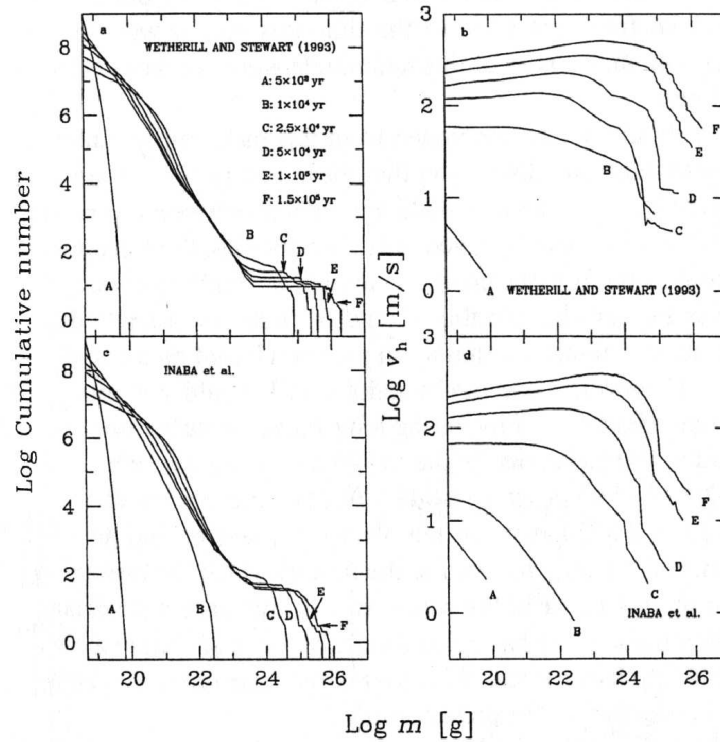


Figure 9.14: Calculation of Inaba et al. 2001 [67] (their Fig. 9, bottom).

9.8.4 Statistical Code

Our last test calculation is a comparison to the work of Inaba et al. 2001 [67] (their Fig. 9, bottom), who put considerable effort in the construction of a high accuracy statistical code. They include nearly the same physics and interpolation formula, with minor differences to our approach. While our approach allows a spacing $\delta = 2$, their solution of the coagulation requires a smaller spacing $\delta = 1.1$ to guarantee a reliable solution. The few-body limit is handled properly, with an additional treatment of the protoplanets via the gravitational-range approach.

We chose initial conditions (T5), which match the values of Inaba et al. 2001 [67]. Again, we find a good agreement (see Fig. 9.13 and Fig. 9.14) except minor deviations that are due to the different implementation of the collisional probability.

Chapter 10

Results

10.1 Initial Conditions

We apply our hybrid code to a well defined initial setup of a planetesimal disc. All simulations use a homogenous ring of planetesimals extending from an inner boundary R_{\min} to an outer boundary R_{\max} . Since radial migration is not included, all planetesimals are bounded to this volume throughout the simulation. The central star has a mass of one solar mass. Each simulation starts with no N -body particles, thus we need only to specify the setup for the statistical part of the calculation. The differential surface density as a function of mass is

$$\frac{d\Sigma}{dm} = \Sigma_0 \frac{m}{\bar{m}^2} \exp(-m/\bar{m}) \quad (10.1)$$

$$\text{Var}(m) = \bar{m}^2 \quad (10.2)$$

where Σ_0 is the total surface density and \bar{m} is the mean mass. Eq. 10.1 provides a smooth variation over a few mass bins, which avoids numerical problems at startup. The initial velocity dispersion is related to the mean escape velocity v_∞ of the initial size distribution defined by Eq. 10.1

$$\frac{1}{100} v_\infty^2 = T_r + T_\phi + T_z \quad (10.3)$$

with the ratio of the velocity dispersions

$$T_r = 4T_\phi = 4T_z \quad (10.4)$$

We adopt a rather small initial velocity dispersion to avoid strong spurious fragmentation due to an overestimated velocity dispersion. Furthermore, strong relaxation in the initial phase of the calculation establishes quickly an equilibrium velocity dispersion. The time step control parameters are chosen such that the energy error $\Delta E/E$ of the N -body component remains always smaller than 10^{-8} throughout the simulation. Likewise, our choice of the parameters of the statistical component assures that the statistical model is solved accurately and remains stable, as indicated by the set of comparative runs. All runs simulate only a narrow ring centred at a distance r_c . Hence we employ the following scaling:

$$r_c = 1 \quad M_c = 1 \quad G = 1 \quad (10.5)$$

Appendix A contains a complete set of scaling constants to provide a convenient transformation between physical units and simulation units (defined by Eq. 10.5) if needed. Table 10.1 summarises the main simulation parameters.

η_{Disc}	0.01
η_{reg}	0.002
η_{irr}	0.001
R_{min}	0.95 AU
R_{max}	1.05 AU
\bar{m}	3×10^{18} g
ρ	2.7 g/cm ³
δ	2
Δv_g	60 m/s

Table 10.1: General parameters common to all simulations listed in table 10.2.

Code	Strength	N_M	N_R	$\Sigma[\text{g}/\text{cm}^2]$	m_{min}/M_c	m_{trans}/M_c	$\rho_g[\text{g}/\text{cm}^3]$
S1FB	B&A 1999	24	50	10	3.48×10^{-18}	3.89×10^{-11}	10^{-9}
S2FH	H&H 1990	24	50	10	3.48×10^{-18}	3.89×10^{-11}	10^{-9}
S3FN	Perfect Merger	24	50	10	3.48×10^{-18}	3.89×10^{-11}	10^{-9}
S4FBN	B&A 1999	24	50	10	3.48×10^{-18}	3.89×10^{-11}	0
S5FBL	B&A 1999	24	5	10	3.48×10^{-18}	3.89×10^{-11}	10^{-9}
S6FBH	B&A 1999	24	100	10	3.48×10^{-18}	3.89×10^{-11}	10^{-9}
S7FB2	B&A 1999	40	50	10	5.31×10^{-23}	3.89×10^{-11}	10^{-9}
S8_S2	B&A 1999	15	50	2	3.48×10^{-18}	4.87×10^{-12}	2×10^{-10}
S9_S100	B&A 1999	27	50	100	3.48×10^{-18}	3.11×10^{-10}	10^{-8}

Table 10.2: Complete list of all simulations. The first group examines different collisional models, the second group resumes the nominal simulation S1FB with different resolutions and the third group explores different surface densities.

10.2 Simulations

Though the hybrid code has been constructed to solve the complete (with respect to size) planetesimal problem, our approach is still limited by the available computing resources. A small ring with a width of 0.1 AU (centred at 1 AU) and a moderate lower cut-off size needs already one week of wallclock time, where the major fraction is due to the statistical model. Hence we focussed on this rather small setup as a reference model, but we also conducted some more refined models with calculation times up to months.

As we apply our hybrid code to planet formation for the first time, we use a nominal surface density $\Sigma = 10 \text{ g}/\text{cm}^2$, which assures a convenient comparison to other works since it serves as a common reference value in the literature. We focus on the following aspects of protoplanetary growth:

1. Different collision models
2. Spatial (radial) density structure (e. g. gap formation)
3. Resolution effects
4. Different surface densities

The first item represents a fundamental uncertainty, since the impact physics of planetesimals is still under active research. Realistic simulations of planetesimal collisions do not only require a carefully constructed code, but also a knowledge of the internal structure of the involved bodies. Since planetesimals emerge as fragile dust aggregates and evolve into solid bodies, their internal structure and strength is also time-dependent. The second item highlights the slowly

No.	A	B	C	D	E	F
$T[\text{yr}]$	0	1,000	10,000	20,000	50,000	100,000

Table 10.3: Time coding of the evolutionary stages A to F .

evolving inhomogeneities introduced by the growing protoplanets. It was argued that gap opening in the planetesimal disc could stop the accretion well before the isolation mass is reached (see Rafikov 2001 [125]). As the hybrid code includes spatial structuring in a proper way, it is possible to ascertain the role of gap formation in the protoplanetary growth process. The third issue is less subjected to unknown physics, but rather to limitations in the available computing power. As the solution of the coagulation equation scales with the third power of the number of grid cells, the choice of a realistic cut-off mass may be prohibitively expensive. To conclude our investigation, we conducted a small set of different surface densities with our reference fragmentation model (Benz and Asphaugh 1999 impact strength, referred to as B&A 1999 hereafter). Table 10.2 summarises the various parameters of our simulations, while the following sections discuss each simulation in more detail. Since the hybrid code uses a statistical representation and N -body data at the same time to integrate a planetesimal disc, we employ the following technique to provide a concise data analysis:

The N -body data is projected onto an extended mass grid derived from the statistical model to generate a unified representation of a hybrid run. Additional diagrams supplement more information on the N -body component if needed.

10.2.1 Fragmentation Models

The treatment of collisions is a key element in any planetesimal growth simulation. While the basic parameters of collisions are rather well understood, the current status of research leaves still room to explore different collisional models. We devised four different setups to examine the influence of the collisional model in more detail. The perfect merger assumption (S3FN) is our most basic choice. While this is an inappropriate assumption for mutual collisions among smaller planetesimals, it provides an upper limit for the growth speed. The second and third model use our detailed collisional model (see Chapter 6) with the B&A 1999 impact strength (S1FB) and the Housen and Holsapple 1990 (referred to as H&H 1990 hereafter) impact strength (S2FH). These two impact strengths are not the only derived strength measures (see e.g. the broad overview in Benz and Asphaug 1999), but they mark roughly the range of possible values. The fourth model (S4FBN) assumes a gas-free system due to an early dispersal of the gaseous disc. This model does not represent an alternative collision model, but provides a different evolution of the random velocities, which gives rise to a different role of collisions. All other simulations neglect the dispersal of the gaseous disc, since the simulation time is still short compared to the disc lifetime. Each simulation is summarised in a set of four diagrams (see Fig. 10.4–10.7):

A summary of the cumulative size distribution $N(> m)$ (upper left), which displays at what sizes most of the particles are located. In addition, we provide the surface density per bin Σ_Δ (upper right) to indicate where most of the mass is concentrated. Owing to the logarithmically equal spacing of the mass grid, Σ_Δ is related to the differential surface density

$$\Sigma_\Delta \approx \frac{2}{3} \frac{\partial \Sigma}{\partial \ln(m)} \quad (10.6)$$

where $\delta = 2$ is assumed. The summary is completed by two plots of the radial (T_r) and vertical (T_z) velocity dispersion (lower left and right).

Despite of the quite different setups, we notice an overall similarity of the time evolution. Runaway growth sets in after a few 10^4 years (stage C), indicated by the formation of a pronounced peak at the high mass end. The onset of runaway growth roughly coincides with the creation of the first N -body particles. Opposed to earlier statistical calculations (e.g. Wetherill and Stewart

1989 [150], 1993 [151]), we find no ‘gap’ in the size distribution, but a smooth transition from the slowly growing field planetesimals (peak around 10^{19} g) to the rapidly growing protoplanets. The initiation of runaway growth is associated with a qualitative change in the velocity dispersion. While the initial choice of the velocity dispersion quickly relaxes to a constant value at smaller sizes (transition stage A→B), dynamical friction establishes energy equipartition among the larger masses. The turnover point between these two regimes refers to a balance between the stirring due to larger bodies and damping due to encounters with smaller planetesimals (Rafikov 2003d [129]). In addition, the smaller planetesimals are subjected to damping by the gaseous disc, which significantly reduces the velocity dispersion at smaller sizes. Hence this damping is absent in the gas-free case (compare S4FBN, Fig. 10.7 bottom).

We emphasise that all simulations do not generate any artifacts which could be attributed to an improper joining of the statistical and the N -body component. Some non-smooth structure is visible at the high mass end (i. e. data from the N -body component), but the variations do not exceed the fluctuations expected from small number statistics.

All simulations which allow destructive collisions exhibit the evolution of a fragment tail. The expected equilibrium slope is roughly $k \approx 2$ (compare Chapter 7), which refers to a steep size distribution and a rather flat density distribution:

$$N(> m) \propto m^{-1} \quad (10.7)$$

$$\Sigma_{\Delta} \approx \text{const.} \quad (10.8)$$

Simulation S1FB (B&A 1999 strength, Fig. 10.6) and S4FBN (Gas-free, Fig. 10.7) show a clear plateau in the density distribution, in accordance with estimate Eq. 10.8. In contrast, simulation S2FH (H&H 1990 strength, Fig. 10.5) evolves a second maximum at the lower boundary of the mass grid. Though this structure is partly due to the lower grid boundary, the main cause is the reduced H&H 1990 impact strength at sizes of a few 10 kilometres (as compared to the B&A 1999 strength), thus leading to the quick destruction of the remaining field planetesimals at masses around 10^{18} g.

The overall agreement of the different simulations is reflected by the growth of the largest mass in the system (see Fig. 10.1). Until 2×10^4 years, all simulations agree rather well. Later on simulation S3FN (Perfect Mergers) exhibits the largest growth rate as expected. Though simulation S1FB (B&A 1999 strength) seems to show a slower growth than simulation S2FH (H&H 1990 strength), this is only due to a different sequence of major impacts. In fact, the B&A 1999 strength simulation allows for a much faster growth, in accordance with the total mass contained in the N -body component (Fig. 10.3). The gas-free simulation S4FBN exhibits the slowest growth among the four test cases.

A further examination of the mass loss¹ reveals the cause of this different behaviour. A pronounced mass loss in simulation S2FH slows the protoplanetary growth down by an overall reduction of the surface density. On the contrary, the accretion rate in the gas-free case is mainly reduced by a larger velocity dispersion (compare Fig. 10.7 bottom to Fig. 10.6 bottom), though some increased mass loss (compared to S1FB) is visible.

We find no accelerated growth due to the inclusion of fragmentation events, compared to Wetherill and Stewart 1989 [150]. In contrast, we find that a lower impact strength or the absence of gas damping slows down the growth by an increased mass loss. The total mass in the N -body component is still small ($\approx 10\%$ of the total mass, compare Table 10.4) at the end of the simulations, thus orbit crossing is expected to set in after a few 10^6 years.

10.2.2 Spatial Distribution

The capability of the code to treat spatial inhomogeneities relies on the chosen spatial resolution. Thus we compare a low resolution model (S5FBL), which virtually inhibits any spatial structuring, with a model using our nominal resolution (S1FB) and a run with even improved resolution

¹Mass loss refers to planetesimals which pass the lower grid boundary.

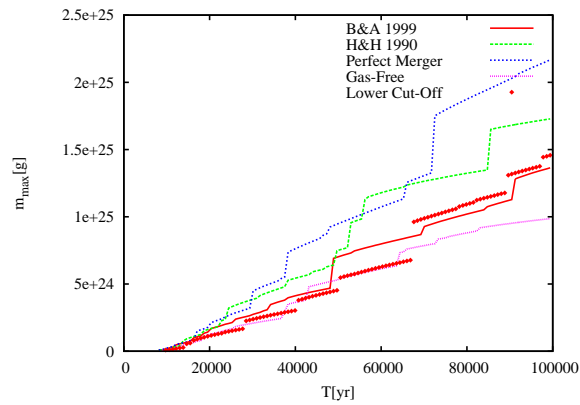


Figure 10.1: Largest body in the simulation as a function of time for the different collision models S1FB (B&A 1999), S2FH (H&H 1990), S3FN (Perfect Merger) and S4FBN (Gas-Free). In addition, simulation S7FB2 with a lower cut-off mass is included.

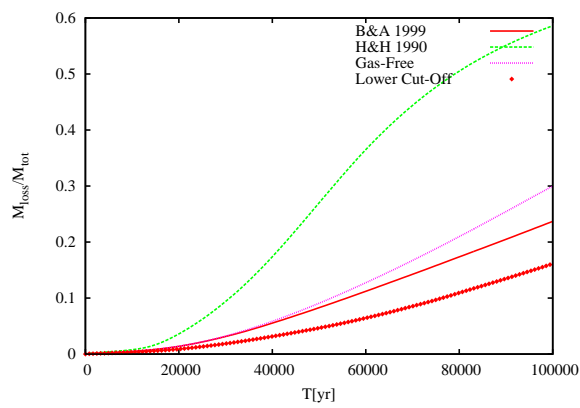


Figure 10.2: The same coding as Fig. 10.1 for the total mass loss. Hence S3FN (Perfect Merger) is not included.

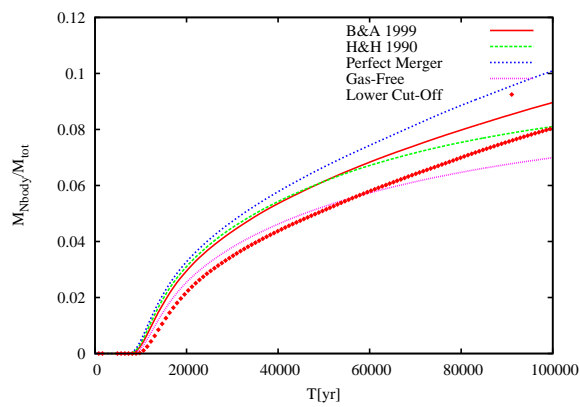


Figure 10.3: The same as Fig. 10.1 for the total mass in the N -body component.

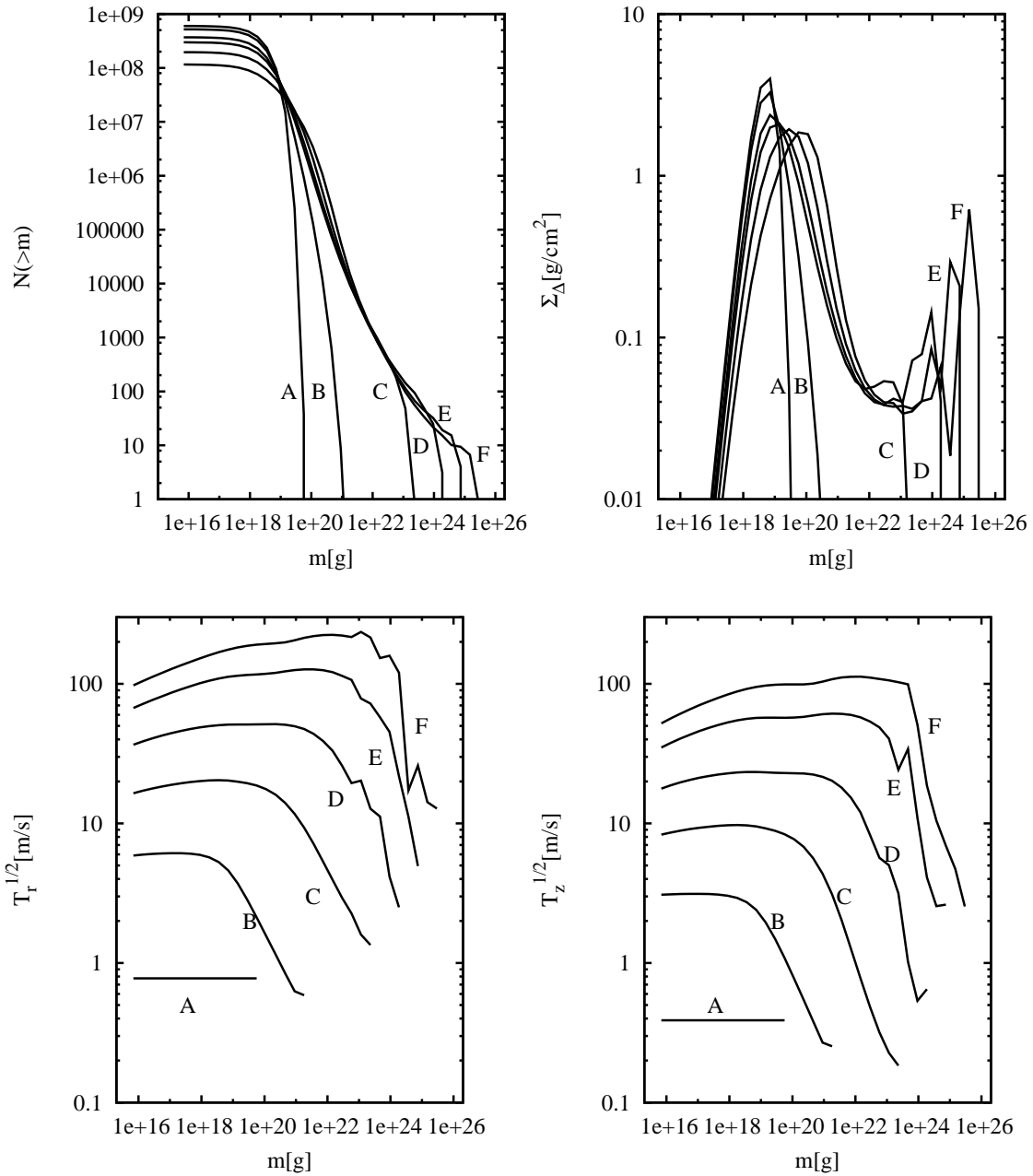


Figure 10.4: Summary of simulation S3FN, which assumes perfect mergers. Table 10.3 gives the time coding of the labels A–F.

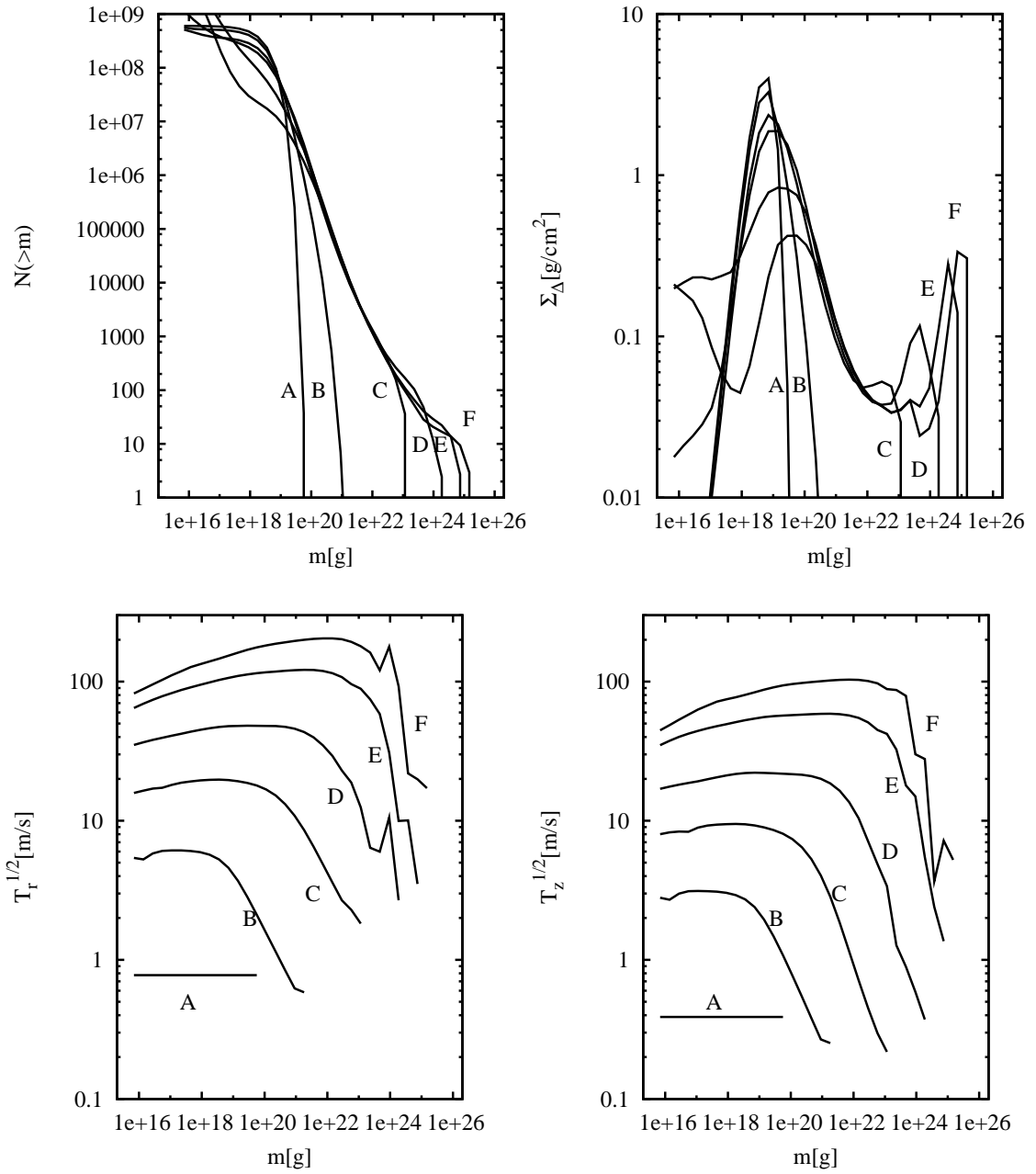


Figure 10.5: Summary of simulation S2FH, which uses the H&H 1990 strength. Table 10.3 gives the time coding of the labels A–F.

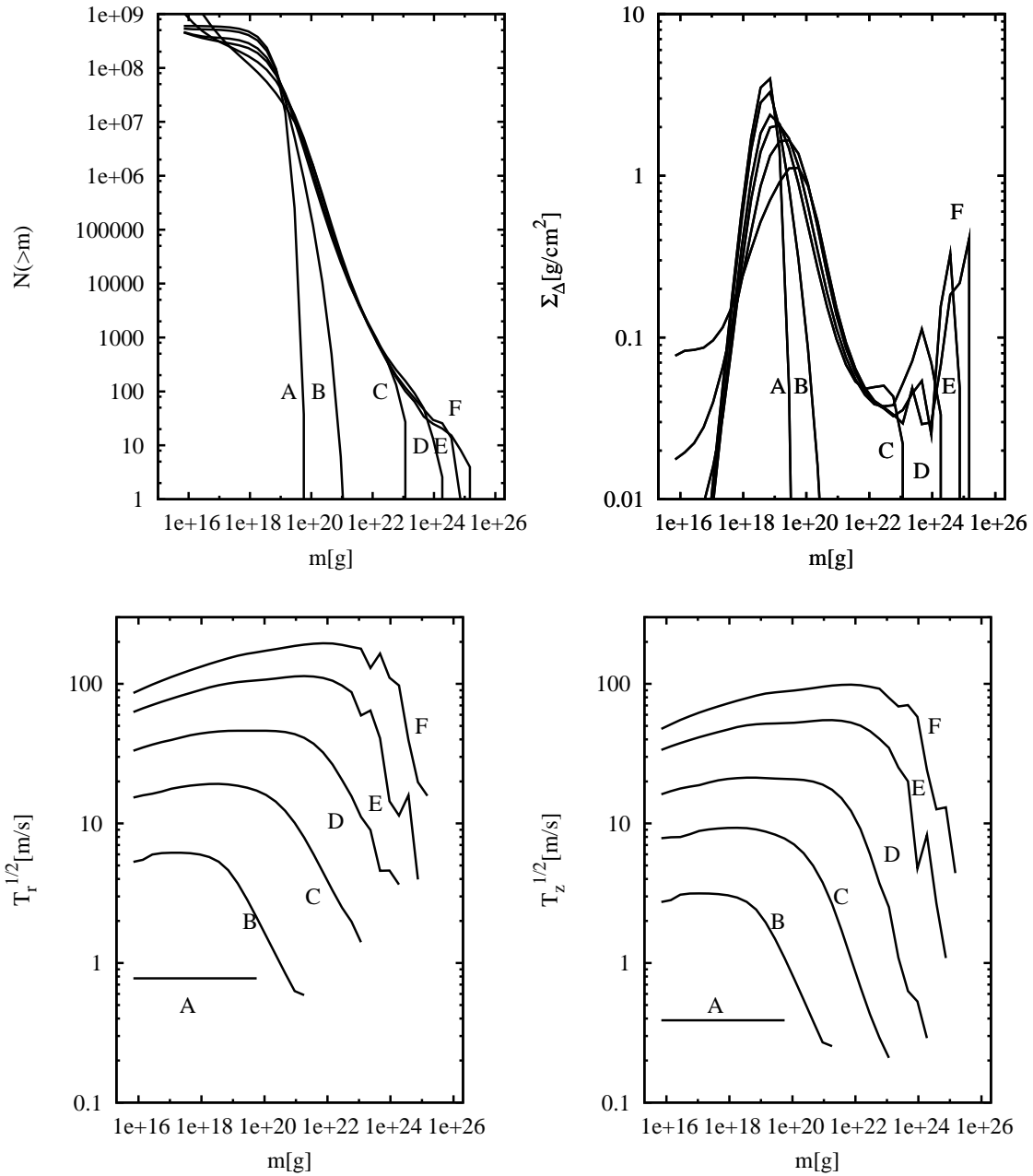


Figure 10.6: Summary of simulation S1FB, which uses the B&A 1999 strength. Table 10.3 gives the time coding of the labels A–F.

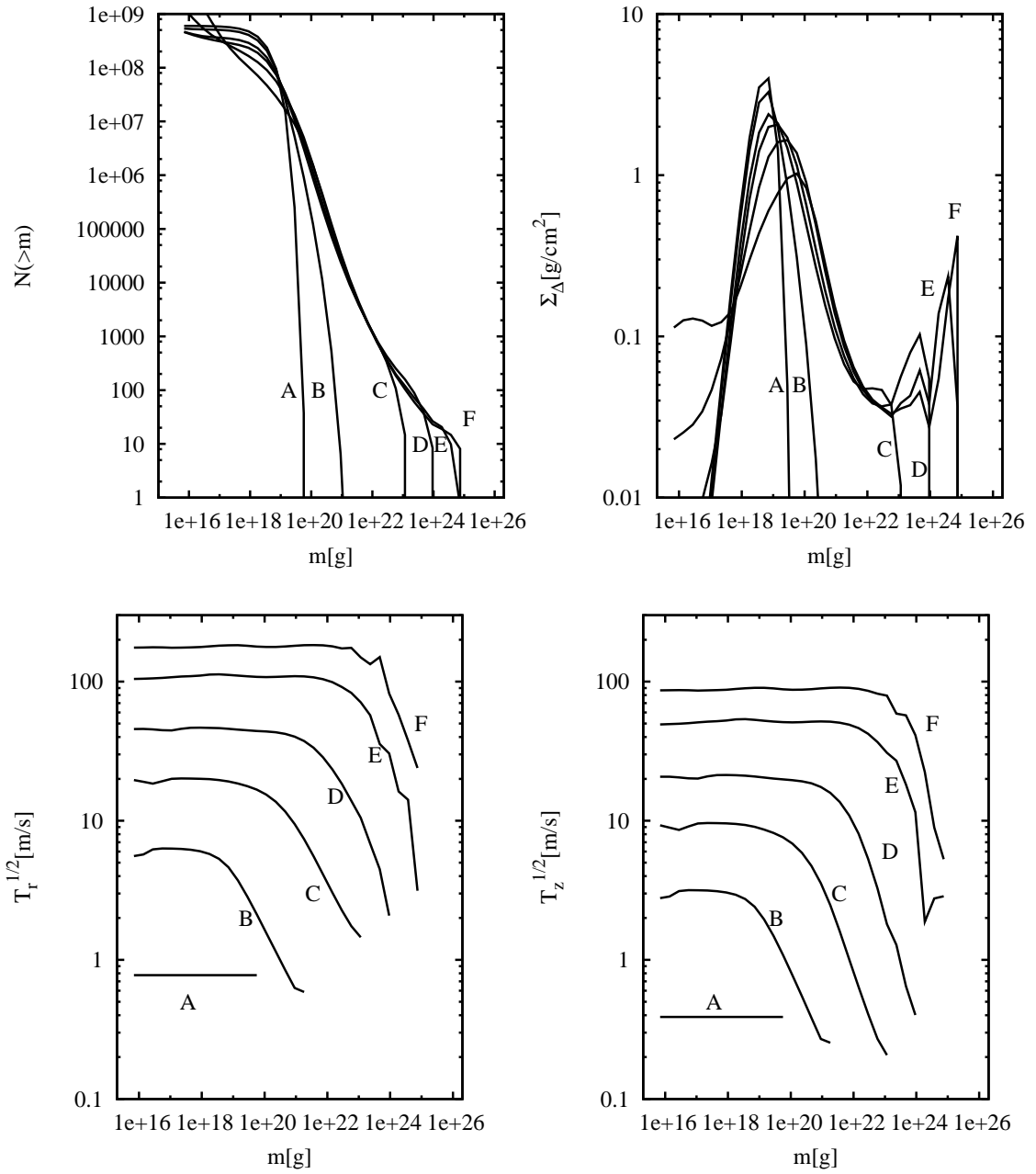


Figure 10.7: Summary of simulation S4FBN, which uses the B&A 1999 strength and a gas-free system. Table 10.3 gives the time coding of the labels A–F.

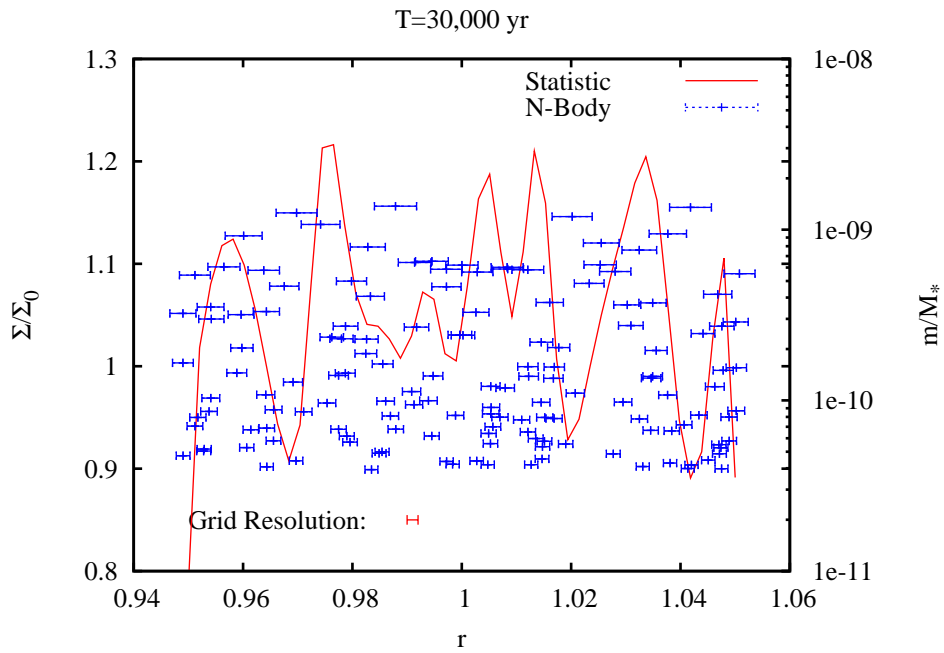


Figure 10.8: Radial density structure of the statistical component of model S1FB at $T = 30,000$ yr (left scale). Blue indicates the semimajor axis and masses (right scale) of the N -body particles. The error bars are 10 Hill radii wide and refer to the heating zone of each N -body particle.

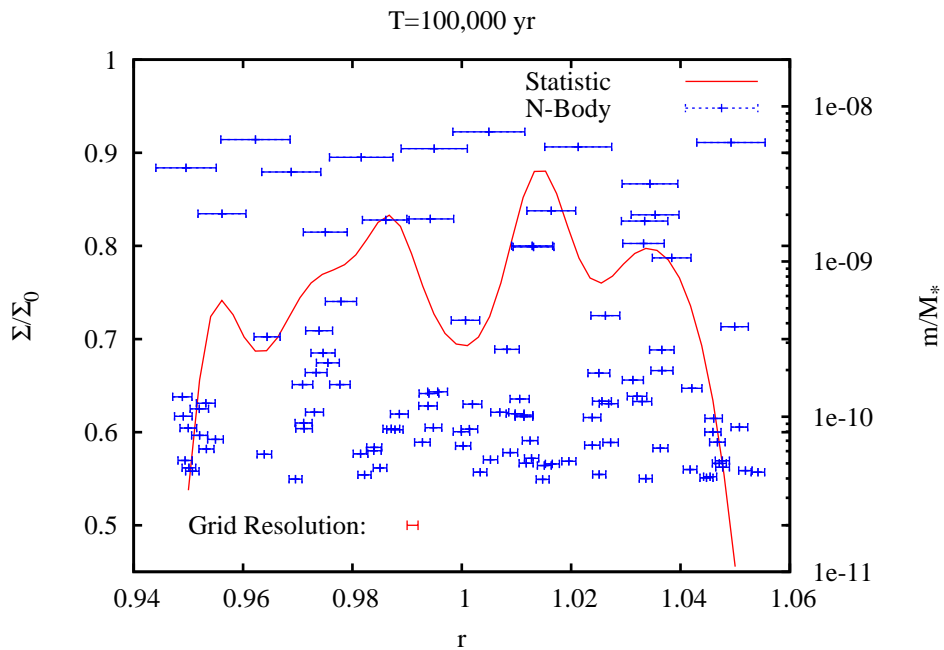


Figure 10.9: Same as Fig. 10.8 at $T = 100,000$ years.

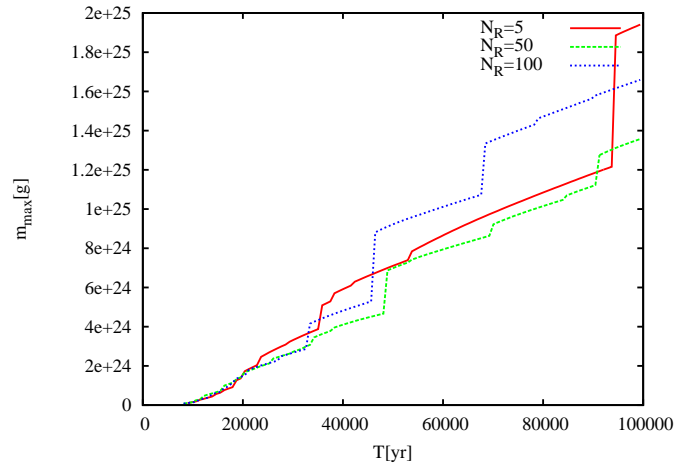


Figure 10.10: Largest body in the simulation as a function of time for the different resolutions S5FBL ($N_R = 5$), S1FB ($N_R = 50$) and S6FBH ($N_R = 100$).

(S6FBH). The nominal resolution is adjusted to the width of the heating zone of a planetesimal at the transition mass.

Fig. 10.8 depicts the spatial structure at $T = 30,000$ yr, i. e. shortly after stage D (nominal model S1FB). While the protoplanets are already massive enough after a few 10^4 years (stage C) to open gaps in the planetesimal component, there is only a weak correlation between the radial structures and the location of the most massive protoplanets. A closer examination of the time evolution of the radial structure reveals that most features are ‘fossils’ from the first emerged N -body particles, which are slowly erased by the diffusion of the field planetesimals. Fig. 10.9 confirms the further smoothing of the radial features. While major mergers among the protoplanets still lead to distinct features in the surface density even after a few 10^4 years, any further structuring ceases at the end of the simulation.

The absence of any prominent gap formation (fluctuations are smaller than 20 %) is related to the evolution of the overall size distribution. Though the gap opening criterion (see Eq. 3.51) is formally satisfied by all protoplanets during the runaway phase, the dense overlapping of the associated heating zones (compare Fig. 10.8) inhibits the evolution of any gap-like feature. As the protoplanets grow, they exert a growing influence on the dynamics of the planetesimal system. While this dominance should strengthen the possible formation of gaps, the system is already dynamically too hot to allow radial structures. The eccentricities of the field planetesimals are comparable to the width of the heating zone (compare Fig. 10.6, bottom), hence any planetesimal that is scattered to larger (or smaller) radii immediately encounters a neighbouring protoplanet.

In summary, the protoplanets (or rather their precursors) are too abundant when the system is dynamically cool enough, but when a group of mature protoplanets has evolved, the system is already too hot. Thus we expect an even less effective radial structuring for larger surface densities. While systems with a lower surface density may allow the formation of gap-like structures, they are so slowly evolving that planet formation may never reach the final growth phases.

10.2.3 Resolution

The minor role of gap formation is further supported by a comparison of the growth process for the three different radial resolutions $N_R = 5$, $N_R = 50$ and $N_R = 100$. Except some variations due to a different sequence of major impacts (see Fig. 10.10), all three simulations are in excellent agreement with respect to the mass loss and the total mass in the N -body component.

Accordingly, we find no differences between the various fragmentation models (S1FB, S2FH, S3FN, S4FBN) with respect to possible emerging gaps, except an earlier homogenisation in the

Simulation	Σ [g/cm ²]	m [g]	v_{Hill} [m/s]	$M_{\text{Nbody}}/M_{\text{Statistic}}$	M_{iso} [g]
S8_S2	2	2.6×10^{23}	10.5	0.04	7.8×10^{25}
S1FB	10	1.2×10^{25}	37.6	0.13	8.6×10^{26}
S9_S100	100	4.1×10^{26}	122.2	1.34	2.7×10^{28}

Table 10.4: Maximum mass and associated quantities at $T = 100,000$ years for different surface densities.

gas-free case S4FBN due to the stronger heating of the smaller planetesimals.

In addition, we conducted one simulation (S7FB2) with a significantly reduced (by a factor 10^5) lower mass grid boundary. Though the standard choice $m_{\text{min}} = 6.9 \times 10^{15}$ g is in accordance with the size regime where migration would remove the smaller fragments, the actual mass cut-off is less sharp as our estimations in Chapter 7 indicate. A reduced lower cut-off increases the dwell-time of collisional fragments in the system, thus increasing the mass fraction which could be accreted by the protoplanets. Hence the mass loss is reduced by 30 % as compared to the nominal model S1FB (Fig. 10.2). Though the shape of the fragment tail is modified by a different choice of the grid boundary, the change of the overall evolution of the protoplanets remains rather small.

10.2.4 Surface Density

Our last set of simulations examines the evolution of different surface densities. Again, simulation S1FB with a surface density of $\Sigma = 10$ g/cm² serves as a standard model. In addition, we explored two further surface densities: A low-mass disc with $\Sigma = 2$ g/cm² (S8_S2), and a high-mass disc with $\Sigma = 100$ g/cm² (S9_S100), which is close to the upper mass limit set by observations. The basic parameters of all three simulations are equal except a proper scaling of the gas density and individually chosen transition masses.

Firstly, we resume the inspection of possibly emerging gaps. While the low mass case shows a more pronounced radial structure (fluctuations up to 40 %), these features are only weakly related to the location of the largest protoplanets. Hence these structures are signatures of the first N -body particles. The high mass case exhibits no strong features at all, except for very weak features during the initial runaway phase. These findings strengthen the discussion in Section 10.2.2, assigning only a minor role to gap formation in the planetesimal component during the protoplanet accretion.

The overall growth process follows a standard pattern. Since the accretion rate in all three simulations is directly proportional to the surface density (compare Eq. 3.52), we rescale the time to the reference simulation S1FB. Thus we get a good agreement in the time evolution of the largest mass in the system (see Fig. 10.12), though the turnover to the slower oligarchic growth occurs at different (scaled) times. Likewise, we rescale the time to ease the comparison of the mass loss in the three simulations (Fig. 10.13).

As soon as a set of dominant protoplanets has evolved, they control the velocity dispersion of the field planetesimals. Therefore the magnitude of the velocity dispersion matches the Hill velocity of the largest body in the system (see Table 10.4 and Fig. 10.6, 10.15 and 10.16).

While this similarity of the three simulations is also in good agreement with standard estimations of the growth process (see the Introduction in Chapter 3), the later stages differ markedly. Since a larger surface density implies larger (and faster growing) protoplanets, the velocity dispersion of the field planetesimals is also driven to higher velocities. Hence we notice an increased mass loss as the initial surface density increases (Fig. 10.13). The mass loss of the most massive setup S9_S100 reduces the surface density nearly to the standard case S1FB. Since the mass loss is not due to a ‘true’ migration of the smaller fragments, but due to the lower grid boundary (in mass) which mimics the effect of migration, we examine this finding in more detail.

The influence of fragmentation on the protoplanetary growth is mainly determined by two timescales: The fragmentation time τ_{frag} , which refers to planetesimal–planetesimal collisions and the growth timescale τ_{grow} of the protoplanetary accretion. We employ the expressions de-

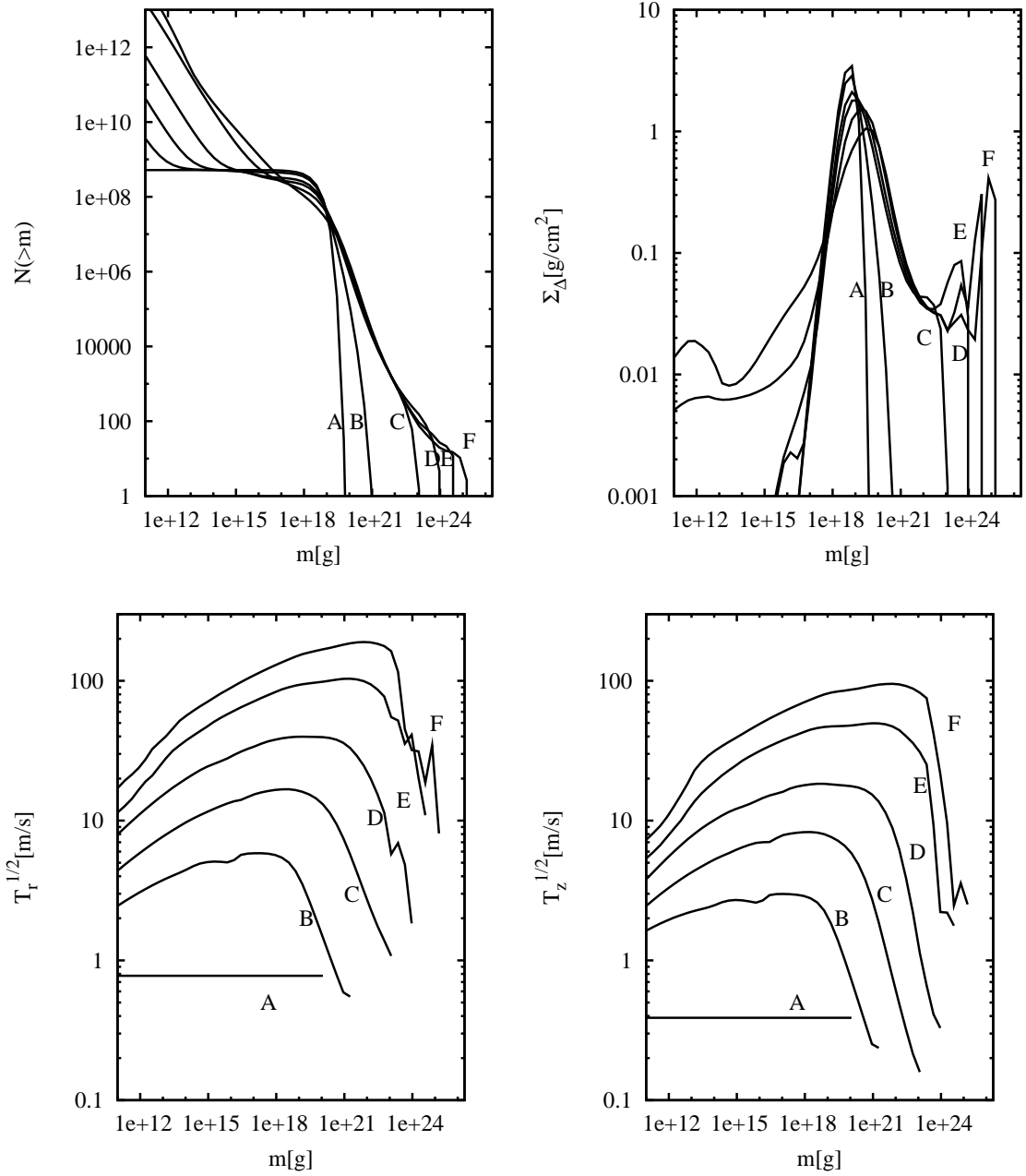


Figure 10.11: Summary of simulation S7FB2, which uses the B&A 1999 strength and a smaller lower cut-off mass.

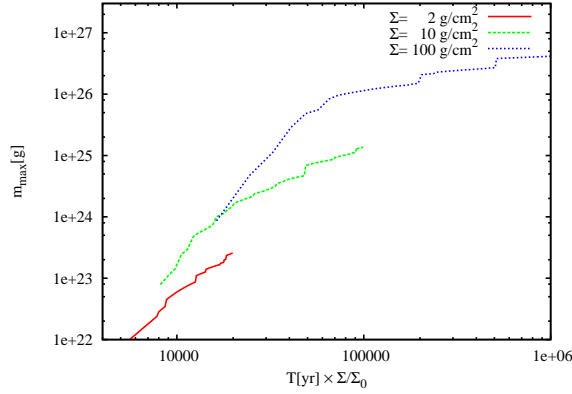


Figure 10.12: Largest body in the simulation as a function of time for the different surface densities S8_S2 ($\Sigma = 2 \text{ g/cm}^2$), S1FB ($\Sigma = 10 \text{ g/cm}^2$) and S9_S100 ($\Sigma = 100 \text{ g/cm}^2$). The reference density is $\Sigma_0 = 10 \text{ g/cm}^2$.

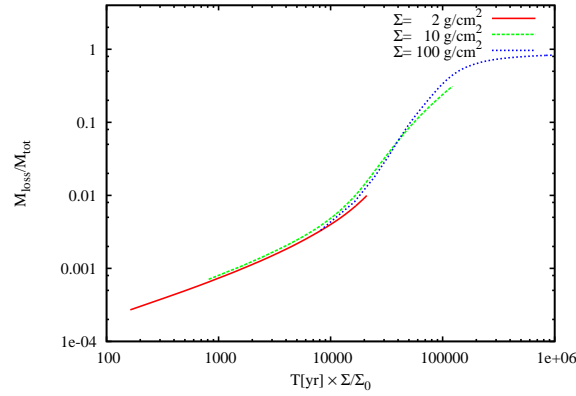


Figure 10.13: Mass loss in the simulation as a function of time for different surface densities (same as Fig. 10.12).

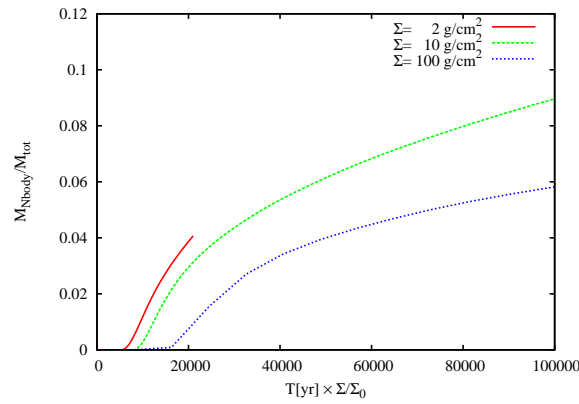


Figure 10.14: Mass in the N -body component of a simulation as a function of time for the different surface densities S8_S2 ($\Sigma = 2 \text{ g/cm}^2$), S1FB ($\Sigma = 10 \text{ g/cm}^2$) and S9_S100 ($\Sigma = 100 \text{ g/cm}^2$).

rived in Section 7.4 and the approximated differential surface density Eq. 10.8 to estimate the fragmentation time:

$$\tau_{\text{frag}} \approx \frac{\tilde{S}}{G'_0} \tau_0 \quad G'_0 \approx 10 \quad (10.9)$$

$$\approx \frac{\ln(m/m_0)}{80} \frac{R_m S_m}{\Sigma_m \Omega^3 R_{\text{Hill}}^2} \quad (10.10)$$

m is a typical mass of the largest planetesimals, R_m is the corresponding radius and S_m is the impact strength. Σ_m is the total surface density of the field planetesimals, with a lower cut-off m_0 due to migration. R_{Hill} is the typical Hill radius of a protoplanet, where it is assumed that the protoplanets control the velocity dispersion of the field planetesimals.

The growth timescale of the protoplanets follows immediately from rearranging Eq. 3.52:

$$\tau_{\text{grow}} \approx \frac{M \tilde{e}_m^2}{6\pi \Sigma_m \Omega R R_{\text{Hill}}} \quad (10.11)$$

Since the mass loss due to migration and the replenishment of smaller fragments by mutual collisions quickly establishes a stationary solution, the removal of the field planetesimals operates on the fragmentation timescale. Hence the accretion of the protoplanet ceases if the *mill condition*² is fulfilled:

$$\tau_{\text{grow}} > \tau_{\text{frag}} \quad (10.12)$$

This equation translates to lower a limit of the protoplanet mass ($\tilde{e}_m = 4$ is assumed)

$$M > \frac{1}{53} \ln(m/m_0) \frac{R_m S_m}{\Omega^2} \sqrt[3]{\frac{M_c}{a^3 \rho}} \quad (10.13)$$

which we denote as M_{mill} :

$$\frac{M_{\text{mill}}}{m} = \frac{f}{53} \ln(m/m_0) \left(\frac{2S_m}{\rho v_{\infty,m}^2} \right) \left(\frac{a^3 \rho}{M_c} \right)^{2/3} \quad (10.14)$$

ρ is the bulk density of the planetesimals. In addition, we used the escape velocity $v_{\infty,m}$ of the field planetesimals to arrive at a clearer expression. Since a more refined treatment of migration could alter the size of M_{mill} , we introduce an additional factor f to allow an adjustment if necessary. Hence f should be of order unity. A necessary condition for the mill process to operate is the presence of a gaseous disc. As a high surface density is needed for the protoplanetary growth to reach the mill mass, the growth itself is likely to be faster than the dispersal of the gaseous disc. However, this concept is also useful in a gas-free system. If the protoplanets in a given planetary system do not exceed the mill mass, it is still possible that the planets after the final giant impact phase exceed m_{mill} . While the absence of strong migration of the planetesimals³ prevents any reduction of the planetary accretion rate, the system enters nevertheless a qualitatively different stage: The evolution of the left-over planetesimals (i. e. the *disc clearing*) is now driven by fragmentation rather than accretion.

Before we apply the concept of the *mill condition* to our last set of simulations, it is useful to discuss the properties of M_{mill} in more detail. A robust feature of the mill mass is, that it is independent of the surface density of the field planetesimals. Hence it represents a universal upper limit of the protoplanet mass, given that all other parameters of the planetary system are fixed. The mill mass increases more steeply with increasing radius ($\propto r^2$) than the isolation mass for all realistic density profiles (e. g. $M_{\text{iso}} \propto r^{3/4}$ for the minimum mass solar nebula). This restricts

²We denote Eq. 10.12 as *mill condition*, since the protoplanets grind the surrounding planetesimals without retaining a significant fraction.

³*Radiative pressure* and *Pointing–Robertson drag* still provide an effective removal of dust-sized particles in a gas-free system. See the discussion in Burns et al. 1979 [28].

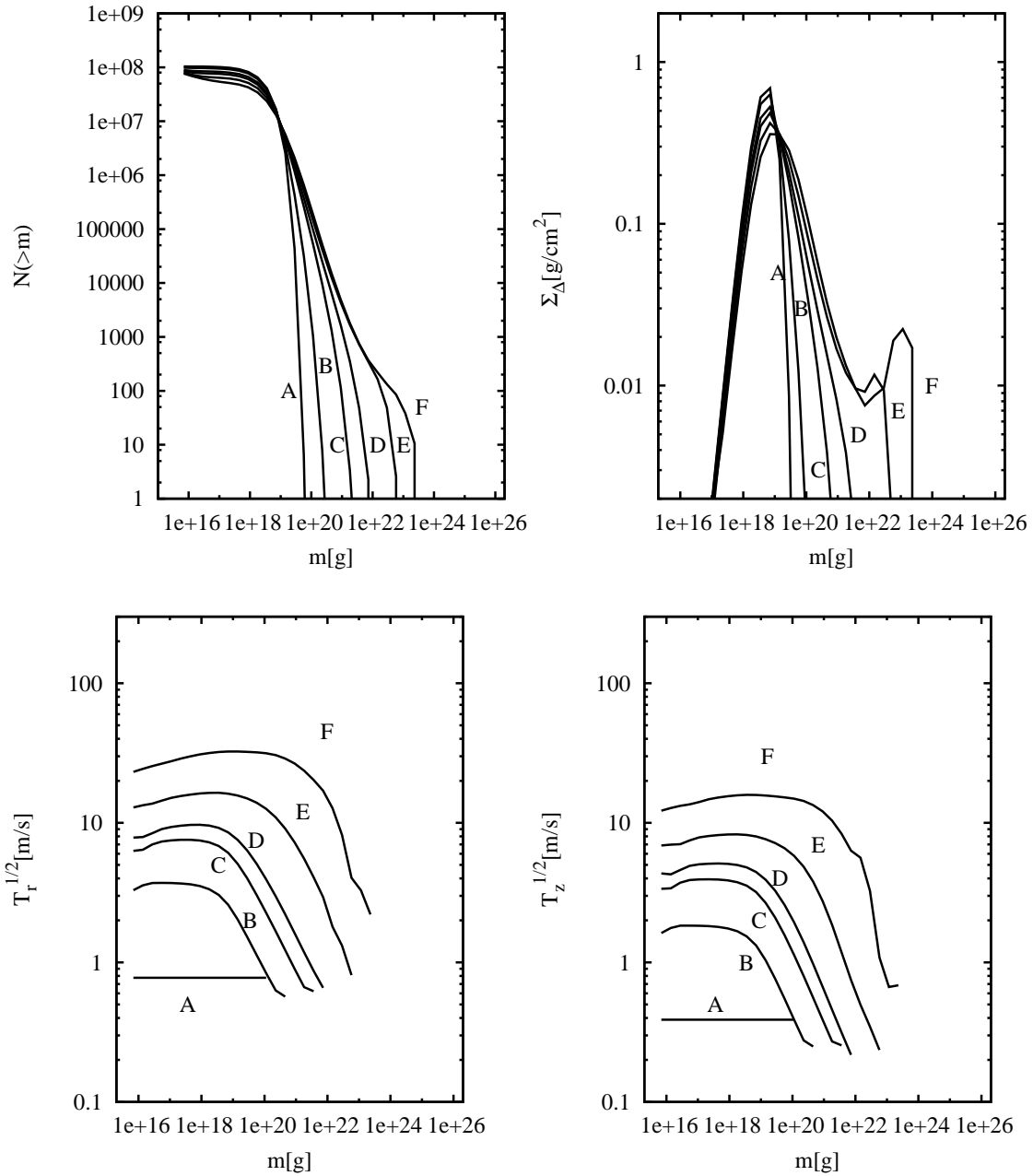


Figure 10.15: Summary of simulation S8_S2, which uses the B&A 1999 strength and a lower surface density $\Sigma = 2 \text{ g}/\text{cm}^2$. Table 10.3 gives the time coding of the labels A–F.

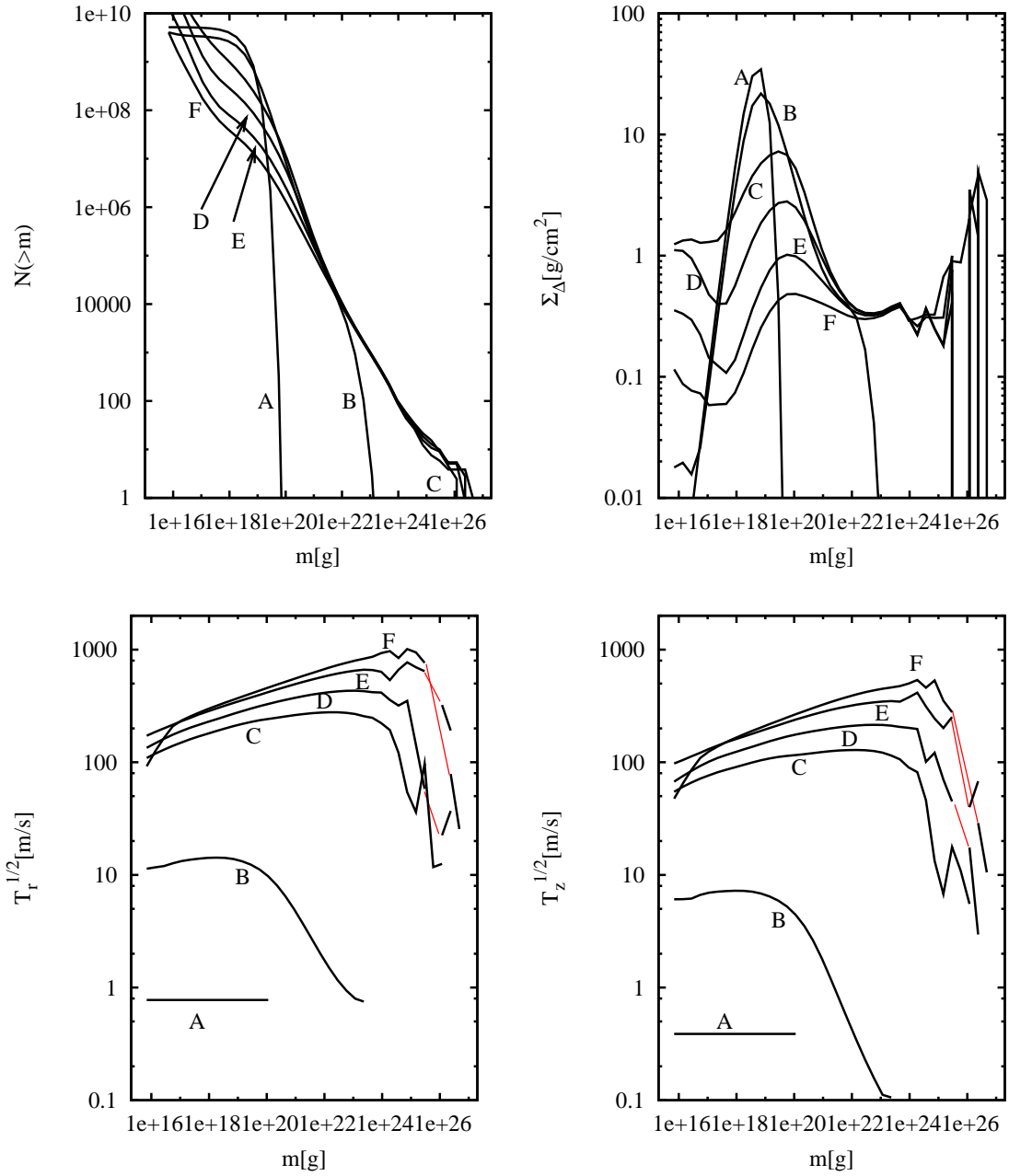


Figure 10.16: Summary of simulation S9_S100, which uses the B&A 1999 strength and a higher surface density $\Sigma = 100 \text{ g}/\text{cm}^2$. Red lines refer to empty mass bins.

the efficient termination of accretion by fragmentation to the inner parts (e. g. the terrestrial zone in the solar system) of a planetary system. The migration process enters only through the lower cut-off mass m_0 . While the uncertainty of m_0 seems less grave as it appears as a logarithm, the migration timescale depends on the planetesimal radius which still allows a strong variation. An uncertainty of the cut-off radius by a factor of ten indicates an uncertainty of M_{mill} of the same order, which strengthens the necessity of a careful treatment of migration in a global frame.

All simulations use a lower cut-off size of 800 metres, which is roughly equivalent to the cut-off introduced by migration. Since m_0 is defined by the identity of the migration timescale and the fragmentation timescale (see Chapter 7), this mass is also independent of the surface density, given that the ratio of solid to gaseous material is constant. While the more refined simulation S6FBH shows a mass loss only reduced by 30 %, we expect that the uncertainty due to the reduced treatment of migration is at least of the same order.

Given these restrictions, we turn to the analysis of the simulations. Simulation S9_S100 is strongly affected by the mill process, whereas simulation S1FB still retains a significant fraction of the initial mass. The quiescent conditions in simulation S8_S2 exclude a prominent role of fragmentation at any evolutionary stage. Thus we estimate $M_{\text{mill}} \approx 0.1 M_{\oplus}$ for a solar system analogue at 1 AU (see Fig. 10.12), which yields the approximate expressions:

$$M_{\text{mill}} = f \times 0.1 M_{\oplus} \times \left(\frac{r}{1 \text{ AU}} \right)^2 \left(\frac{M_c}{1 M_{\odot}} \right)^{-2/3} \left(\frac{\rho}{2.7 \text{ g/cm}^3} \right)^{2/3} \quad (10.15)$$

Since the protoplanets maintain a separation of approximately $10 R_{\text{Hill}}$, the mill mass corresponds to an upper limit Σ_{mill} of the surface density which is available for the formation of protoplanets:

$$\Sigma_{\text{mill}} = \frac{M_{\text{mill}}}{20\pi a R_{\text{Hill}}} \quad (10.16)$$

$$= f^{2/3} \times 9.15 \frac{\text{g}}{\text{cm}^2} \times \left(\frac{r}{1 \text{ AU}} \right)^{-2/3} \left(\frac{M_c}{1 M_{\odot}} \right)^{-1/9} \left(\frac{\rho}{2.7 \text{ g/cm}^3} \right)^{4/9} \quad (10.17)$$

The scaling relation Eq. 10.15 implies $M_{\text{mill}} \approx 2.5 M_{\oplus}$ at 5 AU, which is in agreement with an upper core mass of $4M_{\oplus}$ found in the simulations of Inaba et al. 2003 [68]. Though it seems impossible to form a core that is large enough ($15 M_{\oplus}$) to initiate gas accretion, this tight upper limit is due to the disregard of the gaseous envelope (i. e. the protoplanetary atmosphere before the onset of strong gas accretion) of the growing core. Since the gaseous envelope enhances the accretional cross section by an order of magnitude (thus $f \approx 10$ in Eq. 10.15), the mill mass increases by the same factor. Thus the formation of a $15 M_{\oplus}$ proto-jovian core at 5 AU is not ruled out by fragmentation, again in agreement with Inaba et al. 2003 who included this effect in subsequent simulations.

Both low-mass simulations S1FB and S8_S2 still contain a major fraction of the total mass in the statistical component, which prevents the onset of orbital crossing on a timescale of a few 10^5 years. However, the fast protoplanetary growth in the high-mass simulation S9_S100, accompanied by an intense mass loss, leads to an onset of strong protoplanet-protoplanet interactions already at the end of the simulation. The chaotic evolution of the velocity dispersion at the high mass end (Fig. 10.16 bottom) already indicates an intense interaction of the N -body particles.

Chapter 11

Discussion

We have developed a new hybrid code to explore the formation of protoplanets. After a careful assessment of the quality of the code, we applied this simulation tool to the formation of protoplanets. Our conclusions drawn from these simulations are the following:

- The influence of the fragmentation model on the protoplanetary growth is weak during the fast initial runaway growth. In particular, any realistic choice of the impact strength does not inhibit the growth of the planetesimals. However, the choice of the fragmentation model controls the oligarchic growth through the overall mass loss due to the migration of smaller fragments. Our simulations show that the Housen and Holsapple 1990 strength leads to a significant deceleration of the mass accretion in the later phases. Thus the recent impact strength from Benz and Asphaugh 1999 is more favourable in terms of an efficient protoplanet formation.
- We introduced the notion of a critical *mill mass* to provide a convenient handle on the fragmentation processes. If the mass of a protoplanet (or planet) exceeds this critical limit, then an interplay of destructive collisions and the removal of fragments by migration terminates the accretion of planetesimals. In particular, this critical mass implies an upper limit of the mass (in solids), which can be transformed into planets, unless migration ceases very early due to the fast dissipation of the gaseous disc.
- Opposed to the work of Rafikov 2001, we find no termination of the protoplanetary accretion due to gap formation. None of our simulations shows any significant radial structure, except for a limited time during the runaway accretion. While low surface densities favour gap formation, all observed radial features are so weak that the notion ‘gap’ should be applied with care to these structures. Hence resonant interactions between protoplanets and the field planetesimals are not a dominant process during the growth phases considered, which also supports the validity of the Fokker–Planck approach. Likewise, the dynamically hot field planetesimals also suppress non-axisymmetric features beyond the Hill radius of the protoplanets.

The eccentricity and inclination of the protoplanets remain small during the oligarchic growth phase. However, we note that this does not imply small eccentricities of the final planets, since the onset of orbital crossing terminates the dynamically quiet oligarchic growth phase.

While the implementation and some code details are newly introduced to the field of planet formation simulations, the first hybrid approach has been developed more than ten years ago. Spaute et al. 1991 [133] (further improved in Weidenschilling et al. 1997 [149]) constructed a hybrid code with a statistical component to treat the smaller particles and a special treatment for the larger particles. A statistical model covers the field planetesimals with the help of a distribution function (similar to Wetherill and Stewart 1989 [150]), whereas the larger particles are individually stored and characterised by mass, semimajor axis, eccentricity and inclination. While

the interaction between these single particles and the statistical component is expressed by standard viscous stirring and dynamical friction terms, perturbations among the single particles are equated in a different way. First, the probability of an encounter of two neighbouring particles is calculated. This probability is used in a second step to decide whether a (numerically integrated) two-body encounter of the neighbouring particles is carried out to derive the change in the orbital elements. Though these two well-defined code components justify to speak about a hybrid approach, the Monte-Carlo like integration of the largest particles is still closely related to a statistical treatment.

The first ‘true’ (from this work’s point of view) hybrid code has been developed by Jewell and Alexander 1996 [70](abstract only). While this short abstract describes briefly their method as a combination of a direct N -body approach for the larger particles and a statistical component for the smaller planetesimals, further detailed publications on the method and its applications have not appeared yet. Thus it is not possible to discuss their work in more detail. However, this work is (to our knowledge) the first attempt to unify a statistical and a pure N -body approach within one simulation tool.

A modified N -body approach is used in the work of Levison et al. 2005 [94](abstract only). Their method covers the largest particles by a direct N -body code, which includes the smaller particles as ‘tracer’ particles. The term ‘tracer’ indicates that each particle represents a whole ensemble of planetesimals. Hence their approach includes additional stirring terms to guarantee a proper interaction of these aggregates with the ‘true’ N -body particles. Though this SPH-like treatment offers a new perspective on the solution of the planetesimal problem, Levison et al. are still working on the code¹.

Recently Kenyon and Bromley 2006 [78] published the description of a hybrid method with a basic approach similar to our work. They employ two velocity dispersions and the surface density of the planetesimals to describe the planetesimal system. The statistical component includes migration of the planetesimals and dust particles due to gas drag and Pointing-Robertson drag. In contrast to our approach, mass transport due to the diffusion of the planetesimals is not included, which precludes the study of spatial structures induced by the protoplanets. Moreover, their method uses the standard discretisation of the collisional flux (see Eq. 8.129), thus restricting the spacing factor to $\delta \lesssim 1.25$ (Kenyon and Luu 1998 [74]). Kenyon and Bromley chose a set of test calculations which focussed less on the technical aspects of their method, but on an overall comparison with a selected set of ‘standard’ works on planet formation. Their test simulations are in good agreement with the references simulations, thus indicating a comparable quality of the method.

While a variety of hybrid approaches emerged over the past years, this technique is still far from a routinely application and is still challenged by many open issues. Though hybrid codes bear the potential to address the dynamical evolution of a whole planetary system, the later stages of protoplanet formation initiate a strong interaction with the gaseous disc, which may require more diligence than the inclusion of few additional interaction terms. However, the development is picking up speed, which places our work in a good position for further research.

Since our work introduced a new computer code to study the growth of protoplanets, we primarily focussed on the careful assessment of its validity and a small parameter study to strengthen this approach. Considering that the current abilities of the hybrid code exclude global simulation which could address migration in a proper way, we restricted our studies to a small ring of planetesimals. However, our experience drawn from this work allows an outline of possible improvements. The wallclock time of a rather small simulation is dominated by the integration of the statistical component. As the radial extension of the simulation volume is increased, the computing time due to the statistical component increases linearly, whereas the computing time due to the N -body component increases proportional to the square of the radial width. If the resolution of the radial grid is reduced, the weight of the N -body part will further increase. A moderately extended model, which covers the inner planetary system up to 10 AU, requires the

¹See the comments in the online version of the talk at <http://www.boulder.swri.edu/~hal/talks.html> (23/3/2006).

long-term integration of 10^3 to 10^4 particles.

While these are only few particles compared to big star cluster simulations (e.g. Makino and Funato 2004 [101], Berczik et al. 2005 [18]), the long integration times of at least 10^6 orbits prevent the efficient parallelisation. A possible solution would be the usage of special GRAPE hardware in a standard PC cluster (see the extensive description in Fukushige et al. 2005 [42]). Although it is quite challenging to combine GRAPE with standard parallelisation techniques for the statistical components, it is a promising approach to allow more realistic simulations of a planetary systems.

The extension of the simulations towards longer integration times does not only require an optimisation of the hybrid code, but also a more careful modelling of the growing planets to account for the interaction with the gaseous disc. While these improvements are necessary to allow the consistent treatment of migration, they also open the study of the early debris disc phase. Debris discs could provide constraints on the planet formation process, since the low opacity of kilometre-sized planetesimals prevents the direct observation of the protoplanetary growth in extrasolar systems. Though all these improvements are not implemented yet, they encourage us to pursue the further development of the hybrid approach.

Appendix A

Symbols

a	:		Semimajor axis
e	:		Eccentricity
i	:		Inclination
τ	:		Longitude of the pericentre
ω	:		Longitude of the ascending node
C_D	:		Drag coefficient
C_r	:		Radial friction coefficient
C_ϕ	:		Azimuthal friction coefficient
C_z	:		Vertical friction coefficient
c_s	:		Sound velocity
D	:		Diffusion coefficient
ϵ	:	$(E_{\text{kin}}\rho)/(2SM)$	Scaled impact energy
E_J	:		Jacobi energy
f_l	:	M_l/M	Dimensionless largest fragment
f_{KE}	:	$2E_{\text{kin}}^{\text{frag}}/E_{\text{kin}}$	Energy partition coefficient
η	:		Time step control parameter
γ_t	:	$\Delta t_{\text{reg}}/\Delta t_{\text{irr}}$	Time step ratio
Λ	:		Coulomb logarithm
M_c	:		Central Mass (Star)
M_{iso}	:		Isolation mass
N_{bl}	:		Block size
N_{nb}	:		Neighbour number
n_p	:		Processor number
κ	:	$\sqrt{\frac{1}{r^3} \frac{d}{dr} (r^3 \Phi')}$	Epicyclic frequency
Ω	:	$\sqrt{\frac{GM_c}{r^3}}$	Kepler frequency
Σ	:	$\int \rho dz$	Surface mass density
Δt	:		Time step
ρ	:		Bulk density
S	:		Impact strength
σ	:		Collisional cross section

Symbols continued

T_r	:		Radial velocity dispersion
T_z	:		Vertical velocity dispersion
v_K	:	$r\Omega$	Velocity on a circular Kepler orbit
v_∞	:	$\sqrt{2GM/R}$	Escape velocity
v_{Hill}	:	$r_{\text{Hill}}\Omega = v_\infty\sqrt{R/6r_{\text{Hill}}}$	Hill velocity
r_{Hill}	:	$r\sqrt[3]{\frac{m_1+m_2}{3M_c}}$	Hill radius
h_{Hill}	:	$\sqrt[3]{\frac{m_1+m_2}{3M_c}}$	Reduced Hill radius
$\delta(x)$:		Dirac's delta function
$\Theta(x)$:		Heaviside step function
$\text{erf}(x)$:	$2\pi^{-1/2}\int_0^x \exp(-t^2)dt$	Error function
$\text{EXINT}(x)$:	$\exp(x)\Gamma(0, x)$	Exponential integral

Useful numbers

1 AU	:	$1.495\,978\,7066 \times 10^{13}$ cm	Astronomical unit
	:	$4.848\,136\,782 \times 10^{-6}$ pc	
1 yr	:	$3.155\,814\,950 \times 10^7$ s	1 sidereal year
G	:	$6.6742(10) \times 10^{-11}$ m ³ kg ⁻¹ s ⁻²	Gravitational constant
	:	$6.6742(10) \times 10^{-8}$ cm ³ g ⁻¹ s ⁻²	
v_\oplus	:	29.7859 km/s	Mean orbital velocity of the earth
10 g/cm ²	:	$1.12516 \times 10^{-6} M_\odot/\text{AU}^2$	
2.7 g/cm ³	:	$4.54462 \times 10^6 M_\odot/\text{AU}^3$	
R	:	6.4 km	Radius of a planetesimal with mass $m = 3 \times 10^{18}$ g
	:		
k_B	:	$1.380\,6505(24) \times 10^{-16}$ erg/K	Boltzmann constant
	:	$1.380\,6505(24) \times 10^{-23}$ J/K	
m_{H}	:	1.007 94(7) u	Standard atomic weight of hydrogen
u	:	$1.660\,538\,86(28) \times 10^{-27}$ kg	Atomic mass unit
L_\odot	:	$3.845(8) \times 10^{33}$ erg/s	Solar luminosity (bolometric)
M_\odot	:	1.9891×10^{33} g	Solar mass
M_J	:	1.8987×10^{30} g	Jupiter mass
M_\oplus	:	5.9742×10^{27} g	Earth mass
M_\oplus	:	6.4191×10^{26} g	Mars mass
M_ζ	:	7.3482×10^{25} g	Moon mass
M_\oplus/M_\odot	:	$3.040\,433 \times 10^{-6}$	
M_J/M_\odot	:	$0.954\,792 \times 10^{-3}$	

The numbers are taken from *Allen's astrophysical quantities* [37] and the CODATA(2002)¹ recommended values of the fundamental physical constants.

¹Hosted by the National Institute of Standards and Technology (NIST), see <http://physics.nist.gov/cuu/index.html> (21/3/2006).

Appendix B

Central Force – Derivatives

Central force \mathbf{F} per mass (i. e. acceleration) and its time derivatives are:

$$\mathbf{F} = -\frac{\mathbf{x}M}{x^3} \quad (\text{B.1})$$

$$\mathbf{F}^{(1)} = -\frac{\mathbf{v}M}{x^3} - 3A\mathbf{F} \quad (\text{B.2})$$

$$\mathbf{F}^{(2)} = -\frac{\mathbf{a}M}{x^3} - 6A\dot{\mathbf{F}} - 3B\mathbf{F} \quad (\text{B.3})$$

$$\mathbf{F}^{(3)} = -\frac{\dot{\mathbf{a}}M}{x^3} - 9A\mathbf{F}^{(2)} - 9B\mathbf{F}^{(1)} - 3C\mathbf{F} \quad (\text{B.4})$$

$$\mathbf{a} = \dot{\mathbf{v}} \quad (\text{B.5})$$

$$A = \frac{\mathbf{x} \cdot \mathbf{v}}{x^2} \quad (\text{B.6})$$

$$B = \frac{v^2}{x^2} + \frac{\mathbf{x} \cdot \mathbf{a}}{x^2} + A^2 = \dot{A} + 3A^2 \quad (\text{B.7})$$

$$C = \frac{3\mathbf{v} \cdot \mathbf{a}}{x^2} + \frac{\mathbf{x} \cdot \dot{\mathbf{a}}}{x^2} + A(3B - 4A^2) \quad (\text{B.8})$$

The $\mathbf{F}^{(i)}$ denote the central force and its time derivatives, whereas \mathbf{a} and $\dot{\mathbf{a}}$ refer to the total acceleration of the particle. The assumption that \mathbf{x} , \mathbf{v} , \mathbf{a} and $\dot{\mathbf{a}}$ are independent of each other allows the derivation of averaged expressions for particle–particle interactions:

$$\langle (\mathbf{F})^2 \rangle = m^2 \frac{1}{x^4} \quad (\text{B.9})$$

$$\langle (\mathbf{F}^{(1)})^2 \rangle = m^2 \frac{2v^2}{x^6} \quad (\text{B.10})$$

$$\langle (\mathbf{F}^{(2)})^2 \rangle = m^2 \left(12 \frac{v^4}{x^8} + 2 \frac{a^2}{x^6} \right) \quad (\text{B.11})$$

$$\langle (\mathbf{F}^{(3)})^2 \rangle = m^2 \left(144 \frac{v^6}{x^{10}} + 126 \frac{a^2 v^2}{x^8} + 2 \frac{\dot{a}^2}{x^6} \right) \quad (\text{B.12})$$

We combine these expressions with Aarseth's time step formula to derive the regular time step as a function of the neighbour sphere radius R_s :

$$\Delta t_{\text{reg}} \approx \sqrt{\eta_{\text{reg}}} \frac{R_s}{\bar{v}} \frac{1}{1 + \sqrt{R_s/R_0}} \quad (\text{B.13})$$

$$R_0 = 4 \frac{\bar{v}^2}{a} \approx \frac{4\bar{v}^2 \bar{r}^2}{Gm} = 4 \frac{\bar{r}^2}{r_{\text{close}}} \quad (\text{B.14})$$

\bar{r} is the average particle distance and r_{close} is the impact parameter for a 90-degree deflection.

Appendix C

Plummer Model

The *Plummer model* is a simple theoretical model of the distribution of stars in a star cluster (Plummer 1911 [123]). It is characterised by the total mass M and a scale radius r_0 which define the potential–density pair:

$$\rho(r) = \frac{3M}{4\pi r_0^3} (1 + r^2/r_0^2)^{-5/2} \quad (\text{C.1})$$

$$\Phi(r) = -\frac{GM}{\sqrt{r^2 + r_0^2}} \quad (\text{C.2})$$

Thus the velocity dispersion (referring to an isotropic velocity distribution), the total potential energy and the total kinetic energy are:

$$\sigma^2(r) = \frac{1}{6} \frac{GM}{\sqrt{r^2 + r_0^2}} \quad (\text{C.3})$$

$$E_{\text{pot}} = -\frac{3\pi}{32} \frac{GM^2}{r_0} \quad (\text{C.4})$$

$$E_{\text{kin}} = \frac{3\pi}{64} \frac{GM^2}{r_0} \quad (\text{C.5})$$

It is appropriate to transform the physical units to so-called *N-body units* defined by

$$G = 1 \quad M = 1 \quad E = -1/4 \quad (\text{C.6})$$

to ease the numerical integration of the cluster evolution (see Aarseth et al. 1974 [1]).

Appendix D

Scalable Collisions Flux

The mass flux according to the perturbation equation 7.28 is:

$$F_p = - \iint (n(m_2)\Delta n(m_1) + n(m_1)\Delta n(m_2))\sigma(m_1)v(m_2)m_1 f_m(m_1/m, \epsilon) dm_1 dm_2 \quad (\text{D.1})$$

$$= F^{(1)} + F^{(2)} \quad (\text{D.2})$$

Firstly, we employ the substitution

$$m_1 = mx_1 \quad (\text{D.3})$$

$$m_2 = m_0 \left(\frac{m_1}{m_0} \right)^{\frac{1+\alpha}{1+2w}} (\tilde{S})^{\frac{1}{1+2w}} \epsilon^{\frac{1}{1+2w}} \quad (\text{D.4})$$

to solve for the partial flux $F^{(1)}$:

$$F^{(1)} = -n_0^2 m_0^3 \sigma_0 v_0 \int g(mx_1) F_1(x_1) dx_1 \quad (\text{D.5})$$

$$F_1(x_1) = \tilde{S}^{-k'} \int \epsilon^{-\frac{w+s+3+\alpha}{2+\alpha+2w}} \frac{f_m(x_1, \epsilon)}{x_1(1+2w)} d\epsilon \quad (\text{D.6})$$

The second contribution $F^{(2)}$ requires a slightly different transformation:

$$m_1 = mx_1 \epsilon^{-1/(1+\alpha)} \quad (\text{D.7})$$

$$m_2 = m_0 \left(\frac{mx_1}{m_0} \right)^{\frac{1+\alpha}{1+2w}} (\tilde{S})^{\frac{1}{1+2w}} \quad (\text{D.8})$$

Thus the partial flux $F^{(2)}$ is:

$$F^{(2)} = -n_0^2 m_0^3 \sigma_0 v_0 \int g(m_2) F_2(x_1) dx_1 \quad (\text{D.9})$$

$$F_2(x_1) = \tilde{S}^{-k'} \int \epsilon^{-\frac{w+s+3+\alpha}{2+\alpha+2w}} \frac{f_m(x_1 \epsilon^{-1/(1+\alpha)}, \epsilon)}{x_1(1+2w)} d\epsilon \quad (\text{D.10})$$

We change to a new set of logarithmic coordinates

$$u = \ln(m/m_0) \quad u_1 = \ln(x_1) \quad \tilde{s} = \frac{\ln(\tilde{S})}{1+\alpha} \quad (\text{D.11})$$

which transforms the total flux F_m to a convolution integral:

$$F_p = -n_0^2 m_0^3 \sigma_0 v_0 \int (g(u+u_1)G_1(u_1) + g(p(u+u_1+s_1))G_2(u_1)) du_1 \quad (\text{D.12})$$

$$p = \frac{1+\alpha}{1+2w} \quad (\text{D.13})$$

$p = 1$ refers to the already derived solution for self-similar collisions. Hence we expand Eq. D.12 at $p = 1$ and retain only the zeroth-order moment of the fragmentation kernel:

$$F_p = -n_0^2 m_0^3 \sigma_0 v_0 \left(g(u) G_{1,0} + \left(g(u) + u(p-1) \frac{\partial g}{\partial u} \right) G_{2,0} \right) \quad (\text{D.14})$$

This expression is equivalent to

$$F_p = -n_0^2 m_0^3 \sigma_0 v_0 (g(u) G_{1,0} + [g(u) + (p-1)(g(u) - g(0))] G_{2,0}) \quad (\text{D.15})$$

where higher derivatives of $g(u)$ are neglected. Hence we recover the same functional form of the perturbed mass flux F_p as for self-similar collisions:

$$F_p = -n_0^2 m_0^3 \sigma_0 v_0 g(u) (G_{1,0} + p G_{2,0}) + \text{const.} \quad (\text{D.16})$$

$$\propto \tilde{S}^{-k'} \quad (\text{D.17})$$

Appendix E

Coagulation Equation

While the success of a general approximation of the coagulation equation depends heavily on the used coagulation kernel, we nevertheless provide a more general approach to embed Chapter 7 in a broader context. The standard coagulation equation is:

$$0 = \frac{\partial}{\partial t} mn(t, m) + \frac{\partial}{\partial m} F_m(t, m) \quad (\text{E.1})$$

$$F_m = - \iint n(t, m_1) n(t, m_2) \sigma(m_1, m_2) v_{\text{rel}} M_{\text{red}}(m, m_1, m_2) dm_1 dm_2 \quad (\text{E.2})$$

In virtue of our experience drawn from the perturbation expansion, we transform the coagulation equation to logarithmic coordinates

$$u = \ln(m) \quad (\text{E.3})$$

and employ the size distribution $g(u)$ relative to the steady-state solution $n_{\text{eq}}(m)$:

$$0 = \frac{\partial}{\partial t} g(u, t) n_{\text{eq}}(u) e^{2u} + \frac{\partial}{\partial u} F_u(t, m) \quad (\text{E.4})$$

$$F_u = - \iint g(t, u_1) g(t, u_2) K(u, u_1, u_2) du_1 du_2 \quad (\text{E.5})$$

$K(u, u_1, u_2)$ is the properly transformed new coagulation kernel. $g(u)$ is expanded under the integral to arrive at a moment expansion of the flux F_u :

$$F_u = -K_{00}(u) g(u)^2 - (K_{10}(u) + K_{01}(u)) g(u) \frac{\partial g}{\partial u} + \dots \quad (\text{E.6})$$

$$K_{ij} = \iint K(u, u_1, u_2) u_1^i u_2^j du_1 du_2 \quad (\text{E.7})$$

Retaining only the leading order terms, we recover an approximate coagulation equation which is similar to the *inviscid Burgers' Equation*¹:

$$0 = \frac{\partial}{\partial t} g(u, t) n_{\text{eq}}(u) e^{2u} - \frac{\partial}{\partial u} (K_{00}(u) g(u)^2) \quad (\text{E.8})$$

¹This notion goes back to Burgers 1948 [27], but the equation was already introduced by Bateman 1915 [13].

Appendix F

Computing Facilities

Name	Hydra	Titan	JUMP
Institut	ARI/ZAH	ARI/ZAH	Forschungszentrum Jülich
Location	Heidelberg	Heidelberg	Jülich
Processors	20	64	1248
Speed	2.2GHz	3.2GHz	1.7GHz
Processors/Node	2	2	32
Network	Myrinet	Infiniband	Gigabit-Ethernet
Bandwidth	2Gbit/sec	20 Gbit/sec	10 Gbit/sec

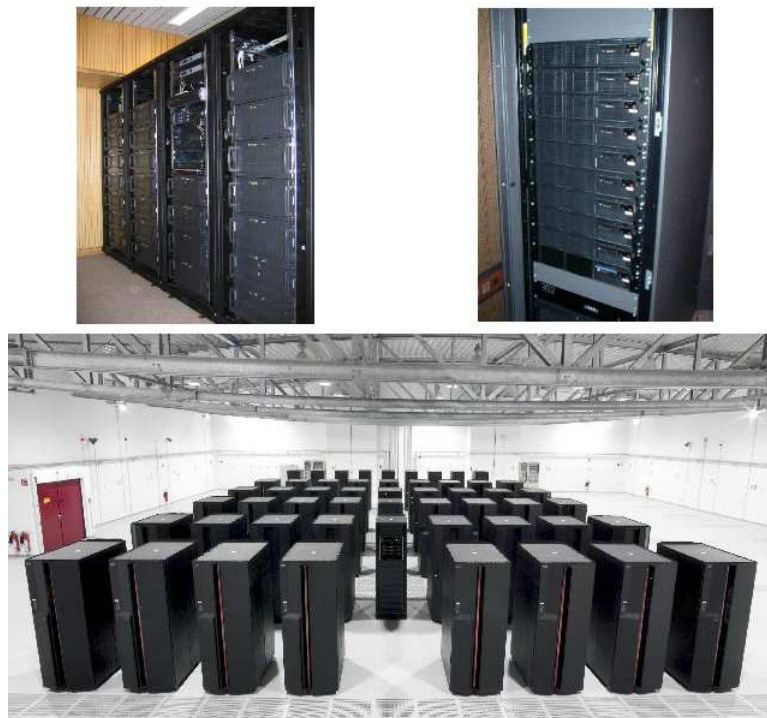


Figure F.1: Images of the used supercomputers. Titan (upper left), Hydra (upper right) and JUMP (bottom). Each cabinet of the JUMP system represents one node (i. e. 32 processors).

Appendix G

Rendering Planetesimals

The surface $r(\phi, \theta)$ of each planetesimal is expanded in surface harmonics

$$r(\phi, \theta) = R_0 + \sum_{l=2}^{l_{\max}} \sum_{m=0}^l A_{lm} \sqrt{\frac{(l-m)!}{(l+m)!}} P_l^m(\cos \theta) \cos(m\phi + \phi_{lm}) \quad (\text{G.1})$$

where P_l^m are associated Legendre polynomials and R_0 is the mean radius. The shape of the surface is controlled by the phases ϕ_{lm} and the amplitudes A_{lm} . Since planetesimals are randomly oriented in space, we choose these parameters according to:

$$A_{lm} = \begin{cases} 2\sigma_l R_{lm} & \text{for } m > 0 \\ \sigma_l W_{lm} & \text{otherwise.} \end{cases} \quad (\text{G.2})$$

$$\phi_{lm} = \begin{cases} 2\pi Z_{lm} & \text{for } m > 0 \\ 0 & \text{otherwise.} \end{cases} \quad (\text{G.3})$$

Z_{lm} are independent uniform deviates, the coefficients W_{lm} are independently normally (Gaussian) distributed and R_{lm} indicates Rayleigh distributed values. Since the dipole terms $l = 1$ mainly imply a displacement of the basic sphere R_0 , they are excluded in the summation. We derive the correlation between the altitudes r_1 and r_2 at two different locations separated by an angle γ to clarify the meaning of the coefficients σ_l :

$$\langle (r_1 - R_0)(r_2 - R_0) \rangle = \sum_{l=2}^{l_{\max}} \sigma_l^2 P_l(\cos(\gamma)) \quad (\text{G.4})$$

Hence the σ_l are related to the altitudes of surface features associated with a length scale $2\pi R_0/l$. While the determination of these coefficients would require a detailed simulation of the accretional process, we recede to a simple estimate. Random accretion¹ of a collisional relaxed population of planetesimals implies $\sigma_l \propto 1/l$. While subsequent impacts level older surface structures, we use a more steep function $\sigma_l \propto 1/l^2$. If asteroids are larger than $R_s \approx 140$ km (see e. g. Hughes and Cole 1995 [59]), self-gravity enforces a more spherical shape. Thus we modify the amplitudes σ_l to

$$\sigma'_l = \min(\sigma_l, R_s^2/R_0) \quad (\text{G.5})$$

The surface texture is generated from a *Perlin noise*² function, combined with a modified *lambert shading* to suppress a completely dark far side of the planetesimals. We apply a standard raytracing technique to render the entire disc.

¹All accreted particles stick at the impact site without significantly reshaping the planetesimal.

²Perlin noise is similar to properly filtered white noise. It was first implemented by Ken Perlin to generate realistic computer graphics efficiently. See <http://mrl.nyu.edu/~perlin/> (28/3/2006).

Appendix H

Files

Output files:

FILE	Purpose
COLLHIS.16	Collisions logfile
DISCDAT.17	Complete disc configuration every DELTAT
disc.dat	Disc initial values in binary Format
discout.dat	Final disc data at end of a run
fort.44	Debugging Output
fort.45	Debugging Output
fort.66	Debugging Output

KDISC options:

No.	Value	Action
1	0	Standard initial model
	1	Read from disc.dat
	2	Read from homdisc.dat
2	1	Write final data to discout.dat
3	1	Run disc until first particles emerge and stop
4	0	Simple diag. output
	1 or 2	More diag. output
5	0	Open at lower mass
	1	Closed at lower mass
	2	No accretion
	3	Perfect merger
6	1	Particle reflection at radial boundaries
7	1	Activate BINCORREL
8	1	Switch on radial diffusion

Extended input file. The box indicates the additional variables for NBODY6DISC:

```
1 5E9 200000 40 40
30 1 10 1006 15 1
0.001 0.002 0.4 5120. 5120. 1E10 5.0E-07 4.848E-06 0.2919E-16
1 1 1 0 1 0 0 0 0 0
0 0 0 0 0 1 0 0 0 2
1 2 1 0 0 2 0 0 0 0
0 0 2 0 1 0 1 1 0 1
0 0 0 0 0 0 0 0 0 0
0.0 0.01 0.002 1.0 1.0E-06 0.01
```

0.0 1.0 1.0 1.0 0.0
2.7 1.0
1.726D7 0.1 0.01 1D-9 6000.
1 1 0 0 3 1 0 1 0 0

```
2.3 1.0 1.0 0 0.0 0.0
0.5 0.0 0.0 0.0
0 0.005 -1.0 1.0 5.0 5 0
```

Corresponding variables:

KSTART, TCOMP, TCRIT _p , isernb, iserreg	(nbody6.F)
N, NFIX, NCRIT, NRAND, NNBOPT, NRUN	(input.F)
ETAI, ETAR, RSO, DTADJ, DELTAT, TCRIT, QE, RBAR, ZMBAR	(input.F)
(KZ(J), J=1,40)	(input.F)
(BK(J), J=1,10)	(input.F)
DTMIN, RMIN, ETAU, ECLOSE, GMIN, GMAX	(input.F)

Q _{Drag} C3 HZ CMBLHOLE EPS ₁ (input.F)
DENSITY FRADIUS (input.F)
S0 [erg/cm ³] fKE ETADISC RHOGAS [g/cm ³]
VGAS [cm/s] (input.F)
KDISC(1..10) (input.F)

ALPHA, BODY1, BODYN, NBINO, ZMET, EPOCHO	(data.F)
Q, VXROT, VZROT, RSPH2	(scale.F)
NBIN, SEMIO, ECCO, RATIO, RANGE, NSKIP, IDORM	(binpop.f)

Appendix I

New Subroutines

Subroutine	Function	Called By
centrfinit.f	Time step initialisation	FPOLY1 / FPOLY2
centrstarf.f	Calculates F, \vec{F}	FPERT, KSPERT, KSPOLY, REGINT
centrstarf1.f	Calculates F, \vec{F} at startup	CENTRFINIT
centrstarf2.f	Calculates $F^{(2)}, F^{(3)}$ at startup	CENTRFINIT
centrstarfd.f	Calculates $F^{(2)}, F^{(3)}$ of the central force	CENTRSTARPCM2
centrstarpcm.f	Calculates perturbation on C-M particle	REGINT NBINT NBFORCE FPOLY1
centrstarpcm2.f	Calculates $F^{(2)}, F^{(3)}$ of C.M. Perturbation	FPOLY2 CENTRFINIT
centrstarpcm.f	Calculates F_{pert} , see Eq. 4.54	REGINT NBINT
centrstarpot.f	Central Potential	NBPOT, ENERGY, ENERGY_MPI
dragforce.f	Dragforce + first derivative	FPERT, KSPERT, KSPOLY, NBINT, REGINT
dragforce1.f	Dragforce + first derivative	CENTRFINIT
collinit.f	Initialise constants and particle radii	START
icomtab.f	Initialise Communication table for parallel execution	ZERO
orbitdat.f	Calculates orbital elements	Various
rijmod.f	Distance modification factor	Various
bodystrength.f	Calculates planetesimal strength	DISCINIT / CALCFLUXB
calcflux.f	Disc–disc collisions	SUMFLUX
calcfluxb.f	Disc–particle collisions	SUMFLUXB
calchj.f	H_k and J_k functions	DYNFRICFC / TRZDOTBIN / TRZDOTBODY
collisions.f	Look–up table for FRAGBODY	BLOCK DATA
discinit.f	Disc setup	START
dynfricf.f	Disc–particle interaction coefficients	DRAGFORCE / DRAGFORCE1
exint.f	EXINT function	PVSDIST

Subroutine	Function	Called By
fragbody.f	f_l and $f_l^{(2)}$ interpolation	CALCFLUX / CALCFLUXB
fragmred.f	M_{red}	CALCFLUX / CALCFLUXB
growbodies.f	Mass accretion from disc	INTGRT
intdisc.f	Integrate disc	INTGRT
insbody0.f	Prepare particle insertion	NEWBODIES
insbodym.f	Complete particle insertion	INTGRT
newbodies.f	Create new particles	INTGRT
pvsdist.f	Viscous stirring due to distant encounters	TRZDOTBIN/ TRZDOTBODY / DYNFRICFC
startdisc.f	Runs only statistical component	START
sumflux.f	Summation over all mass bins	INTDISC
sumfluxb.f	Summation over all mass bins	INTDISC
trzdotbin.f	Disc-disc stirring	INTDISC
trzdotbody	Disc-particle stirring	INTDISC
xmergemred	M_{red} of a merger	CALCFLUX / CALCFLUXB
weightc.f	Weight function close encounters	CALCFLUXB / TRZDOTBIN / TRZDOTBODY
weightd.f	Weight function distant encounters	CALCFLUXB / TRZDOTBIN / TRZDOTBODY
writedisc.f	Disc data input and output	INTDISC / STARTDISC

Appendix J

New Variables

Variable	Function	COMMON
EDISS1	Total dissipated energy	DRAG1
EDISS1.LOC EDISS.SAVE	Add. variables for parallel execution summation	DRAG1 DRAG1
EBLCKHL	Contribution of central potential to total energy	DRAG1
PF(NMAX)	Dissipation rate W	DRAG1
PFDOT(NMAX)	Time Derivative of PF	DRAG1
T0FRIC(NMAX)	Last calculation of frictional constants	DRAG1
CFRICR(NMAX) CFRICZ(NMAX) CFRICRDOT(NMAX) CFRICZDOT(NMAX)	Frictional Constants	DRAG1 DRAG1 DRAG1 DRAG1
CMBLHOLE	Mass of central star	DRAG
Q_DRAG	Dissipative force parameter	DRAG
C3	Gaseous disc rotation parameter	DRAG
HZ	Gaseous disc scale height	DRAG
DENSITY	Particle density	COLL
FRADIUS	Radius enhancement factor	COLL
CENTIMETER GRAM SECOND	New unit conversion factors	COLL COLL COLL
SIM1/SIM2	Strength calculation constants	COLL
SIMG	Gravitational strength constant γ	COLL
FLM(10,6)	Look-up table largest fragment	COLL
FL2M(10,6)	Look-up table second largest fragment	COLL
SGL	γ for use of FLM / FLM2	COLL
INLIST(1:NMAX)	Optimised neighbour prediction	OPTIM
IPREDOK	Prediction speedup	OPTIM
KOMTAB(32,9)	Communication table for parallel runs	OPTIM
NLAY,NLAY2	Number of communication layers	OPTIM
ISIZEC	Number of ring communications	OPTIM
ISIZENB	disabled	OPTIM
ISIZE2P	disabled	OPTIM
IRED(32)	disabled	OPTIM

NRAD	Number of radial bins	STATD
NMASS	Number of mass bins	STATD
T0DISC	Last correction time	STATD
DTDISC	Disc time step	STATD
ETADISC	Time step control parameter	STATD
TDISCP	Output time	STATD
RDMIN	Inner disc radius	STATD
RDMAX	Outer disc radius	STATD
DELTAR	Radial width of a Bin	STATD
SDENS0(NMASS,NRAD)	Surface density at T0DISC	STATD
TZ0	T_r at T0DISC	STATD
TR0	T_z at T0DISC	STATD
TZDOT0	\dot{T}_r at T0DISC	STATD
TRDOT0	\dot{T}_z at T0DISC	STATD
SDENS	Temporary use	STATD
TZ		STATD
TR		STATD
TZDOT		STATD
TRDOT		STATD
DIFFC(NMASS,NRAD)	Diffusion coefficients	STATD
DXBMIN(NMASS)	Width of a mass bin	STATD
XMBIN(NMASS)	Central mass m_i of a bin	STATD
R0BIN(NMASS)	Particle radius	STATD
GAMBIN(NMASS)	γ	STATD
S0BIN(NMASS)	S_0	STATD
FKINEN	f_{KE}	STATD
S0IMP	S_0	STATD
XMLOSS	Lost mass	STATD
XMTRANS	Mass turned into particles	STATD
XMTOT	Total mass	STATD
EKTRANS	Energy shifted to particles	STATD
ONE24	1/24	PARAMS

Bibliography

- [1] Aarseth S. J., Hénon M., Wielen R., 1974. A comparison of numerical methods for the study of star cluster dynamics. *Astronomy and Astrophysics* **37**, 183–187
- [2] Aarseth S. J., 1985. Direct Methods for N -Body Simulations. In Multiple Time Scales (Brackbill, J.U., Cohen, B.I.,Hrsg.),*Academic Press Orlando*, p. 378.
- [3] Aarseth S. J., Lin D. N. C., Palmer P. L., 1993. Evolution of Planetesimals. II. Numerical Simulations. *Astrophysical Journal* **403**, 351
- [4] Aarseth, S. J., 1999. From NBODY1 to NBODY6: The Growth of an Industry. *PASP* **111**, 1333
- [5] Aarseth S., 2003. Gravitational N -Body Simulations. *Cambridge University Press*
- [6] Adachi I., Hayashi C., Nakazawa K., 1976. The Gas Drag Effect on the Elliptic Motion of a Solid Body in the Primordial Solar Nebula. *Progress of Theoretical Physics* **56**, 1756–1771
- [7] Ahmad A. and Cohen L., 1973. A Numerical Integration Scheme for the N -Body Gravitational Problem. *Journal of Computational Physics* **12**, 389–402
- [8] Artymowicz P., Lin D. N. C., Wampler E. J., 1993. Star trapping and metallicity enrichment in quasars and active galactic nuclei. *Astrophysical Journal* **409**, 592
- [9] Astakhov S. A., Lee E. A., Farrelly D., 2005. Formation of Kuiper-belt binaries through multiple chaotic scattering encounters with low-mass intruders *MNRAS* **360**, 401–415
- [10] Bagatin A. C., Cellino A., Davis D. R., Farinella P., Paolicchi P., 1994. Wavy size distribution for collisional systems with a small-size cutoff. *Planet. Space. Sci.* **42**, 1079–1092
- [11] Balbus S. A., Hawley J. F., 1998. Instability, turbulence, and enhanced transport in accretion disks. *Reviews of Modern Physics* **70**, 1–53
- [12] Balbus. S. A., 2003. Enhanced Angular Momentum Transport in Accretion Disks. *Ann. Rev. Astron. Astrophys.* **41**, 555–597
- [13] Bateman H., 1915. Some recent Researches on the Motion of Fluids. *Monthly Weather Review* **43**, 163
- [14] Beaulieu J.-P. et al., 2006. Discovery of a cool planet of 5.5 Earth masses through gravitational microlensing. *Nature* **439**, 437–440
- [15] Beckwith S. V. W. and Sargent A. I., 1996. Circumstellar disks and the search for neighbouring planetary systems. *Nature* **383**, 139–144
- [16] Benedict G. F., McArthur B. E., Forveille T., Delfosse X., Nelan, E., Butler R. P., Spiesman W., Marcy G., Goldman B., Perrier C., Jefferys W. H., Mayor M., 2002. A Mass for the Extrasolar Planet Gliese 876b Determined from Hubble Space Telescope Fine Guidance Sensor 3 Astrometry and High-Precision Radial Velocities. *Astrophysical Journal* **581**, L115–L11

- [17] Benz W. and Asphaug E., 1999. Catastrophic Disruptions Revisited. *Icarus* **142**, 5–20
- [18] Berczik P., Merritt D., Spurzem R., 2005. Long–Term Evolution of Massive Black Hole Binaries. II. Binary Evolution in Low-Density Galaxies. *Astrophysical Journal* **633**, 680–687
- [19] Binney J., 1977. Dynamical friction in aspherical clusters. *MNRAS* **181**, 735–746
- [20] Binney J. and Tremain S., 1994. Galactic Dynamics, Third printing. *Princeton University Press, Princeton, New Jersey*
- [21] Birn J., 1973. On the Stability of the Planetary System. *Astronomy and Astrophysics* **24**, 283–293
- [22] Blum J. and Wurm G., 2000. Experiments on Sticking, Restructuring, and Fragmentation of Preplanetary Dust Aggregates. *Icarus* **143**, 138
- [23] Bodenheimer P. and Pollack J. B., 1986. Calculations of the accretion and evolution of giant planets The effects of solid cores. *Icarus* **67**, 391–408
- [24] Bodenheimer P., Hubickyj O., Lissauer J. J., 2000. Models of the in Situ Formation of Detected Extrasolar Giant Planets. *Icarus* **143**, 2–14
- [25] Bottke W. F., Durda D. D., Nesvorný D., Jedicke R., Morbidelli A., Vokrouhlický D., Levison H., 2005. The fossilized size distribution of the main asteroid belt. *Icarus* **175**, 111–140
- [26] Bromley B. C. and Kenyon S. J., 2006. A Hybrid N–body–Coagulation Code for Planet Formation. *astro-ph* **0602327** (15/2/2006)
- [27] Burgers J. M., 1948. A mathematical model illustrating the theory of turbulence. *Adv. Appl. Mech.* **1**, 171
- [28] Burns J. A., Lamy P. L., Soter S., 1979. Radiation forces on small particles in the solar system. *Icarus* **40**, 1–48
- [29] Butler R. P., Vogt S. S., Marcy G. W., Fischer D. A., Wright J. T., Henry G. W., Laughlin G., Lissauer J., 2004. A Neptune–Mass Planet Orbiting the Nearby M Dwarf GJ 436. *Astrophysical Journal* **617**, 580–588
- [30] Cameron A. G. W., 1973. Abundances of the Elements in the Solar System. *Space Science Reviews* **15**, 121
- [31] Canup R. M. and Agnor C. B., 2001. Accretion of terrestrial planets and the Earth Moon system. In *Origin of the Earth and the Moon (Canup, R.M., Righter, K., Hrsg.)*, Univ. of Arizona Press, Tucson p. 113
- [32] Chandrasekhar S., 1942. Dynamical Friction. I. General Considerations: the Coefficient of Dynamical Friction. *Astrophysical Journal* **97**, 255
- [33] Charbonneau D., Brown T. M., Latham D. W., Mayor M., 2000. Detection of Planetary Transits Across a Sun–like Star. *Astrophysical Journal* **529**, L45–L48
- [34] Charnoz, S., Thébault P., Brahic A., 2001. Short–term collisional evolution of a disc perturbed by a giant-planet embryo. *Astronomy and Astrophysics* **373**, 683
- [35] Chauvin G., Lagrange A.–M., Dumas C., Zuckerman B., Mouillet D., Song I., Beuzit J.–L., Lowrance P., 2005. Giant planet companion to 2MASSW J1207334–393254 *Astronomy and Astrophysics* **438**, L25
- [36] Connaughton C., Rajesh R., Zaboronski O., 2004. Stationary Kolmogorov solutions of the Smoluchowski aggregation equation with a source term. *Physical Review E* **69**, 061114

- [37] Cox A. N., 2000. Allen's astrophysical quantities 4th ed. *Springer, AIP Press, New York 2000*
- [38] Del Popolo A., Gambera M., Ercan N., 2001. Migration of giant planets in planetesimal discs. *MNRAS* **325**, 1402
- [39] Dohnanyi J. W., 1969. Collisional models of asteroids and their debris. *Journal of Geophys. Research* **74**, 2531–2554
- [40] Duncan M. J., Levison H. F., Lee M. H., 1998. A Multiple Time Step Symplectic Algorithm for Integrating Close Encounters. *Astronomical Journal* **116**, 2067–2077
- [41] Estrada P. R., Mosqueira I., 2003. Gap–Opening, Disk Clearing, and the Survival of the Regular Satellites of Jupiter and Saturn. *34th Annual Lunar and Planetary Science Conference*
- [42] Fukushige T., Makino J., Kawai A., 2005. GRAPE-6A: A Single-Card GRAPE-6 for Parallel PC-GRAPE Cluster Systems. *PASJ* **57**, 1009–1021
- [43] Glaschke P., 2003. Fragmentation of Planetesimals – Modeling and Results. *ESA SP-539*, p425
- [44] Goldreich P. and Ward W. R., 1973. The formation of planetesimals. *Astrophysical Journal* **183**, 1051–1061
- [45] Goldreich P., Lithwick Y., Sari R., 2004. Final Stages of Planet Formation. *Astrophysical Journal* **614**, 497–507
- [46] Goldreich P., Lithwick Y., Sari R., 2004b. Planet Formation by Coagulation: A Focus on Uranus and Neptune. *Annu. Rev. Astron. Astrophys.* **42**, 549–601
- [47] Greenberg R., Hartmann W. K., Chapman C. R., Wacker J. F., 1978. Planetesimals to planets – Numerical simulation of collisional evolution. *Icarus* **35**, 1–26
- [48] Greenberg R. and Bottke W. F., 1991. Planetary Accretion Rates: Analytical Derivation. *Icarus* **94**, 98
- [49] Greenzweig Y. and Lissauer J., 1990. Accretion Rates of Protoplanets. *Icarus* **87**, 40
- [50] Greenzweig Y. and Lissauer J., 1992. Accretion Rates of Protoplanets II. *Icarus* **100**, 440
- [51] Hasegawa M. and Nakazawa K., 1990. Distant encounter between Keplerian particles. *Astronomy and Astrophysics* **227**, 619–627
- [52] Hayashi C., 1981. Structure of the Solar Nebula, Growth and Decay of Magnetic Fields and Effects of Magnetic and Turbulent Viscosities on the Nebula. *Progress of Theoretical Physics Supplement* **70**, 35–53
- [53] Hemsendorf M., Sigurdsson S., Spurzem R., 2002. Collisional Dynamics around Binary Black Holes in Galactic Centers. *Astrophysical Journal* **581**, 1256–1270
- [54] Hénon M. and Petit J.–M., 1986. Series Expansions for Encounter–Type Solutions of Hills Problem. *Celestial Mechanics* **38**, 67
- [55] Hernquist L., Hut P., Makino J., 1993. Discreteness Noise versus Force Errors in N –Body Simulations. *Astrophysical Journal* **402**, L85–L88
- [56] Hill G. W., 1878. Researches in the Lunar Theory. *American J. Math.* **1**, 5–26, 129–147, 245–260

- [57] Hornung P., Pellat R., Barge P., 1985. Thermal velocity equilibrium in the protoplanetary cloud. *Icarus* **64**, 295
- [58] Housen K. R. and Holsapple K. A., 1990. On the Fragmentation of Asteroids and Planetary Satellites. *Icarus* **84**, 226
- [59] Hughes D. W. and Cole G. H. A., 1995. The asteroidal sphericity limit. *MNRAS* **277**, 99–105
- [60] Ida S. and Nakazawa K. S., 1989. Collisional probability of planetesimals revolving in the solar gravitational field. III *Astronomy and Astrophysics* **224**, 303
- [61] Ida S., 1990. Stirring and Dynamical Friction Rates of Planetesimals in the Solar Gravitational Field. *Icarus* **88**, 129–145
- [62] Ida S. and Makino J., 1992. N-body simulation of gravitational interaction between planetesimals and a protoplanet. I – Velocity distribution of planetesimals. *Icarus* **96**, 107
- [63] Ida S., Kokubo E., Makino J., 1993. The Origin of Anisotropic Velocity Dispersion of Particles in a Disc Potential. *MNRAS* **263**, 875
- [64] Ida S. and Makino J., 1993b. Scattering of planetesimals by a protoplanet – Slowing down of runaway growth. *Icarus* **106**, 210
- [65] Ida S. and Lin D. N. C., 2004. Towards a Deterministic Model of Planetary Formation. I. A Desert in the Mass and Semimajor Axis Distributions of Extrasolar Planets. *Astrophysical Journal* **604**, 388
- [66] Ida S. and Lin D. N. C., 2004b. The formation and retention of gas giant planets around stars with a range of metallicities. *astro-ph 0408019*
- [67] Inaba S., Tanaka H., Nakazawa K., Wetherill G. W., Kokubo E., 2001. High-Accuracy Statistical Simulation of Planetary Accretion: II. Comparison with N-Body Simulation. *Icarus* **149**, 235
- [68] Inaba S., Wetherill G. W., Ikoma M., 2003. Formation of gas giant planets: core accretion models with fragmentation and planetary envelope. *Icarus* **166**, 46–62
- [69] Inaba S., Barge P., Daniel E., Guillard H., 2005. A two-phase code for protoplanetary disks. *Astronomy and Astrophysics* **431**, 365–379
- [70] Jewell G. M. and Alexander S. G., 1996. A Hybrid Statistical/N-Body Simulation for Mid-Stage Solar System Formation. *Bulletin of the American Astronomical Society* **28**, 1107
- [71] Johansen A., Klahr H., Henning T., 2006. Gravoturbulent Formation of Planetesimals. *Astrophysical Journal* **636**, 1121–1134
- [72] Kary D. M., Lissauer J., Greenzweig Y., 1993. Nebular gas drag and planetary accretion. *Icarus* **106**, 288
- [73] Kempf S., Pfalzner S., Henning T. K., 1999. N-particle-simulations of dust growth. *Icarus* **141**, 388–398
- [74] Kenyon S. J. and Luu J. X., 1998. Accretion in the Early Kuiper Belt. I. Coagulation and Velocity Evolution. *Astronomical Journal* **115**, 2136–2160
- [75] Kenyon S. J. and Luu J. X., 1999. Accretion in the Early Kuiper Belt. II. Fragmentation. *Astronomical Journal*, **118** 1101–1119
- [76] Kenyon S. J. and Bromley B. C., 2001. Gravitational Stirring in Planetary Debris Disks. *Astronomical Journal* **121**, 538

- [77] Kenyon S. J. and Bromley B. C., 2004. Collisional Cascades in Planetesimal Disks. II. Embedded Planets. *Astronomical Journal* **127**, 513–530
- [78] Kenyon S. J. and Bromley B. C., 2006. Terrestrial Planet Formation I. The Transition from Oligarchic Growth to Chaotic Growth. *Astronomical Journal* **131**, 1837–1850
- [79] Kokubo E. and Ida S., 1995. Orbital Evolution of Protoplanets Embedded in a Swarm of Planetesimals. *Icarus* **114**, 247
- [80] Kokubo E. and Ida S., 1996. On Runaway Growth of Planetesimals. *Icarus* **123**, 180–191
- [81] Kokubo E. and Ida S., 1997. Oligarchic Growth of Protoplanets. *Icarus* **131**, 171
- [82] Kokubo E., Yoshinaga K., Makino J., 1998. On a time-symmetric Hermite integrator for planetary N -body simulation. *MNRAS* **297**, 1067–1072
- [83] Kokubo E. and Ida S., 1998. Oligarchic Growth of Protoplanets. *Icarus* **131**, 171
- [84] Kokubo E., Ida S., 2000. Formation of Protoplanets from Planetesimals in the Solar Nebula. *Icarus* **143**, 15
- [85] Kokubo, E., Ida, S., 2002. Formation of Protoplanet Systems and Diversity of Planetary Systems. *Astrophysical Journal* **581**, 666
- [86] Kokubo E. and Makino J. 2004. A Modified Hermite Integrator for Planetary Dynamics. *PASJ* **56**, 861–868
- [87] Kominami J. and Ida S., 2004. Formation of terrestrial planets in a dissipating gas disk with Jupiter and Saturn. *Icarus* **167**, 231–243
- [88] Kornet K., Stepinski T. F., Różyczka M., 2001. Diversity of planetary systems from evolution of solids in protoplanetary disks. *Astronomy and Astrophysics* **378**, 180–191
- [89] Kortenkamp S. J., Kokubo E., Weidenschilling S. J., 2001. Formation of planetary embryos. In *Origin of the Earth and the Moon (Canup, R.M., Righter, K., Hrsg.)*, Univ. of Arizona Press, Tucson, p. 85.
- [90] Krivov A. V., Sremčević M., Spahn F., 2005. Evolution of a Keplerian disk of colliding and fragmenting particles: a kinetic model with application to the Edgeworth–Kuiper belt. *Icarus* **174**, 105–134
- [91] Kustaanheimo P. and Stiefel E. L., 1965. Perturbation theory of Kepler motion based on spinor regularization. *J. Reine angew. Math.* **218**, 204–219
- [92] Larson R. B., 1970. A method for computing the evolution of star clusters. *MNRAS* **147**, 323
- [93] Leinhardt Z. M. and Richardson D. C., 2005. Planetesimals to Protoplanets. I. Effect of Fragmentation on Terrestrial Planet Formation. *Astrophysical Journal* **625**, 427–440
- [94] Levison H., Nesvorny D., Agnor C., Morbidelli A., 2005. The Role of Dynamical Friction in Terrestrial Planet Formation. *American Astronomical Society, DPS meeting* **37**, 2501
- [95] Lin D. N. C., Papaloizou J., 1979. On the structure of circumbinary accretion disks and the tidal evolution of commensurable satellites. *MNRAS* **188**, 191–201
- [96] Lissauer J., 1993. Planet Formation. *Annu. Rev. Astron. Astrophys.* **31**, 129–174
- [97] Makino J. and Hut P., 1988. Performance Analysis of Direct N -Body Calculations. *Astrophysical Journal Supplement* **68**, 833–856

- [98] Makino J., 1991. Optimal order and time-step criterion for Aarseth-type N-body integrators. *Astrophysical Journal* **369**, 200–212
- [99] Makino J. and Aarseth S. J., 1992. On a Hermite integrator with Ahmad-Cohen scheme for gravitational many-body problems. *PASJ* **44**, 141–151
- [100] Makino, J., Fukushige, T., Funato, Y., Kokubo, E., 1998. On the Mass Distribution of Planetesimals in the Early Runaway Stage. *New Astronomy* **3**, 441
- [101] Makino J. and Funato Y., 2004. Evolution of Massive Black Hole Binaries. *Astrophysical Journal* **602**, 93–102
- [102] Masset F. S. and Papaloizou J. C. B., 2003. Runaway Migration and the Formation of Hot Jupiters. *Astrophysical Journal* **588**, 494–508
- [103] Mayor M. and Queloz D., 1995. A Jupiter-Mass Companion to a Solar-Type Star. *Nature* **378**, 355
- [104] McNeil, D. S., Duncan, M. J., Levison, H. F., 2004. Effects of Type I Migration on Terrestrial Planet Formation. *American Astronomical Society DPS meeting* **36**, 4407
- [105] Merrit D., 2001. Brownian Motion of a Massive Binary. *Astrophysical Journal* **556**, 245
- [106] Michel P., Tanga P., Benz W., Richardson D. C., 2002. Formation of Asteroid Families by Catastrophic Disruption: Simulations with Fragmentation and Gravitational Reaccumulation. *Icarus* **160**, 10–23
- [107] Mikkola S., 1997. Practical Symplectic Methods with Time Transformation for the Few-Body Problem. *Celestial Mechanics and Dynamical Astronomy* **67**, 145–165
- [108] Mikkola S. and Aarseth S. J., 1998. An efficient integration method for binaries in N-body simulations. *New Astronomy* **3**, 309–320.
- [109] Nakagawa Y., Hayashi C., Nakazawa Y., 1983. Accumulation of planetesimals in the solar nebula. *Icarus* **54**, 361–376
- [110] O’Brien D. P. and Greenberg R., 2003. Steady-state size distributions for collisional populations: analytic solution with size-dependent strength. *Icarus* **164**, 334
- [111] O’dell C. R., Wen Z., Hu X., 1993. Discovery of new objects in the Orion nebula on HST images – Shocks, compact sources, and protoplanetary disks. *Astrophysical Journal* **410**, 696–700
- [112] O’dell C. R. and Wen, Z. 1994. Postrefurbishment mission Hubble Space Telescope images of the core of the Orion Nebula: Proplyds, Herbig-Haro objects, and measurements of a circumstellar disk. *Astrophysical Journal* **436**, 194–202
- [113] Ohtsuki K., Nakagawa Y., Nakazawa K., 1990. Artificial Acceleration in Accumulation Due to Coarse Mass-Coordinates Divisions in Numerical Simulations. *Icarus* **83**, 205
- [114] Ohtsuki K., 1993. Capture probability of colliding planetesimals - Dynamical constraints on accretion of planets, satellites, and ring particles. *Icarus* **106**, 228
- [115] Ohtsuki K., 1999. Evolution of Particle Velocity Dispersion in a Circumplanetary Disk Due to Inelastic Collisions and Gravitational Interactions. *Icarus* **137**, 152
- [116] Ohtsuki K., Stewart G. R., Ida S. 2002. Evolution of Planetesimal Velocities Based on Three-Body Orbital Integrations and Growth of Protoplanets. *Icarus* **155**, 436
- [117] Paczynski B., 1996. Gravitational Microlensing in the Local Group. *Ann. Rev. Astron. Astrophys.* **34**, 419–460

- [118] Palmer P. L., Lin D. N. C., Aarseth S. J., 1993. Evolution of Planetesimals. I. Dynamics: Relaxation in a thin disk. *Astrophysical Journal* **403**, 336–350
- [119] Papaloizou J. C. B. and Larwood J. D., 2000. On the orbital evolution and growth of protoplanets embedded in a gaseous disc. *MNRAS* **315**, 823–833
- [120] Papaloizou J. C. B. and Terquem C., 2006. Planet formation and migration. *Rep. Prog. Phys.* **69**, 119–180
- [121] Petit J.-M. and Hénon M., 1986. Satellite Encounters. *Icarus* **66**, 536
- [122] Petit J.-M. and Hénon M., 1987. A numerical simulation of planetary rings. II – Monte Carlo model. *Astronomy and Astrophysics* **188**, 198
- [123] Plummer H. C., 1911. On the problem of distribution in globular star clusters. *MNRAS* **71**, 460–470
- [124] Preto M. and Tremaine S., 1999. A Class of symplectic Integrators with adaptive Time Step for separable Hamiltonian Systems. *Astronomical Journal* **118**, 2532–2541
- [125] Rafikov R. R., 2001. Termination of Planetary Accretion due to Gap Formation. *Astronomical Journal* **122**, 2713–2722
- [126] Rafikov R. R., 2003. Planetesimal Disk Evolution Driven by Planetesimal-Planetesimal Gravitational Scattering. *Astronomical Journal* **125**, 906
- [127] Rafikov R. R., 2003b. Planetesimal Disk Evolution Driven by Embryo-Planetesimal Gravitational Scattering. *Astronomical Journal* **125**, 922
- [128] Rafikov R. R., 2003c. The Growth of Planetary Embryos: Orderly, Runaway, or Oligarchic? *Astronomical Journal* **125**, 942
- [129] Rafikov R. R., 2003d. Dynamical Evolution of Planetesimals in Protoplanetary Disks. *Astronomical Journal* **126**, 2529
- [130] Safronov V. S., 1969. Evolution of the protoplanetary cloud and formation of the Earth and the planets. *NASA-TTF* 677
- [131] Shiidsuka, K., Ida, S., 1999. Evolution of the velocity dispersion of self-gravitating particles in disc potentials. *MNRAS* **307**, 737
- [132] Skeel R. D., 1999. Symplectic integration with floating-point arithmetic and other approximations. *Applied Numerical Mathematics* **29**, 3–18
- [133] Spaute, D., Weidenschilling, S. J., Davis, D. R., Marzani, F., 1991. Accretional Evolution of a Planetesimal Swarm: 1. A New Simulation. *Icarus* **92**, 147
- [134] Spurzem R. and Aarseth S. J., 1996. Direct collisional simulation of 100000 particles past core collapse. *MNRAS* **282**, 19
- [135] Spurzem, R., 1999. Direct N-body Simulations. *The Journal of Computational and Applied Mathematics, Special Volume Computational Astrophysics* **109**, 407–432
- [136] Stewart G. R. and Wetherill G. W., 1988. Evolution of planetesimal velocities. *Icarus* **74**, 542
- [137] Stewart G. R. and Ida S., 2000. Velocity Evolution of Planetesimals: Unified Analytical Formulas and Comparisons with N-Body Simulations. *Icarus* **143**, 28
- [138] Takeuchi T., Miyama S. M., Lin D. N. C., 1996. Gap Formation in Protoplanetary Disks. *Astrophysical Journal* **460**, 832

- [139] Tanaka, H. and Nakazawa K., 1994. Validity of the Statistical Coagulation Equation and Runaway Growth of Protoplanets. *Icarus* **107**, 404
- [140] Tanaka, H. and Ida S., 1996. Distribution of Planetesimals around a Protoplanet in the Nebula Gas. *Icarus* **120**, 371
- [141] Tanaka, H., Inaba, S., Nakazawa, K., 1996b. Steady-State Size Distribution for the Self-Similar Collision Cascade. *Icarus* **123**, 450
- [142] Thébault P. and Brahic A., 1998. Dynamical influence of a proto-Jupiter on a disc of colliding planetesimals. *Planetary and Space Sciences* **47**, 233
- [143] Thommes E. W., Duncan M. J., Levison H. F., 2003. Oligarchic growth of giant planets. *Icarus* **162**, 431–455
- [144] Press W. and Spergel D.N., 1988. Choice of order and extrapolation method in Aarseth-type N-body algorithms. *Astrophysical Journal* **325**, 715–721
- [145] Ward W. R., 1986. Density waves in the solar nebula – Differential Lindblad torque. *Icarus* **67**, 164–180
- [146] Weidenschilling S. J., 1977. Aerodynamics of solid bodies in the solar nebula. *MNRAS* **180**, 57
- [147] Weidenschilling S. J., 1980. Dust to planetesimals – Settling and coagulation in the solar nebula. *Icarus* **44**, 172
- [148] Weidenschilling S. J., 1984. Evolution of grains in a turbulent solar nebula. *Icarus* **60**, 553
- [149] Weidenschilling S. J., Spaute D., Davis D. R., Marzari F., Ohtsuki K., 1997. Accretional Evolution of a Planetesimal Swarm. *Icarus* **128**, 429
- [150] Wetherill G. W. and Stewart G. R., 1989. Accumulation of a Swarm of Small Planetesimals. *Icarus* **77**, 330
- [151] Wetherill G. W. and Stewart G. R., 1993. Formation of Planetary Embryos: Effects of Fragmentation, Low Relative Velocity, and Independent Variation of Eccentricity and Inclination. *Icarus* **106**, 190
- [152] Wisdom J. and Holman M., 1991. Symplectic maps for the n-body problem. *Astronomical Journal* **102**, 1528–1538
- [153] Wuchterl G., 1999. Giant planet formation – a theoretical timeline. In: *Planetary systems in the universe: Observation, formation, and evolution* (Penny, A.J., Artymowicz, P., Lagrange, A.-M., Hrsg.), Proc. IAU Symp. No. 202, ASP IAU Symp. Series, im Druck.
- [154] Wuchterl G., Guillot T., Lissauer J.J., 2000. Giant planet formation. In *Protostars and Planets IV* (Mannings, V., Boss, A. P., Russell, S. S., Hrsg.), Univ. of Arizona Press, Tucson. p. 1081.

Acknowledgments / Danksagung

Eigentlich bevorzuge ich es, mich eher kurz zu fassen – sicher lächelt jetzt der eine oder andere, aber zumindest schriftlich ziehe ich eine knappe Formulierung blumigen Metaphern vor. Nach mehr als 130 Seiten befängt mich aber trotzdem noch das Gefühl, daß nicht alles gesagt wurde. Fertig ist eine Arbeit nie – es gibt immer die Möglichkeit, weitere Details zu erforschen, neue Themen einzuschließen oder Altes präziser zu fassen.

Vielleicht ist es mir gelungen, dieser “ewigen” Unvollständigkeit ein Stück zu entrinnen. Sicher ist nur, daß diese Arbeit ohne einen Dank für die Begleitung und Unterstützung während der letzten drei Jahre aufs gröbste unvollständig wäre. Zu meiner Freude haben unwahrscheinlich viele Menschen dazu beigetragen, daß ich nun diese abschließenden Zeilen schreiben kann. Ich fürchte so viele, daß es fast unmöglich ist, alle zu nennen.

Mein Betreuer Rainer Spurzem hat mir ermöglicht, dieses Thema in aller Freiheit zu bearbeiten und mich bei all den kleinen und großen Problemen engagiert unterstützt. Besonders möchte ich mich für die hervorragende Arbeitsatmosphäre bedanken, mit der er erst ein konzentriertes Arbeiten, spannende Diskussionen mit Kollegen und kreative Ideen ermöglicht hat.

Meinem zweiten Gutachter Herrn Prof. Tscharnuter möchte ich nicht nur für die Unterstützung bei der Beurteilung dieser Arbeit danken, sondern auch für die “Initialzündung” vor einigen Jahren im Seminar im ITA. Ich erinnere mich noch gut an die Fragen und Anregungen zur Entstehung von Planeten, die der wesentliche Impuls zur Behandlung dieses Themas waren.

Douglas Lin overwhelmed me with his hospitality during my stay in Santa Cruz during last November. I enjoyed the discussions on my work that helped me very much to understand the big picture. A special thank goes to Eric ‘the collaborator’ Asphaug for our productive discussion on the various aspects of fragmentation.

Während der letzten Wochen wurde ich tatkräftig bei der Durchsicht, Korrektur und Überarbeitung meiner Arbeit unterstützt (verbliebene Fehler liegen natürlich in meiner Verantwortung, und dienen ausschließlich als Übung für den Leser).

Vor mehr als einem Jahr tauchte ich mit Jens Rodmann zusammen in die Unwägbarkeiten der N -body Programmierung ab. In den letzten Wochen teilte er mit mir ein Büro und erfüllte dabei den Raum alleine durch seine Anwesenheit mit einer unglaublichen Ruhe, die mir auf den letzten Metern sehr geholfen hat. Darüber hinaus hat er mir mehr als einmal in mancher sprachlicher Notlage geholfen: Dem(!) war echt hilfreich!

Alexey Minz is one of the few people who master the art of keeping innocent colleagues whole nights busy with seemingly simple questions. I enjoyed every minute of our discussions, and I think the proofreading of my thesis was a fair revenge ☺. Do not stop asking these question – more sleepless nights are waiting!

Der Dritte im Bunde der Korrekturleser war Andreas Ernst. Eigentlich wäre an dieser Stelle ein Verweis angebracht, da seine Fragen meist wenig mit der Arbeit, dafür aber um so mehr mit allen anderen physikalischen Themen zu tun hatten. Wie gesagt, eigentlich . . . aber ich habe soviel dabei gelernt, das ich jegliche Beschwerden einfach mit einem “Danke” ersetze.

A special thank goes to the creator of the NBODY-codes Sverre Aarseth. Once I thought it would be good to meet him to get first-hand information on the N -body codes. But when I actually got to know Sverre, I enjoyed his kindness and enthusiasm so much, that I abandoned all the technical questions. Inspiration is more important than subroutines! However, I received precious support from the N -body fellows Chingis Omarov, Pau Amaro-Seoane and Gábor Kúpi. There is no stronger uniting agent than a misbehaving code!

I also thank the ‘legendary’ Peter Berczik, father of the practical Berczik-benchmark-unit, for all his suggestions. He has the rare talent to make you feel home virtually wherever you are, even during the most intense Teeminar discussions.

Andrea Borch hat uns alle immer wieder mit ihren interessanten Diskussionsthemen überrascht. Auch wenn ich nach drei Jahren Forschung immer noch nicht verstanden habe, was ‘gender mainstreaming’ eigentlich ist.

I specially thank José Fiestas, our Teexperte at Weberstrasse, and his wife Wendy. Together with Miguel Preto they are the lively heart of Weberstrasse. Ovidiu Furdui taught me a fascinating Zen (?) wisdom that is still on my mind: ‘Silence is the perfect sound.’

Marc Freitag gave me not only an exciting introduction to the world of Monte-Carlo codes, but also enriched my understanding of astronomy with many interesting discussions.

Christoph Eichhorn, Emil Khalisi, Andreas Just, Kristin Warnick und Kristina Wäcken haben mir mit ihren Arbeitsgebieten Einblick in Sternhaufen und Galaxien gegeben. Ich habe dabei nicht nur neue Methoden kennengelernt, sondern wurde auch stetig an den großen Zusammenhang von Planetensystemen mit ihrer Umgebung erinnert. Hoffentlich ist es mir gelungen, mit dieser gediegenen ☺Arbeit auch einen Einblick in mein Fachgebiet zu geben.

A special thank and a ‘merci beaucoup’ goes to the ‘lens guys’ Robert Schmidt and Arnaud Cassan. They fought hard to keep up with all that star cluster stuff, so I fear that they finally gave up. However, they never abandoned their kind support and patience.

Ich möchte auch meinen Kommilitonen Alexander Westphal, Daniel Buchholz, Jens Bossmeyer, Jörg Lange, Kerstin Schindler, Michaela Tscherneck sowie Judith Abbé danken. Leider zählten auch die grauen Männer zu meinen (ausnahmsweise unerwünschten) Unterstützern, aber hoffentlich ist es mir zumindest zeitweise gelungen, den Stress abzuschütteln und an euch zu denken. Ich wünsche euch viel Erfolg für eure Zukunft!

Mathias Schott hat mir nicht nur mit vielen Kommentaren geholfen, sondern auch meine Aufmerksamkeit immer wieder auf all die Dinge jenseits der Astronomie gelenkt. Tja, sieht wohl doch so aus als ob Du recht behalten würdest ☺.

Meine Familie hat mich bei meinem Vorhaben immer unterstützt und mir bei viele Dingen des Alltags den Rücken frei gehalten. Ohne diese Hilfe gerade während der letzten Monate hätte ich mich nicht in diesem Maße auf die Arbeit konzentrieren können.

Ganz besonders möchte ich Sabine danken. Es ist klar, wie sehr Du mir bei der Fertigstellung dieser Arbeit geholfen hast. Du bereicherst mein Leben, und ich freue mich immer wieder aufs neue auf jeden gemeinsamen Tag.

Since I am not rewarded with an Oscar, I omit special thanks to my gardener (who I never had) and to the director of ‘Nightmare on Weberstreet’ (since this movie does not exist either). I leave you all with a quote from one of the ancestors of modern physics. Believe me, he is right.

An expert is a person who has made all the mistakes that can be made in a very narrow field.

Niels Bohr (1885 – 1962)